Doctoral Dissertation

Application of Remote Sensing Technique for Assessment of Natural Disasters in Afghanistan

（アフガニスタンにおける自然災害把握のための
リモートセンシング技術の応用に関する研究）

Department of Architecture
Graduate School of Engineering
Hiroshima University

Mujeeb Rahman Atefi

Sep 2022

Dedication

“To my family”

Declaration

I hereby declare that I have completed the present work, entitled " Application of Remote Sensing Technique for Assessment of Natural Disasters in Afghanistan" solely and without illegal aid from outside sources. There are no further sources and aids besides those listed, which have indicated sections borrowed verbatim or thematically from the utilized references.

Hiroshima, August 10, 2022

Mujeeb Rahman Atefi

Acknowledgments

First and foremost, I would like to express my sincere gratitude to my advisor assoc. Prof. Hiroyuki Miura for the continuous support of my Ph.D. studies and research, as well as for his patience, motivation, enthusiasm, and immense knowledge. His office door was always open whenever I ran into a trouble spot or had a query regarding my study or writing. Moreover, he consistently steered me in the right direction whenever he believed it was necessary, and his dynamism, vision, sincerity, and motivation have deeply inspired me. He has instructed me on the process for conducting research and presenting it as plainly as feasible. In a word, I can say that he is more than a supervisor, and thankfully, it was a wonderful privilege and honor to work and study under his supervision, and I hope that our professional relationship may continue.

Second, my most profound appreciation goes to Prof. N. Nakamura and Assoc. Prof. T. Mori for being my sub-supervision and taking their valuable time for reading this dissertation. I would also like to thank Prof. Hiroshi Tagawa, for serving as my committee member despite his busy schedules and provide me his insightful feedback during the preliminary exam.

During my studies, I was grateful for the MEXT (Ministry of Education, Culture, Sports, Science, and Technology) scholarship. I am extremely grateful to everyone who has been supportive of my professional objectives and who has worked hard to give me with the protected academic time to achieve those ambitions, including the Engineering support office and other Hiroshima University employees for their kind demeanor and unending support.

Nobody has been more important to me in the pursuit of this project than the members of my family, so this is the opportunity to express my profound and sincere gratitude to my parents, sister, and brothers, whose love, guidance, and unending inspiration words are with me in whatever I pursue.

Mujeeb Rahman Atefi
Hiroshima University, Higashihiroshima City, Japan
Sept 2022

Acknowledgments

The dissertation may share some identical sentence or similar formulations from my publications:

” Volumetric Analysis of the Landslide in Abe Barek, Afghanistan Based on Nonlinear Mapping of Stereo Satellite Imagery-Derived DEMs”,
” Detection and Volume Estimation of Large-scale Landslide in Abe Barek, Afghanistan Using Nonlinear Mapping of DEMs” and
” Detection of Flash Flood Inundated Areas Using Relative Difference in NDVI from Sentinel-2 Images: A Case Study of the August 2020 Event in Charikar, Afghanistan”.

For the purpose of improving readability, I remove a clear identification and utilize the paragraphs of the current dissertation from the articles with the publisher's courteous permission. The readers are referred to the journals through the DOI URLs that are provided in the metadata tables in order to access the final versions of the articles.

Abstract

Afghanistan is a country that is exposed to numerous geomorphological hazards such as earthquakes, landslides, floods, droughts, avalanches, and man-made disasters. Natural disasters such as landslides and floods are among the most common hazards in various parts of the country, causing extensive damage to buildings and killing hundreds of people each year. Safety and economic problems, instability, ongoing war, and poverty have put Afghanistan among the countries that have paid less attention to research. Therefore, it is challenging to find a published map or find reports after a disaster to show you the details of a natural disaster along with its exact geographical location. Assessing the degree of catastrophes is vital for post-disaster efforts and for structural engineers planning and constructing appropriate structures to prevent future disasters. Based on this, people would choose to reside in secure places instead of vulnerable ones. Because most structures in Afghanistan are created by people without any engineering, designs, assessments, or ideas owing to a lack of total government oversight and regular urban planning. Considering the concerns described, the relevance of the issue, and the scarcity of research in the specified areas in Afghanistan, an attempt was made in this study to perform a study on floods and landslides. It was planned to conduct current study to investigate without traveling to the impacted region for on-site data collection due to acute security issues. As a result, this research focuses on assessing two natural disasters (the Abe-Barek landslide and the Charikar flood) utilizing remote sensing analyses.

Chapter 1 discussed how natural catastrophes, notably floods and landslides, are common in many places of Afghanistan. In the background and literature review part, it has been demonstrated that, despite being classified as a natural disaster-prone country, Afghanistan has less research and knowledge on natural disasters. It has also been discussed that how catastrophe assessments are crucial for post-disaster operations and for policymakers seeking to prevent future disasters. This chapter also discussed the purpose and research problem.

Chapter 2 discussed the specifics of natural disaster risk in Afghanistan, such as earthquakes, floods, landslides, avalanches, and droughts. The availability of risk information is critical for effective catastrophe and climate risk management. The risk profile summarizes and visualizes the national multi-hazard evaluations. Such data and information will be critical for politicians, decision-makers, development planners, and infrastructure investors to create a

more resilient future for Afghans. As a result, this chapter addressed the susceptibility map, lack of coping skills, lack of adaptive capacities, vulnerability map, population exposure to natural disasters, and world risk index as a result of exposure and vulnerability. Furthermore, it was also presented that which natural disasters have the greatest impact in terms of agricultural losses, property losses, and human losses.

Chapter 3 presented on the assessment of the Abe-Barek landslide using remote sensing analysis. The Abe-Barek landslide occurred on May 2, 2014 in northern parts of Afghanistan. Pre-and post-event Digital Elevation Models (DEMs) created from stereo pairs of high-resolution satellite images was used to evaluate the extent and the volume of displaced material. For obtaining such objectives a nonlinear technique was proposed to accurately align the multi-temporal DEMs to decrease the undesired artifacts from identified landslide affected areas and finally increase the accuracy of the estimation. The landslide volume was estimated as 1.05×10^6 m^3 from the corrected DEM of difference (DoD) by the nonlinear method and the relationship between the area and volume compared to those of the previous studies were discussed. Furthermore, in order to map the damaged region and determine the number of impacted people, the remote sensing-based damage assessment was also conducted.

Chapter 4 proposed a method for identifying and assessment of the Charikar flood. Since the Charikar flash flood occurred on August 26, 2020, there have been no high-resolution stereo pair satellite data available to use the same approach utilized for the landslide identification. A pixel-based spectral index approach which is suitable for assessing flash floods using lower resolution data were utilized. Relative Difference Normalized Difference Vegetation Index (NDVI) was used in Google Earth Engine with freely accessible medium resolution images (Sentinel-2). Also, pre- and post-event NDVIs and NDVI-time series were applied to track changes in the study region, and it is found that the NDVI dropped considerably after the incident and remained low for two years. The fact that the NDVI levels have not changed after two years is clear indication that there is no recovery process, neither given by the government nor by the people themselves. A DEM-based flow simulation was also conducted to examine the simulation's usefulness in detecting unsafe locations for future flood disasters The accuracy was also assessed using the official survey reports and other on-site data, such as satellite images. Based on the available data, it is concluded that both methodologies were suitable for monitoring, analyzing, and mapping almost all types of disasters in the future.

Chapter 5 concluded the overall result of this study as well as the study's strengths, shortcomings, recommendations and future directions.

TABLE OF CONTENTS

Pages

Dedication i
Declaration ii
Acknowledgments iii
Abstract vi
Table of Contents viii
List of Acronyms xi
List of Notations xii
List of Equations xiii
List of Tables xiv
List of Figures xv

CHAPTER I 1
Introduction 1
1.1 Background 1
1.2 Literature Review 5
1.2.1 Landslide Studies in Remote Sensing 5
1.2.2 Flood Studies in Remote Sensing 11
1.3 Problem Statement 15
1.4 Research Objectives 17
1.5 Organization of the Dissertation 18

CHAPTER II 20
Natural Disaster in Afghanistan 20
2.1 Introduction 20
2.2. Floods 24
2.2.1 Flood Risk and its impact on assets in Afghanistan 26
2.2.2. Recommendations 28
2.3. Earthquake 29
2.3.1 Earthquake Risk and its impact on assets in Afghanistan 33

2.3.2. Recommendations 36
2.4. Landslide 37
2.4.1 Landslide Risk and its impact on assets in Afghanistan 38
2.4.2. Recommendations 39
2.5. Snow Avalanches 40
2.5.1 Snow avalanches' risk and its impact on assets in Afghanistan 42
2.5.2. Recommendations 43
2.6. Droughts 44
2.6.1 Drought risk and its impact on assets in Afghanistan 47
2.6.2. Recommendations 49

CHAPTER III 50
Assessment of the Abe-Barek Landslide using Remote Sensing Analysis 50
3.1. Introduction 50
3.2. Satellite imagery used in landslide analysis 55
3.3. Nonlinear Mapping Method 60
3.4. Evaluation and Applicability of the Method 65
3.4.1. Statistical Assessment 66
3.4.2. Shifting Vectors Assessment 68
3.5. Quality Assessment 70
3.6. Landslide based nonlinear method's results 72
3.6.1. Corrected and uncorrected DEMs profile cross-sections 72
3.7. Volume Estimation 75
3.7.1 Previous landslide's volume versus current estimated one 79
3.8. Advantages and Shortcoming of the Method 82
3.9. Future Studies 83
3.10. Summary of this chapter 84

CHAPTER VI 86
Assessment of the Charikar Flood Using Remote Sensing Analysis 86
4.1 Introduction 86
4.2 Study Area and the Flash Flood in Charikar 87
4.3. The flash flood in Charikar 89

4.4. Materials 93
4.4.1. Sentinel-2 imagery 93
4.5. Methodology 95
4.5.1. NDVI and Spectral water indices 96
4.5.2. Normalized Difference vegetation Index (NDVI) 99
4.5.3. Normalized Difference Water Index (NDWI) 100
4.5.4. Normalized Difference Moisture Index (NDMI) 101
4.5.5. Relative Difference NDVI (rdNDVI) 104
4.5.6. Histogram-based segmentation 106
4.5.7. Accuracy assessment procedures using confusion matrix 107
4.5.8. Flood susceptibility mapping model based on Flow-R 108
4.6. Extraction of flood inundated areas 109
4.7. Inundation map by visual interpretation 114
4.8. Accuracy assessment 116
4.9. Monitoring the changes in the affected area in two years 118
4.10. Flow propagation analysis by Flow-R 120
4.11. Significance of the method 122
4.12. Urban planners and flood managers' expectations from current study 123
4.13. Applications and future aspects 125
4.14. Summary of this chapter 127

CHAPTER V 129
CONCLUSIONS 129
References 134
List of Publications 155

LIST OF ACRONYMS

ABBREVIATIONS	DESCRIPTIONS
DEM	Digital Elevation Model
GCP	Ground Control Point
DoD	Difference of Difference
LiDAR	Light Detection and Ranging
St. deviation	Standard deviation
RPC	Rational Polynomial Equation
NDVI	Normalized Difference Vegetation Index
rdNDVI	relative difference in Normalized Difference Vegetation Index
NDWI	Normalized Difference Water Index
MNDWI	Modified Normalized Difference Water Index
NDMI	Normalized Difference Moisture Index
AWEI	Automated Water Extraction Index
EWI	Enhanced Water Index
GEE	Google Earth Engine
ESA	European Space Agency
MSI	Multispectral Instrument
SAR	Synthetic Aperture Radar
ASTER-GDEM	ASTER Global Digital Elevation Model
ROI	Regions of Interest
NSIA	National Statistic, and Information Authority
NIR	The near infrared
ASTER	Advanced Spaceborne Thermal Emission and Reflection Radiometer

LIST OF UNIT NOTATIONS

NOTATIONS	DESCRIPTIONS
m	meter
%	Percentage
m^3	Cubic meter
A_L	Landslide Area
V_L	Landslide Volume
Z	Elevation
N_w	Window size
N_s	Search area
N_c	Consensus area

LIST OF EQUATIONS

Equation 3-1 Elevations' difference (*S*-Value). 60

Equation 3-2 The first scalars of the shifting vector 61

Equation 3-3 The threshold value of the vectors(d_{th}) 61

Equation 3-3 The ratio of inter-class variance 61

Equation 3-4 The total variance(σ_τ) 61

Equation 4-1 Normalized Difference vegetation Index (NDVI) formula 99

Equation 4-2 Normalized Difference Water Index (NDWI) formula 100

Equation 4-3 Modified Normalized Difference Water Index (MNDWI) 101

Equation 4-4 Normalized Difference Moisture Index (NDMI) 102

Equation 4-5 Relative Difference NDVI (rdNDVI) 105

Equation 4-6 Binarization method 106

LIST OF TABLES

Table 2-1 recorded number of earthquakes, magnitude from 1971 to 2017.....31

Table 3-1 Distinguished features of the satellite imagery used in this study.....55

Table 3-2 Statistical parameters of the DoDs 67

Table 3-3 Summarized erosion and deposition volumes for the corrected and uncorrected DoD.....79

Table 3-4 Empirical relationships linking the landslide area (AL) to the landslide volume (VL) obtained by various researchers.....81

Table 4-1 Distinguished features of the satellite imagery used in this study.....95

Table 4-2 Accuracy assessment result using the confusion matrix. 117

Table 4-3 Debris-flood parameters used in Flow-R. 120

LIST OF FIGURES

Figure 1-1 location of Afghanistan and neighboring countries. 02

Figure 1-2 Outline of the dissertation. 19

Figure 2-1 World disaster-related maps 22

Figure 2-2 number of affected people from different types of natural disaster from 2012 to 2022 23

Figure 2-3 Flood prone areas across all Afghanistan 24

Figure 2-4 GDP and Population exposure to floods 25

Figure 2-5 distribution of assets and its exposure to the flood 26

Figure 2-6 geotectonic plates inside and beyond Afghanistan's border 29

Figure 2-7 active faults inside Afghanistan 30

Figure 2-8 Historical earthquake between 11971-2017 in Afghanistan 31

Figure 2-9 recorded earthquake's magnitudes and depths from 2015 – 2022 32

Figure 2-10 Population and GDP exposure to earthquake 33

Figure 2-11 distribution of assets and its exposure to the flood 35

Figure 2-12 Population and GDP exposure to landslide 37

Figure 2-13 distribution of assets and its exposure to the landslides 38

Figure 2-14 Population and GDP exposure to snow avalanches 40

Figure 2-15 long line of vehicles half-buried in snow avalanches 41

Figure 2-16 distribution of assets and its exposure to the avalanches 42

Figure 2-17 Time series of mean temperature anomalies from 1981-2020 44

Figure 2-18 Population and GDP exposure to Droughts 46

Figure 2-19 Current and future impact of avalanche on assets 47

Figure 3-1 Location of the Abe-barek 51
Figure 3-2 front and top view of landslide affected area 52
Figure 3-3 Flow chart of the data acquisition 56
Figure 3-4 DEM, Hillshades, true image, and point cloud images 58
Figure 3-5 Uncorrected DEMs of difference 59
Figure 3-6 Flowchart of the nonlinear mapping method 63
Figure 3-7 Segmentation of DEMs, matching segments, shifting vector generation 63
Figure 3-8 histogram of shifting vectors thresholding, and consensus operation 64
Figure 3-9 Schematic plan and profile before and after nonlinear mapping 64
Figure 3-10 DEM presents the selected test area 66
Figure 3-11 Generated shifting vector for nine scenarios. 69
Figure 3-12 Comparison of histograms of the corrected and uncorrected DoD 71
Figure 3-13 Profile cross-section of uncorrected DOD 74
Figure 3-14 Profile cross-section of corrected DOD 74
Figure 3-15 Cross-section profile presents the pre-and post-event surface difference 77
Figure 3-16 Elevation difference along the cross-section line A-A' obtained from (pre-post) DEMs 78
Figure 3-17 Comparison of the estimated landslide volume from current study and previous studies 81
Figure 4-1 Topographical map Charikar study area 87
Figure 4-2 Photographs of the flashflood affected area. 90
Figure 4-3 Compounds in Charikar city are at risk of flood due to a lack of regular urban planning 91
Figure 4-4 Flowchart of the methodology used in this study. 96

Figure 4-5 Observation of changes in the study area using pre- and post-event Sentinel-2 satellite images....98
Figure 4-6 Observation of changes in the study area using....100
Figure 4-7 Observation of changes in the study area using pre- and post-event MNDWIs. 101
Figure 4-8 Observation of changes in the study area using NDMIs. 102
Figure 4-9 Observation of changes using NDVI, MNDWI, and NDMI time series ..103
Figure 4-10 Correlation graphs between NDVI and NDMI and MNDWI. 104
Figure 4-11 Result of rdNDVI map for five scenarios.....110
Figure 4-12 rdNDVI-based change detection image and greenest pixel composites....111
Figure 4-13 Histogram of the rdNDVI image with the chosen thresholds.....112
Figure 4-14 Extraction of inundated and non-inundated areas from the rdNDVI result based on binarization 113
Figure 4-15 Visual interpretation of the flood inundated area 114
Figure 4-16 NDVI time series over the study area; the blue line indicates the raw NDVI from Feb. 2019 to Apr. 2022. 119
Figure 4-17 rdNDVI changes in Charikar after one year period.....119
Figure 4-18 Flow-R flood -debris susceptibility map using different travel angles.....121

CHAPTER I

Introduction

1.1 Background

Afghanistan is completely a landlocked, dry, multiethnic country located in the heart of south-central Asia bounded to the east by Pakistan, to the west by Iran, to the north by the central Asian countries of Turkmenistan, Uzbekistan, and Tajikistan (Fig. 1-1). It has also a short border with China to the northeast side. The majority of the land (*i.e.,* more than 70 %) in Afghanistan is mountains. Most of Afghanistan's land is situated between 600 to 3000 meters in elevation (Dupree et al, 2022). The central mountains such as the Hindu Kush mountains with 414000 square km are a part of the Himalayan chain that is mainly situated in Afghanistan. Some peaks of the Hindu Kush Mountain rise above 6400 meters. Soil quality varies in different parts of the country. The central highlands have desert-steppe or meadow-steppe types of soil.

The northern plains have extremely rich, fertile, loess-like soils, while the southwestern plateau has infertile desert soils except along the rivers, where alluvial deposits can be found. Erosion is much in evidence in the central highlands, especially in the regions affected by seasonal monsoons and heavy precipitation. In general, the climate ranges from arid to semi-arid, with a large temperature difference between altitude and between warm and cold seasons. In the mountains the annual mean precipitation increases from west to east; there, as in the southeastern monsoon region, it averages about 400 mm. National precipitation extremes have been recorded in the Salang Pass of the Hindu Kush, with the highest annual precipitation of 53 inches 1,350 mm, and in the arid region of Farah in the west, with only 75 mm per year. Because of the geophysical location, types of soil, and weather extreme in the country, almost

all parts of Afghanistan are very susceptible nearly to all kinds of natural hazards, including earthquakes, floods, drought, sandstorms, snow avalanches, and landslides (Shroder, 2014).

Figure 1-1. Presents the location of Afghanistan and neighboring countries.

About 30 % of the population in Afghanistan is living in Urban areas (Dupree et al, 2022). The majority of urban settlements chose to live along the roads from Kabul southwestward to Kandahar and Herat, northwest to Mazar-i-Sharif, and northeast to Badakhshan. The rural population which is the majority (*i.e.,* 70 %) of the population are living as farmers and nomads over the rest of the country which is distributed unevenly along the rivers. The most heavily populated part of the country is between the cities of Kabul to Charikar, Kabul to Kandahar, and Herat (Dupree et al, 2022). Typical types of buildings in urban areas are made of Masonry, precast (*i.e.,* made during the Soviet invasion), RC and RC-with shear walls. On the other hand, Rural settlements (*i.e.,* most of them farmers) usually sparsely live along valleys of major rivers. The majority of their houses are built from local materials (*i.e.,* stone, mud. etc.) by themselves without the help of professionals or any engineering designs. Even in most of the cases government or local government does not

involve in the whole process of building particularly in rural areas. Because of the poor economy, continuous war, and unstable situation, Afghanistan remains among the country with fewer surveys, and research about any aspects particularly natural disasters. There is no proper urban or rural settlement map or micro zonation map, that shows the natural disaster-prone area. Therefore, usually, they don't have the knowledge to choose a safe place regarding natural disasters. Most of the time they are building their houses along the path of floods, or in landslide-prone areas. Another reason for unlawful, non-engineered urban sprawl is the rapid increase of population after 2001 as a result of mass returning to the country. The rapid increase of population in urban areas like Kabul and other major cities was a challenge for the government in terms of building shortages. The landlords and local government start selling land without a proper urban master plan. As a result of this rapid increase in building construction, most of the settlements build their houses in risky areas such as flood and landslide-prone areas.

Landslides (Zhang et al., 2015) and frequent impactful floods (World bank, 2017) are among the most widespread natural hazards. Most of the time the so-called hazards pose threat to the unlawful weak settlements built from local materials without any proper design and hazard assessments. Since 1980, disasters caused by natural hazards have affected 9 million people and caused over 20,000 fatalities in the country (World Bank, 2017). Providing natural disaster assessments such as landslide assessments and flood mapping assessments is the most critical risk information that paves the ground for the government, policymakers, and even people themselves. Because having access to risk maps makes the public decide to build their house in the proper place and more importantly increases the resilience of future and even existing reconstruction to neutral hazards which can save lives and livelihoods.

It has been clear that the risk related assessment is very advantageous, however collecting data in an insecure country like Afghanistan is almost impossible to conduct the on-

site survey. Hence, taking advantage of remote sensing information is crucial for monitoring land use, and land cover change. The advantages of remote sensing include the ability to collect information over large spatial areas; characterize concerned features and monitor their changes over time, and the ability to integrate this data with other information to aid decision making without putting the life of the surveyor at risk.

1.2 Literature Review

1.2.1 Landslide Studies in Remote Sensing

Landslides induced by heavy rainfalls and earthquakes are among the most common geohazard phenomena that frequently occur in mountainous regions, constitute one of the major hazards responsible for Interruption and destruction of transport-related structures, industrial and hydropower plants, and cause loss of lives worldwide. Recent studies show that the number of locations, activity, severity, frequency of landslides, and their social and economic impacts are increasing (Dai et al., 2002; Haque et al., 2019; Petley et al., 2005; Schuster et al., 2001). As an example, between 2004 and 2010, 2,620 deadly landslides occurred, bringing the lives of 32,322 people to an end. Likewise, the result of a published report by the International Federation of Red Cross and Red Crescent Societies (IFRCRCS, 2001) shows that 42 % of the natural hazards related incidents are triggered by landslides, which annually account for millions to billions of U.S. dollars in economic losses in three countries like Canada, Nepal, and Sweden alone. Wenchuan landslides occurred in Sichuan, China, and were one of the deadliest landslides which led 2,000 people to death (Yin et al., 2009).

Afghanistan is considered a country prone to several geomorphological hazards such as earthquakes, landslides, flooding, drought, avalanches, and man-made disasters. Geomorphic hazards are a notable feature in Afghanistan that kills dozens every year along with other burdens coming from deadly insecurity, unsustainable economy, crippling poverty, and chronic health problems. Safety and economic problems made Afghanistan among the countries with only a little research on landslides. Therefore, the exact location and number of landslides prone areas all over the country have not been specified yet, but as per records of the United Nations Office for the Coordination of Humanitarian Affairs (UNOCHA, 2020) Of all-natural disasters reported in Afghanistan between 2012 and 2020, landslides accounts for

only 6.77% of total natural hazard events which 30.33 % of all Geohazards related deaths being attributed to landslides. Of all recorded (UNOCHA, 2020) landslides in the country between 2012 to 2020, 41.8% occurred in Badakhshan, and surprisingly, landslide events in Badakhshan account for 16.25% of all-natural disaster incidents (UNOCHA, 2020). It accounts for 53.6% of all recorded landslide-related deaths in Afghanistan. As reported by (Gupta, 2010) Badakhshan province is Identified as a high-priority province due to its greater susceptibility to landslides.

Furthermore, (Shroder, 2011a) examined 22 mass movements in northeast Afghanistan and recognized them as loess landslides after due consideration and analysis. A similar study (Shroder, 2011b) found 34 large-scale loess slope failures on the north, west, and northwest slopes of Badakhshan. According to (UNCHA, 2020) From 2012 to 2020, more than 14 thousand individuals were affected by Landslide hazards in Badakhshan province alone, and as reported by (Gupta, 2010) Badakhshan province is a high priority province due to its greater susceptibility to the landslide. The majority of Afghanistan's land is covered by mountains. Hence, due to the insufficient flat area in most of the cities, people constructed their houses along the hills. For instance, Abi-Barek is one of the districts, located in a suburb area that can be counted as a landslide-prone area surrounded by steep slope mountains. A massive landslide occurred on May 2, 2014, in the Abe-Barek area buried all houses with their owners along its path and affected thousands of people and had a considerable impact on the fragile economy of Afghanistan.

Badakhshan province's high susceptibility to landslides led us to conduct a study on one of the occurred landslide events areas using remote sensing. In this research, the attention spotlight is on the Abe-Barek landslide incident which occurred on May 2, 2014, in Badakhshan, Afghanistan, and bring great international attention due to its large dimensions and catastrophic damage. In accordance with United Nations Institute for Training and

Research (UNITAR/UNOSAT, 2014; Zhang et al., 2015) the death toll ranges from 300 to more than 2700. Based on an initial comparison of high-resolution worldView-2 satellite imagery of pre-and post-event a total of 87 structures were buried by a mass of soil (UNITAR/UNOSAT, 2014; Zhang et al., 2015). Moreover (UNITAR/UNOSAT, 2014) after investigation and comparison of different areal images conclude that in the same area previously mass movements occurred and are highly likely to occur again. Zhang et al., (2015) conducted landslide susceptibility assessments in Abe-Barek landslide affected area using a low-resolution of 90m SRTM elevation data and DEM derivatives with great limitation of lacking landslide inventory data.

In order to prepare a suitable response to landslides, various slope reinforcement structures, such as retaining walls, anti-sliding piles, and anchor cables have been commonly used. Knowing the volume of deformed soil is a key index to knowing the magnitude of a landslide, conducting accurate design of slope reinforcement structures, analyzing and evaluate accurately the risk assessments, and predicting the secondary risks triggered by landslides. Compared to calculating the area of a landslide, which is usually easily determined by aerial imagery, quantifying the volume of specified landslides is a challenging task and requires detailed information on the surface and sub-surface geometry profile of the deformed soil (Malamud et al., 2004; Chen et al., 2014; Chen et al., 2019)

There are several methods available that can be used to quantify the displaced soil volume. In some studies, the landslide volume was calculated using combined algebraical approaches (e.g., Integral approximation methods,) in situ profile surveying approaches, and geophysical or drilling techniques (Chen et al., 2014; Chen et al., 2019). In some other studies, the volume of landslides was obtained using statistical approaches (Brunetti et al., 2009; Kovacs et al., 2019; Xu et al., 2016; Zekkos et al., 2017; Larsen et al., 2010). Several studies thus far have claimed that there is a strong relationship between total failure area with the

relevant volume of landslides (Malamud et al., 2004; Guzzetti et al., 2009; Larsen et al., 2010) conventional surveying methods are not suitable for large landslide areas (Kovacs et al., 2019) because in case of urgent hazard assessments it takes considerable time and is not budget-friendly. Another method of quantifying the volume of a landslide material that is the preferred method for this study is remote sensing (e.g. aerial photo surveying, LiDAR, and InSAR techniques) which can provide large-scale data, covering extensive areas. It gives the scientist ability to collect information and images of the Earth's land to characterize the natural features or physical objects on the ground; to observe surface areas and objects on a systematic basis and monitor their changes over time; and the ability to integrate this data with other information to ease the decision-making with urgent support and rescue operation. A general overview of remote sensing techniques for landslide studies and their beneficial service to society has been widely presented (Scaioni et al., 2014). The increasing availability of satellite data, high efficiency, enhanced performance, great accuracy of the computational process, and appropriate output of remote sensing tools led researchers to take advantage of it with greater reason. Thus, every day there is the development of fresh methodologies in numerous sectors, particularly in the study of landslides. Furthermore, Remote sensing techniques provide a potentially low-cost alternative to field-based assessment, monitoring, early investigation, and remedial work planning for different disasters, especially landslides.

In order to quantify the volumes of a displaced material, identifying the location of slope failure is very crucial. identification of a landslide area is commonly performed by utilizing change detection techniques on remote sensing images. Identifying the significant change in a set of images of the same location captured at different time frames is defined as a change detection technique (Singh, 1989; Asokan et al., 2019). Numerous change detection techniques have been introduced, among all, the image differencing (Sohl, 1999), DEMs of difference (Williams, 2012), Normalized difference vegetation index (NDVI) (Ghandhi et al.,

2015; Miura, 2019), principal component analysis (Fauvel et al., 2009; Sabokbar et al., 2014), post-classification comparison (Rogan et al., 2004), spectral mixture analysis (Somers et al., 2011) and artificial neural networks (ANN) (Lei et al., 2019; Ermini et al., 2005; Yilmaz et al, 2009; Mas et al., 2008) become more prominent techniques. A difference of elevation between pre-and post-event DEMs (DEMs of difference: DoD) has been used to identify the location of the affected areas and quantify the displaced soil volume (Tsutsui et al., 2007; Martha et al., 2010; Miura, 2019; Lin et al., 2020). Among various remote sensing data sources, the light detection and ranging (LiDAR) technique can produce a reliable estimate of morphological change (Jaboyedoff et al., 2012). However, LiDAR observations have been rarely conducted in remote areas such as the Abe Barek area. The satellite image-based approach is more feasible to assess the natural disasters in such remote areas. DEM can be created from a stereo analysis of multiple satellite images with different off-nadir angles. In the case that a set of high-resolution stereo pair satellite images is available before and after the disaster, the DoD analysis can be performed by developing pre-and post-event DEMs.

In order to quantify landslide volumes from DoD, the geometries of the obtained DEMs need to be registered accurately. However, the DEM errors of height values are found in many cases, even when the data is geometrically registered. Previous studies revealed that the uncertainty, including registration-noise or locational errors in multi-temporal DEMs, would cause the miscalculation of soil volumes(Chen et al., 2014; Hsieh et al., 2016). These errors arise from many factors such as the quality of original data, interpolation algorithm, projection method during the DEM creation process, etc. (Ostrowski et al., 1989). The horizontal misregistration between DEMs would be one of the major causes of the uncertainty in the DoD analysis.

Various researches have given special attention to the development of advanced registration techniques not only for aerial images (Foseca et al., 1996; Le Moigne et al., 2002;

Sarvaiya et al., 2011) but also for multi-temporal DEMs(Chen et al., 2014; Hirakawa, 2006; Miura, 2015; Jaboyedoff et al., 2012) addressed the use of ground control points (GCPs) to refine the generic sensor's orientations. The collection of GCPs is time-consuming in an urgent time of disaster. Chen et al. (2014) proposed a mass balance model to accurately correct two DEMs and quantify the landslide's accumulated volume. However, the mass balance calculation would be difficult in affected areas where collapsed soils flowed into buildings and the downstream rivers. Hirakawa (2006) also proposed an optimization-based method to automatically correct the geometrical errors in multi-temporal LiDAR-derived DEMs by assuming unique linear errors throughout the area of concern. It would be difficult to correct the geometries of the DEMs when substantial nonlinear distortions are found in the area of interest. Those previous studies indicate that misregistration caused by nonlinear distortions in multi-temporal DEMs still remains an open problem. Miura, (2015) presented a nonlinear mapping technique for reducing horizontal locational errors between LiDAR-derived DEMs and estimating the displaced volumes of debris flows. However, the applicability of the technique for a landslide in satellite image-derived DEMs, and the parameter selections in the technique were not fully discussed in the previous study (Miura, 2015).

In current study, the proposed methodology from (Miura, 2015) has been followed to present the nonlinear mapping technique's applicability in reducing the registration noise of the multi-temporal DEMs to estimate the volume of the Abe Barek landslide. A set of high-resolution DEMs generated from stereo pair satellite images was analyzed. The nonlinear mapping technique was applied for reducing the nonlinear distortions in the DEMs. Unlike the previous work (Miura, 2015), here in this study, particular attention was given to illustrating the efficacy of the method using both statistical approaches and profile cross-sections. The volume of the landslide was estimated from the DoD corrected by the nonlinear technique.

1.2.2 Flood Studies in Remote Sensing

Flooding is one of the most destructive and recurring natural hazards on the planet. It causes catastrophic damage and threats to life, property, and cultural heritage. Floods affect more people than any other sort of weather-related disaster and are a leading cause of natural disaster fatalities worldwide (UNISDR, 2015). It is triggered by natural factors such as heavy rainfall, overflowing of water onto dry land in the floodplain, rapid melting of snow, and the failure of man-made structures such as dams and levees. Floods have had significant impacts on the human economy, as well as indirect effects on economic growth and societal well-being. Floods disproportionately have high impacts on the poorest and most vulnerable people (Freebairn et al, 2020). Afghanistan is vulnerable to a variety of hazards, including earthquakes, flooding, drought, avalanches, and man-made calamities (Atefi and Miura, 2021). Due to safety and economic concerns, there is virtually little emphasis on research. As a result, very little research has been conducted on natural catastrophes, particularly flood disasters. Of all the reported natural catastrophes in 2020, floods directly affected about 50,000 individuals in Afghanistan (IFRCa, 2021) More than 3,000 people were severely affected by the flood in Charikar, Parwan province, during the same year (IFRCb, 2021). A destructive flash flood ravaged Charikar city on August 26, 2020, severely damaging the residential area and killing hundreds of people. Nevertheless, very few studies have been conducted to explore and identify the flood-affected areas in Charikar. Consequently, the precise location of flood-inundated places, as well as the degree of flood damage area, remains unknown to this day.

Although flood control is a tough task, minimizing the consequences is a viable, necessary, and smart option (Khosravi et al, 2019; Mius et al, 2015; Wu et al, 2017; Zaji et al, 2018). It is never easy to figure out and choose the ideal strategy and policy to deal with floods. However, it is possible to reduce these losses and dangers by notifying the public ahead of time and providing credible information, as well as providing proper flood mapping of flood-prone

areas that are experiencing the most severe floods. Flood maps prepared in flood-prone areas utilizing remotely sensed data are very safe, economical, and timesaving, and they play a significant role in predicting, preparing, preventing, and mitigating flood damage. Furthermore, flood monitoring with satellite imagery has the advantage of covering a vast area and being reasonably quick to collect and analyze data. Researchers often benefit from the availability of both optical and radar remotely sensed imagery data for flood monitoring and mitigation methods. The Charikar event was a flash flood caused by severe rainfall that swept downward from the top of the mountain. Since no water has accumulated downstream for a long period, employing optical satellite photos is considered ideal. As a result, in this study, uses optical satellite data to assess flood inundated sites in Charikar.

Several approaches and methodologies based on pixel and object-oriented methods can be used to detect water using optical satellite data, including supervised and unsupervised classification methods; transformation of spectral channels; texture analysis; visual interpretation; single channel thresholding; and channel ratio use. In this approach, water indicators are extremely beneficial. Their implementation is contingent on the formulation of a threshold value that differentiates water pixels from those representing other forms of land cover.

Several approaches for extracting water bodies from remotely sensed data have been developed by researchers. (McFreeters, 1996) proposed the Normalized Difference Water Index (NDWI) to detect water features from Landsat TM using band 2 and band 4. (Rogers et al, 2004) introduced a new NDWI for extracting water from Landsat TM utilizing bands 3 and 5. To extract surface water bodies from raw digital Landsat data, (McFreeters, 1996) proposed a threshold value of zero, with all positive NDWI values categorized as water and negative values classed as non-water. This threshold, on the other hand, makes it impossible to distinguish between built-up surfaces and water pixels. As a result, (Xu, 2006) developed the

Modified Normalized Difference Water (MNDWI) using Landsat TM bands 2 and 5. When compared to other indicators, the MNDWI indicator has a stronger ability to reduce disturbances generated by buildings, vegetation, and soils (Xu, 2006). (Feyisa et al, 2014) developed the Automated Water Extraction Index (AWEI) to increase the accuracy of water extraction in locations containing shadows and dark surfaces. The MNDWI has been used to create a simple Enhanced Water Index (EWI) by (Wang et al, 2014). Water surfaces can be identified from background information such as deserts, soil, and vegetation. For the extraction of surface water from Landsat data, (Rokni et al, 2014) examined the characteristics of NDWI, MNDWI, NDMI, WRI, NDVI, and AWEI in applying a novel surface water change detection process based on the principal components of multi-temporal NDWI. Surface water was retrieved from the indices using a trial-and-error thresholding methodology. The overall accuracy and kappa coefficient were used to examine the efficacy of each water body extraction procedure, and NDWI was found to outperform other measures. These indices have also been used in a multitude of scenarios, such as surface water mapping (Feyisa et al, 2014; Duan et al, 2013), land use and land cover change assessments (Dayranche et al, 2010), and ecological research (Poulin et al, 2010).

Numerous researchers have utilized the Normalized Difference Vegetation Index (NDVI) to detect land cover change since the NDVI shows positive values for vegetation, values close to zero for bare soil, and negative values for water (Huete et al, 1997; Escuin et al, 2008; Sidi et al, 2020). Many studies show that AWEI and MNDWI achieved better results and more stable thresholds than the NDVI index (Huang et al, 2018). However, these indices are frequently used by the researchers to extract water bodies such as lakes, canals, waterways, ponds, and so on. Unlike current study, they never employed the so-called spectral indices in flash flood scenarios where there is no standing water except the damaged area as a result of the flood.

Although modern satellites have provided a superior solution over traditional methods in monitoring water surfaces, manually downloading and processing imagery associated with large study areas or long-term time scales is time-consuming. Most of the traditional methods are not straightforward, which makes them technically challenging for the user to apply because the extra procedures like preprocessing (DeVries et al, 2020).

Google Earth Engine (GEE), a planetary-scale platform for earth science data and analysis developed by Google, has been utilized in this study for applying the NDVI technique developed in (Scheip et al, 2021). The GEE has enabled the development of global-scale products, tools, and services using temporal earth observation data such as Sentinel-2. The GEE platform provides a fast-forward solution for these kinds of big data problems. The GEE has been used to conduct various global and regional scale studies, including regional land cover mapping (Saah et al, 2019), surface water mapping (Phongsapan et al, 2019), accessing food security situations (Poortinga et al, 2019), settlement and population mapping (Patel et al, 2014), and other applications (Mutanga et al, 2019). Hazard Mapper is an open-access application developed in the GEE (Scheip et al, 2021) and has been used in many case studies and in different countries to delineate different kinds of natural hazards, including floods.

Although the model's original developer (Scheip et al, 2021) never used it to estimate floods in non-vegetated environments such as high altitudes or semi-arid to arid regions, this research is looking into it to see if it can be used to locate flood inundated areas in non-vegetated, data-scarce regions in Afghanistan. The flood in Charikar was most likely caused by torrential rain, which caused enormous stones and debris to slide along the path of the stream channel, which was blocked by residential residences, resulting in devastating debris flows that ruined homes, infrastructure, and properties. There were no reports of water accumulation during or after the flood event, indicating that the water was moving extremely quickly along the valley from uphill to the flat areas of the mountain. In this study, the GEE was used to automatically identify

Charikar flash flood flooded areas using a change detection method based on pre- and post-event NDVIs in optical satellite Sentinel-2 pictures. The detected inundation area's accuracy has been evaluated and compared with flood maps derived from visual image interpretations and government reports. Furthermore, the NDVI time series has also been used to measure changes in NDVIs two years after the event date to follow the recovery process in the affected area. Moreover, a digital elevation model (DEM) has been also used to examine flow path assessment of gravitational hazards at a regional scale (Horton et al, 2013) in order to assess the feasibility of the simulation technique for finding and predicting vulnerable regions in future flood occurrences.

1.3 Problem Statement

Slope instability and flood issues are the problems that have to be prioritized for finding a solution to decrease the risk at a tolerable level either by using effective engineering techniques or other effective measures. A budget-friendly way to help decrease the impact of landslides and floods is to identify, assess and develop methods to rapidly can detect in an emergency period of hazards. Assessments of floods and landslides can be possible through on-site surveys and remote sensing. However, remote sensing analysis is safer in terms of securing and faster in terms of efficiency. The assessments of floods and landslides using efficient remote sensing techniques has also been presented. However, there is the following problem applying remotely sensed data:

1. In order to make sure that, landslide and flood assessment analysis is being done properly, it needs to be precisely compared and confirm with field data. In order to carry out such validation analysis; it is necessary to have both precise and sufficient GCP (Ground control points) of the study area. GCP collection can be done by in-situ surveying. Surveying in an unsafe country like Afghanistan is not recommendable. To solve this problem, a method has been proposed that answers the problem very well.

2. Availability of data in remote sensing analysis for a specific study area is crucial. There is very less high-resolution satellite imagery available during the landslide time which occurred in Abe-Barek. The available data was also not observed by one satellite. This is also a challenge because two satellite images with different sensors and resolutions cannot be directly used for the analysis.
3. As stated earlier, for landslide analysis a methodology is proposed that only could be applied with the high-resolution stereo pair satellite imagery. On the other hand, for flood analysis, high-resolution satellite imagery was unavailable to carry out the same methodology as conducted in landslide analysis. Therefore, for the freely available medium resolution satellite image, different methodology was proposed.

Concerning all the mentioned problems, it becomes the purpose to come up with methods that fit very well by performing remote sensing analysis. To do this, understanding knowledge of the engineering characteristic of each problem is vital.

1.4 Research Objectives

The aim of the study is set to fulfill the following objectives from two case studies:

1. The objectives of Abe-Barek landslide assessment analysis are as follows:
    - Applicability of nonlinear mapping technique on minimizing geometric errors
    - Validation of nonlinear mapping algorithm by comparison of several descriptive and graphical parameters.
    - Landslide detection and volume estimation by using corrected DEM based on a nonlinear mapping method.
    - Validation and comparison of the obtained volume of displaced material with previous studies.
    - Landslide hazard assessments to determine the number of affected houses.
2. The objectives of the Charikar flood assessment analysis are as follows:
    - Using Sentinel-2 images in Google Earth Engine to automatically identify the Charikar flash flood inundated area.
    - Rapid mapping of the flood soon after the event with fewer post-event images.
    - To detect and estimate the area of flood inundated area with freely available low-resolution satellite imagery.
    - Evaluate the performance of the relative normalized vegetation index using the google earth engine on flash floods that occurred in non-vegetated environments.
    - Accuracy assessment of the method

To fulfill the above objectives following computer-based software is used:

- Fortran 77 code-oriented program.
- Google Earth Engine (GEE), a JavaScript API-based program.
- QGIS
- ENVI

1.5 Organization of the Dissertation

This dissertation is comprised of 5 chapters. The contents of each chapter are briefly summarized as follows:

1. **Chapter 1** provides a general context of the study including background, problem statement, and research objectives.
2. **Chapter 2** is covering an overview of the natural disaster such as floods, earthquake, ladslide, snow avalanches, and droughts in Afghanistan.
3. **Chapter 3** this chapter is focusing on the assessment of landslide using nonlinear mapping technique. This chapter contains a detailed explanation regarding, acquiring satellite data, features of the obtained data, DEM extraction, alignment of the DEMs, detailed explanation of non-linear mapping methodology, analysis of Abe-barek landslide, its applicability, estimation of the landslide area and volume using remotely sensed data. Moreover, it covers a comparison between previously landslide volume estimation and the current study.
4. **Chapter 4** This chapter covers the assessment of flood using rdNDVI. This chapter covers the details regarding, acquiring satellite data, features of the obtained data, DEM acquisition, detailed explanation of spectral indices, relative Normalized difference Vegetation Index methodology using Google Earth Engine, its applicability, propagation of flood debris mapping in the study area, estimation of the landslide area using remotely sensed data. Moreover, it covers a comparison accuracy assessment using visual interpretation and government survey reports.
5. **Chapter 5** gives information about the general conclusion and future work of this study.

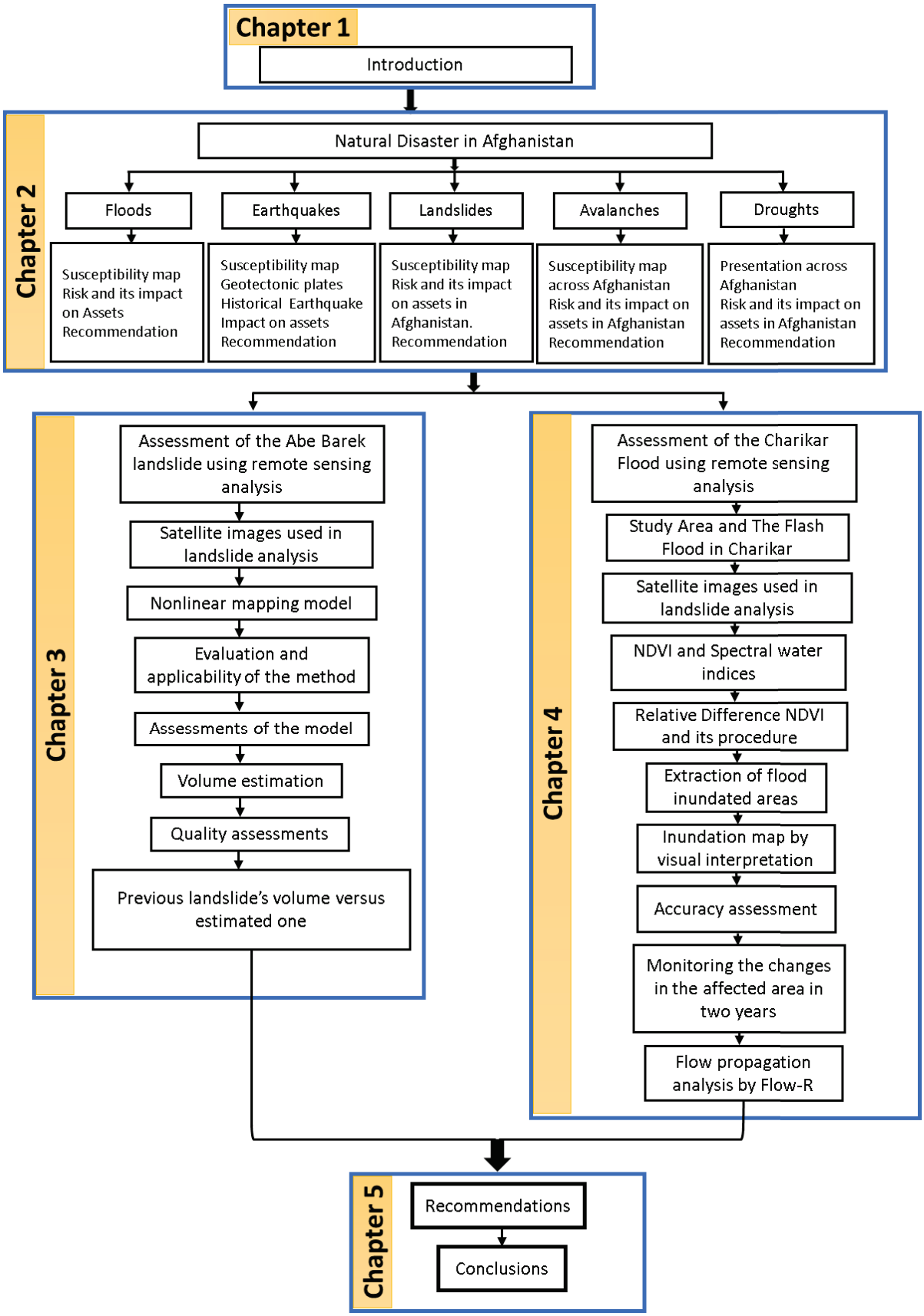

Figure 1-2. Outline of the dissertation.

CHAPTER II

Natural Disaster in Afghanistan

2.1 Introduction

Afghanistan with complex topography, and varying climate conditions with highly fluctuating temperatures between warm and cold in all seasons, is highly prone to a variety of natural hazards (UNDRR, 2020). Exposure of people and assets to natural disasters has been increased due to political instability, war, weak institution, less control of the government on rapid urbanization, and poor planning in the country along with the Covid-19 pandemic and insufficient investment in disaster risk reduction strategies further contributed to increasing the frequency and severity of various natural disasters. Based on World Risk Report (2021) Afghanistan is ranked third for the lowest coping capacity, among highest vulnerability, and stands among the countries with a high lack of adaptive capacity (Fig.2-1). It indicates that any small shock or disaster can easily cause loss of life and properties due to high vulnerability and low coping capacity. Also, Afghanistan ranked second place in terms of natural disaster-related fatalities between 1980-2015. Moreover, in Afghanistan, about 9 million people have been affected and 20000 has been lost their life since 1980 by natural disasters from which floods are the most frequent and damage-causing hazard in the country (World Bank, 2017). Intense rainfall, rapid snow melting, and less vegetation coverage of land in mountainous areas mainly contribute to flood inundation, and urban flooding is mostly a problem in major cities such as Kabul, Mazar-i-Sharif, and Herat due to poor drainage systems (World Bank, 2017). Afghanistan is also highly vulnerable to earthquakes. It is among the 10 % of countries with the highest expected annual earthquake mortality risk. (Shi, et al, 2015). The history of devastating earthquakes in the country ranges more than 4000 years (Boyed et al, 2007). Of all-natural disasters, historically most of the fatalities occurred in the earthquake. Since 1980

more than 10000 people have lost their lives because of earthquakes. (World Bank, 2017). From 1997 to 2007 earthquake-related death has been reported for 7000 people, from which 4000 people died in the Nahrin earthquake in May 1998 (Boyed et al, 2007). As per reports of the world bank, 2017 on average earthquakes cause 80 million US dollars in damages on average annually in Afghanistan.

Furthermore, in Afghanistan with a mountain dominant landscape, landslide susceptibility is classified as high. Having heavy rainfall patterns, high slope terrain, type of geology, soil, land cover, and more importantly earthquakes make the landslide event a frequent hazard phenomenon. Based on (DRR & World Bank, 2017) over 3 million people in Afghanistan are under high exposure to landslide hazards. As per records of the United Nations Office for the Coordination of Humanitarian Affairs (OCHA, 2020) from all reported natural disasters in Afghanistan between 2010 and 2017, landslides only account for 3.6% which makes 16.8% of all Geohazards related deaths. As reported by (Gupta, M.,2010) Badakhshan and with other three northern provinces are identified as high priority provinces due to their greater susceptibility to landslides. Drought is also threatening the lives of nearly three million Afghans (NRC, 2021). Severe weather, including heavy rain and snow falls, has been affecting the central, northern, and northeastern provinces of Afghanistan causing casualties and damage. Avalanches frequently happen almost every year and are triggered after a heavy snowstorm and long-term snowfalls. According to the (World Bank, 2017) reports over two million people are under high threat of avalanches in Afghanistan. Avalanches most often happen in northern parts of the country. The 2017 avalanches were a series of avalanches that occurred in different parts of the country and reportedly killed 100 people (BBC News, 2017). The DRRR estimates show that more than 10000 km of roads which is more than 15 % of all roads in Afghanistan are under high exposure to avalanches, it contains the key transport route

such as the Salang pass which connect the northern province to Capital Kabul. (DRP & world bank, 2017).

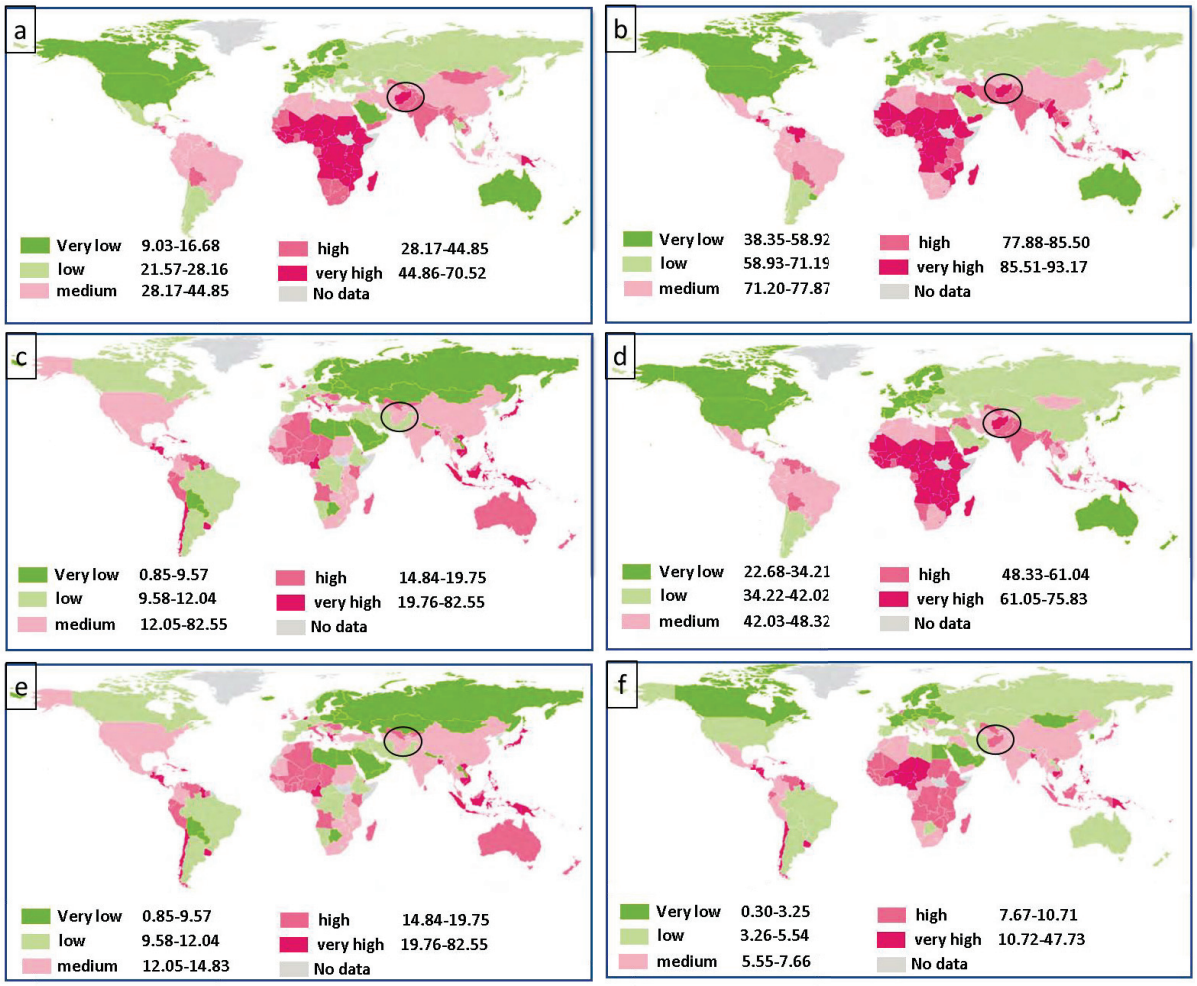

Figure 2-1. World disaster-related maps, a) susceptibility map b) lack of coping capacities c) lack of adaptive capacities d) vulnerability map e) exposure of the population to the natural hazards; f) world risk index as a result of exposure and vulnerability (WorldRiskReport, 2021)

Based on report of (OCHA, 2022), from January 2012 to May 2022, 1.6 million people were affected by natural disasters throughout Afghanistan. A total of 13 provinces out of 34 experienced some kind of natural disaster during the period (Fig. 2-2). Among all the natural disaster flood and flash flood seems to be more frequent. (Fig.2-2). On average the so-called disasters affect 40000 people every year.

This chapter will cover four main frequent natural disasters in Afghanistan such as floods, landslides, earthquakes, avalanches, and droughts in detail:

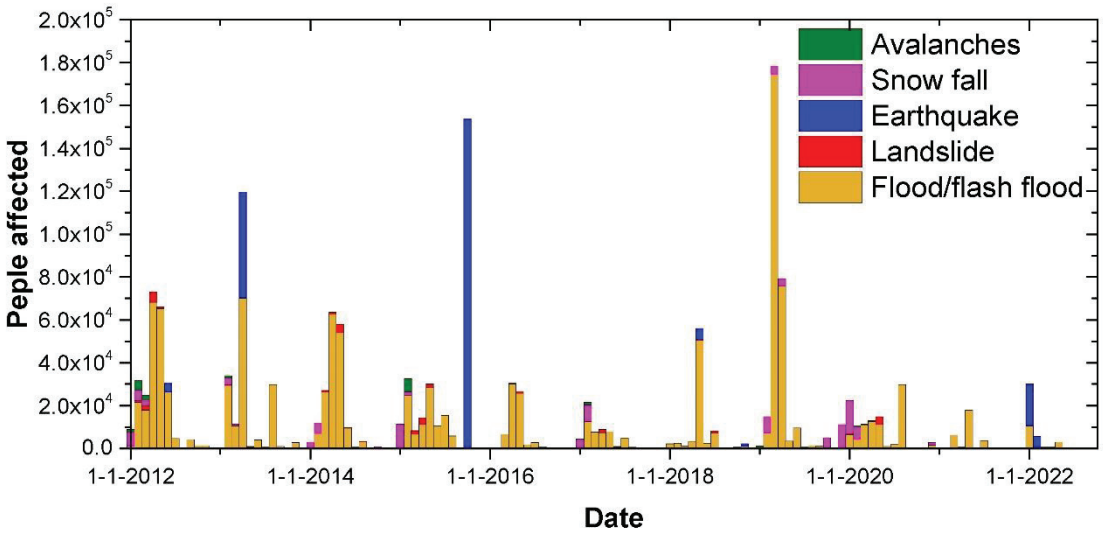

Figure 2-2. Presents number of affected people from different types of natural disaster from 2012 to 2022 (UNDATA).

2.2. Floods

Flood and flash flood are the most frequent types of natural disaster which happening in different parts of Afghanistan and causing loss of life and properties. As can be seen in Fig. 2-3 almost all parts of the country including urban areas and countryside areas are flood prone areas. However, flood impact on population is comparatively low on flat areas compared to the mountainous areas. The main cause of flood in rivers mainly occurs due to the heavy rainfall and snow and glaciers melt. It is noteworthy to mention that lack of vegetation and contributes to the occurrence of flooding. Flooding in urban areas is typically triggered by intense local rainfall and lack of drainage systems. Floods in Afghanistan cause more deaths than other countries due to low socio-economic development, lack of awareness, lack of coping mechanisms and lack of protection capacities.

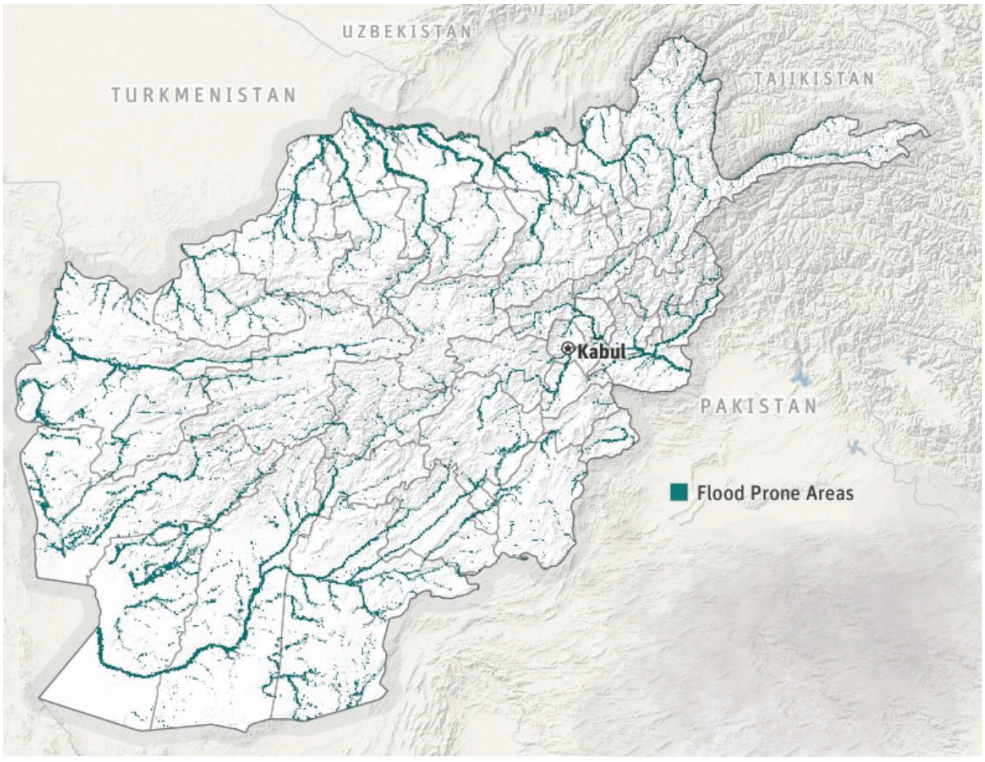

Figure 2-3. Presents the flood prone areas across all Afghanistan. (World Bank, 2017).

Figure 2-4 presents the flood hazard map of all Afghanistan. As can be seen in Fig 2-4 Kabul with high density of population has most affected population because of floods. In Kunar Province flood has high impact on population and GDP.

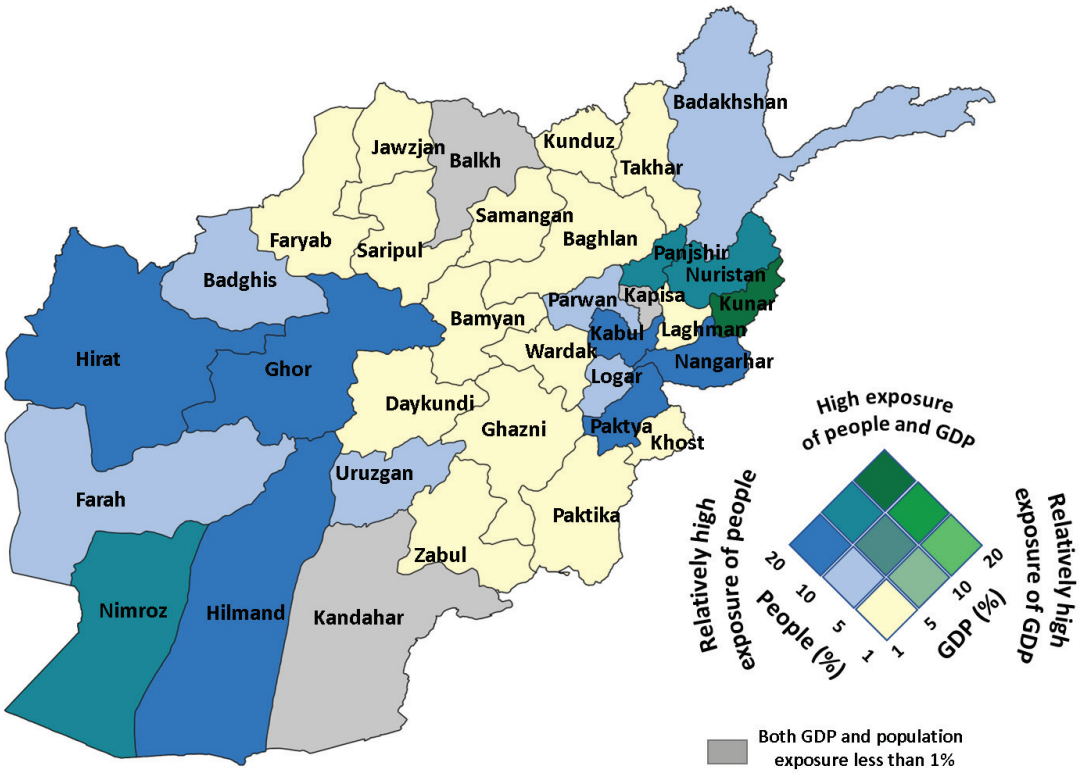

Figure 2-4. GDP and Population exposure to floods. (Data from World Bank, 2017)

2.2.1 Flood Risk and its impact on assets in Afghanistan

The exposure assessment of assets for floods provides essential information about the assets, which are located in the flood hazard prone areas. The information created from the assessment are important and useful to and policy makers as basis for plans and interventions on preparedness, early warning, response recovery, and mitigation. In Afghanistan floods, primarily affecting people, private buildings, roads, healthcare facilities, education related buildings and facilities, and energy related facilities (Fig. 2-5). In Afghanistan floods, primarily affecting people, private buildings, roads, healthcare facilities, education related buildings and facilities, and energy related facilities. Moreover, from Fig. 2-5 it clearly can be noticed that the cities with largest densities of any assets having more exposure to the flood.

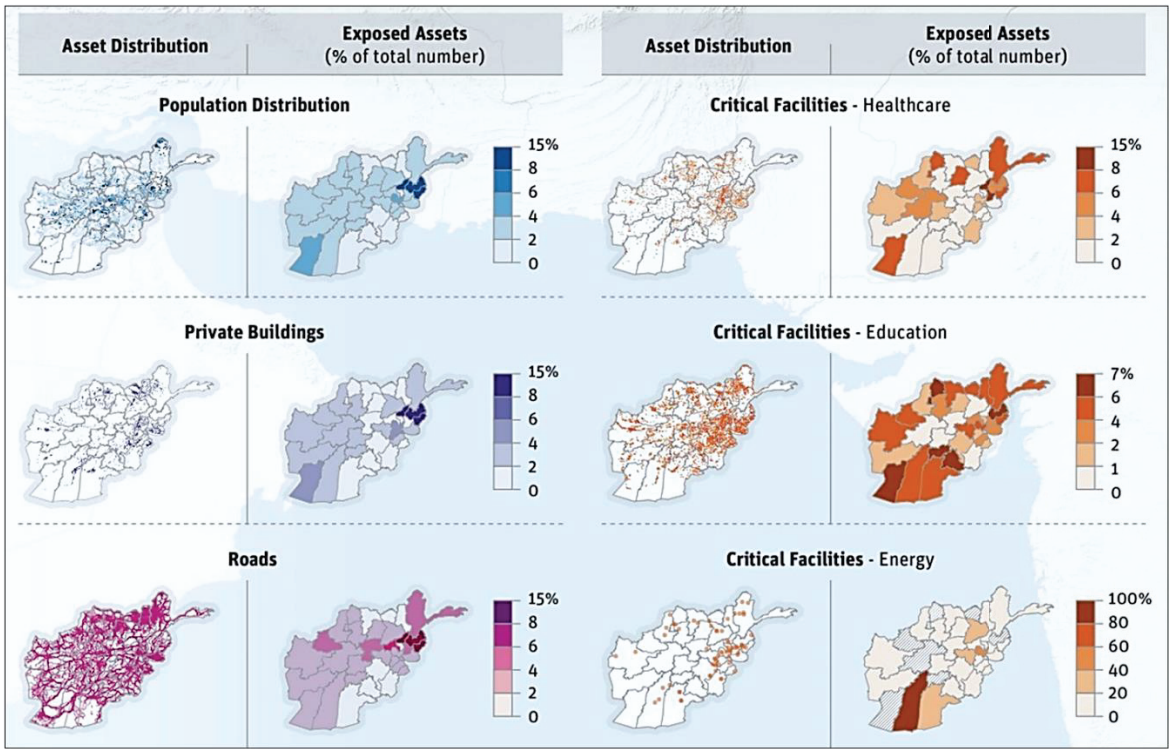

Figure 2-5. Presents the distribution of assets and its exposure to the flood across all Afghanistan. (World Bank, 2017)

For example, Kabul province with highest population density has the highest exposure of the population to the flood. The percentage of population exposed to flood ranges from 8 to 15 percent. Likewise, private buildings, roads healthcare and education related buildings are found to be exposed in flood prone areas.

2.2.2. Recommendations

As discussed, floods frequently occurring in different parts of the country causing significant damage and has the potential to disrupt the livelihood throughout the country. There are various flood risk management methods that can reduce the impacts they can cause.

- Flood risk-reduction measures particularly building infrastructure like strengthening dikes and retrofitting buildings would help improve the flood protection in cities and rural areas.
- Avoid constructing houses in floodplains and flood prone areas as much as possible.
- Because of lack of government control on urban planning and building construction majority of the buildings are being built in riverbanks and flood plains. Increasing the natural space along the riverbanks would help reduce the occurring of flood from rising of the river water.
- Lack of drainage system in all Afghanistan including big cities like Kabul, Mazar-i-Sharif. etc., cause blockage of rainwater.
- Preparing flood inundation maps will prevent people not to construct public and private property in flood prone areas.

2.3. Earthquake

Afghanistan is located in a tectonically active region of the world. Each year Afghanistan experience moderate to strong earthquakes, causing massive human casualties, loss of life and damages to homes and infrastructure because many dwellings are not as stable or well-built. Afghanistan situated between Indian and Eurasian plates Fig 2-6, which area moving upward and downward direction respectively.

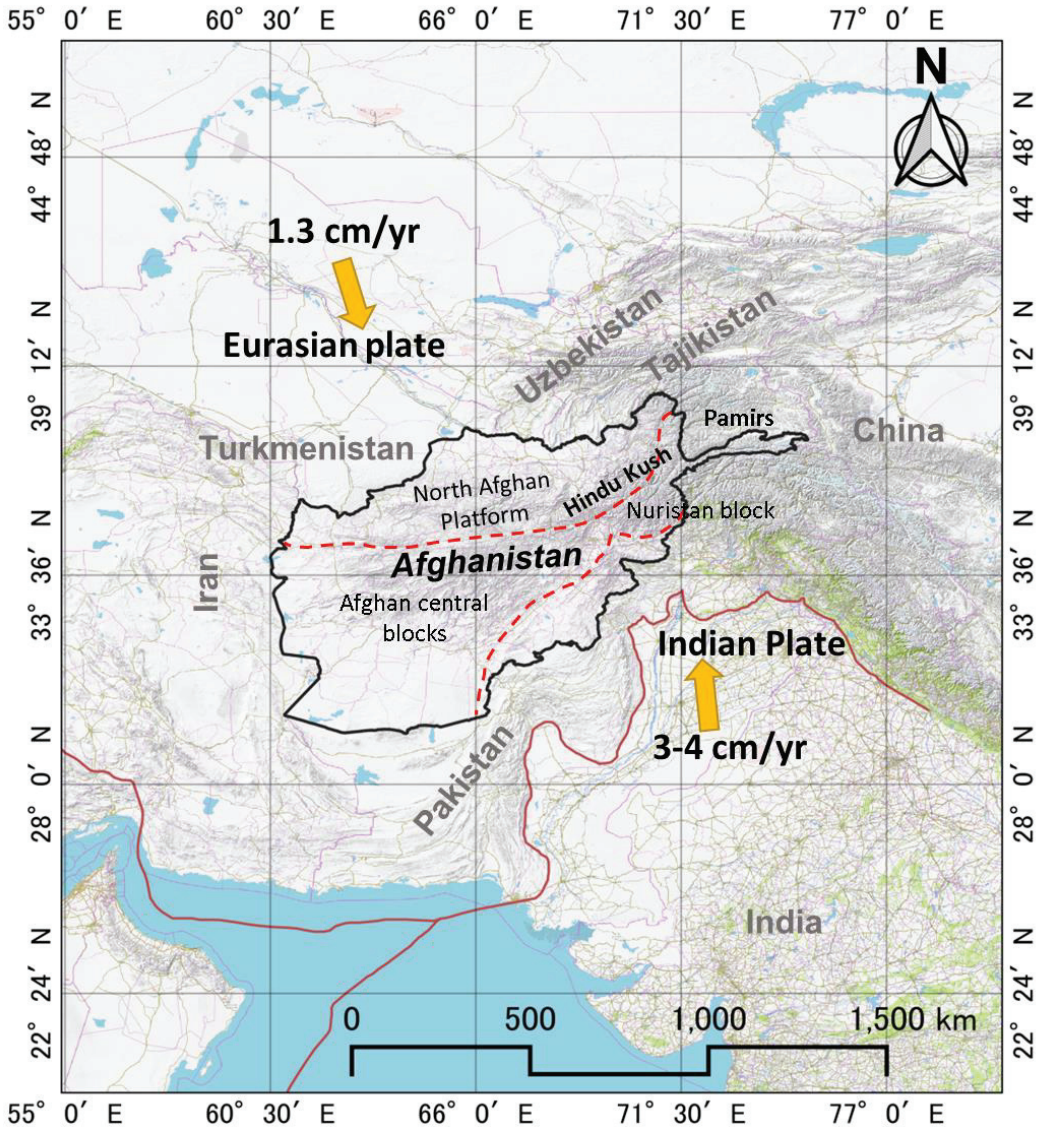

Figure 2-6. Presents the geotectonic plates inside and beyond Afghanistan's border, which as a result may cause major earthquake in Afghanistan and surrounding countries.

If a modern deformation continues in the so-called region, moderate- to- large magnitude are occurring. As a result, the earthquake will cause massive damage, not just from ground shaking and ground surface fault rupture, but also triggering liquefaction and extensive landslide as occurred in Kashmir (Harp et al. 2006). Among all active faults in Afghanistan Hindu Kush-Pamir region the most active because it is intersected by network of faults that have different orientation and direction of movement. Fig 2-7.

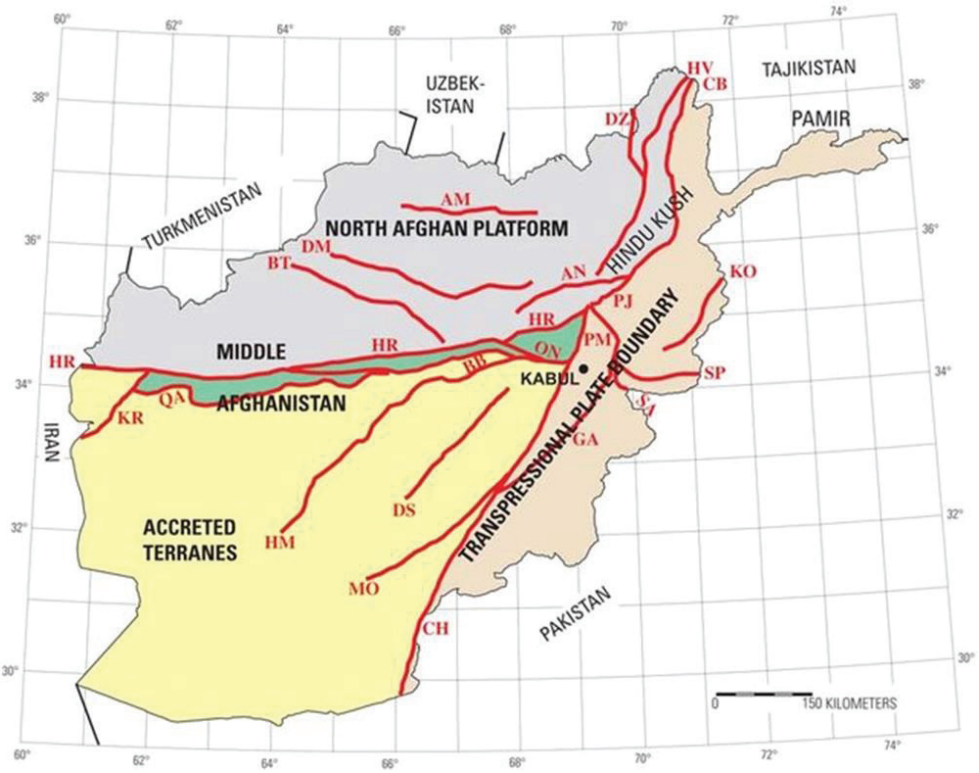

Figure 2-7. Presents the active faults inside Afghanistan (USGS) Modified from Wheeler et al. (2005).

Large number of earthquakes in Afghanistan is triggered by Indian plates which is moving northward beneath Eurasian plate at speed of 3-4 cm/year (Fig. 2-6). This collision make the Himalayan, Hindu Kush, and Pamir Mountains uplifted. As a result of this activity majority of the historical earthquakes happing northern parts of the country. Figure 2-8 clearly illustrates that the distribution of historical earthquakes mostly occurred in Hindu Kush-Pamir

region and gives and insight that future earthquake most likely to happen more and more because those areas under large stresses that cause slip on faults.

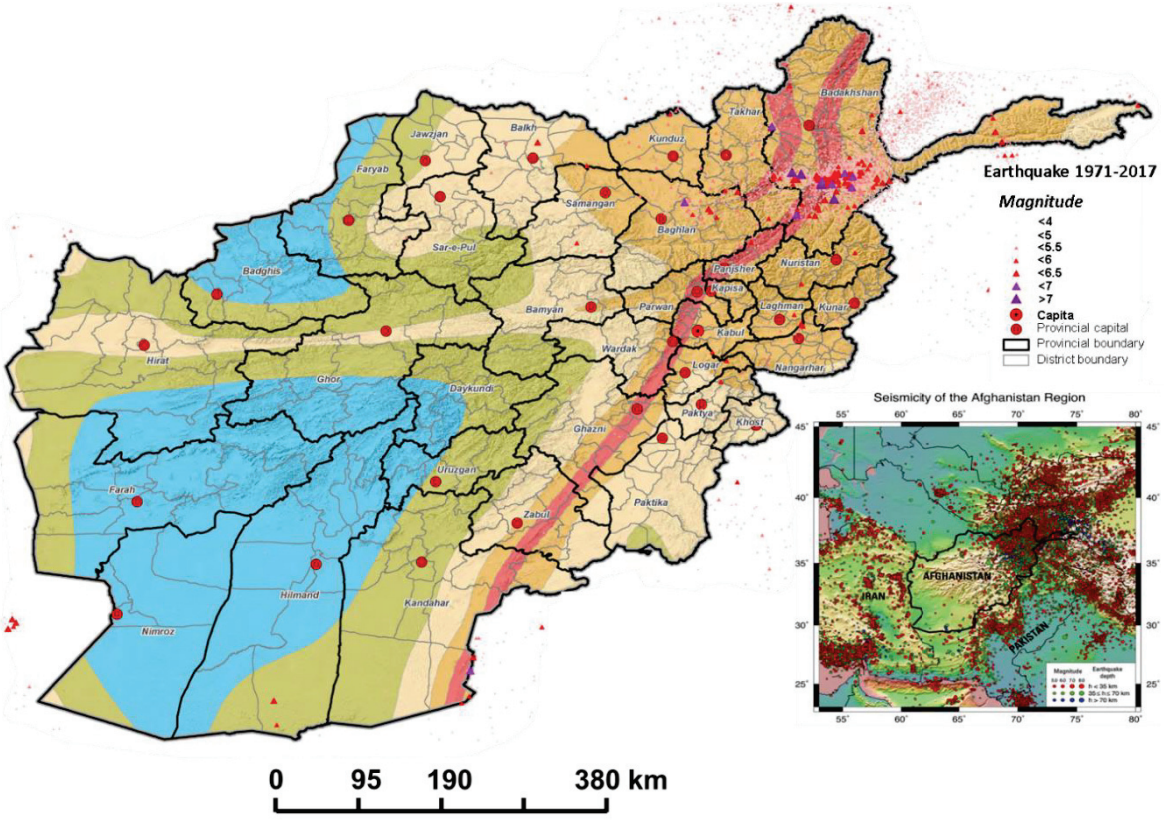

Figure 2-8. This map indicates all the earthquakes recorded in the period between 1971 until first Oct. 2017(IMMAP - E. Hagen, 2017).

Table 2-1. Shows the recorded number of earthquakes, magnitude in Afghanistan from 1971 to 2017 (U.S Geological Survey earthquake program, 2017).

	Number of Earthquakes (magnitude)				
Period	**3-4.9**	**5-5.9**	**6-6.9**	**7-7.9**	**Total**
1971-1979	763	144	17	1	925
1980-1989	1258	140	14	2	1,414
1990-1999	2,181	178	26	3	2,388
2000-2009	3,800	176	21	1	3,998
2010-2017	1,750	122	5	3	1,880
Total	9,752	760	83	10	10,605

Historically many earthquakes struck Afghanistan with magnitude larger than 6 as shown in Table 2-1 which caused huge injuries, loss of life and damages to the properties.

Figure 2-9 presents the earthquakes' magnitude and depth between 2015 to 2022. In 2015 an earthquake which is recorded in USGS with magnitude 7.5 Mw (Fig 2-9) caused nearly loss of 400 people, more than 2500 injuries, and more than 36000 houses were damage, and 7000 houses were totally destroyed. (IFRC, 2015). The shake impact was felt beyond Afghanistan's border as damages and casualties have been reported in the western part of Pakistan while minor damage occurred in India. (OCHA, 2015).

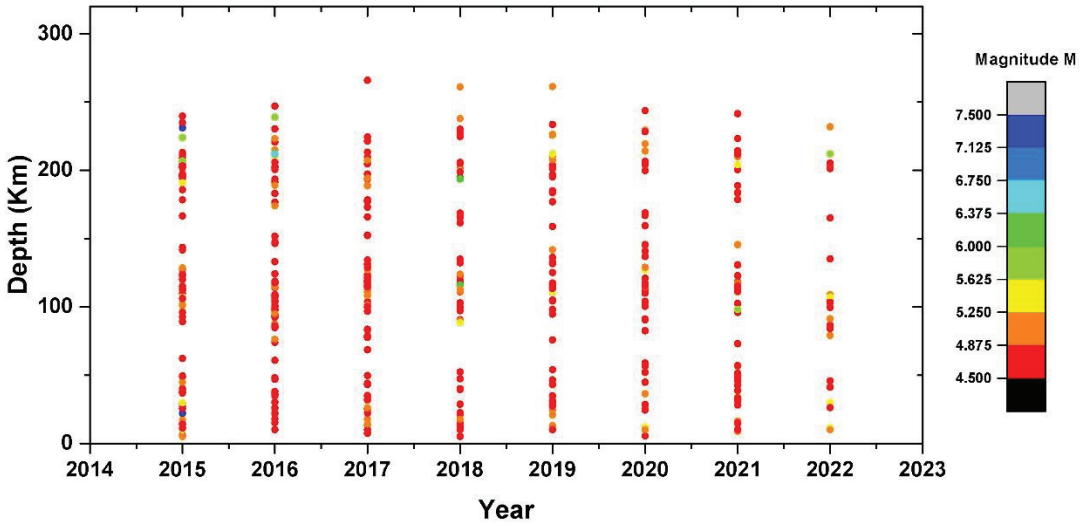

Figure 2-9. Illustrates the recorded magnitudes and depth of the earthquake from 2015 to 2022 (USGS, 2022).

2.3.1 Earthquake Risk and its impact on assets in Afghanistan

Afghanistan is struck by moderate to strong earthquakes, causing huge damage and loss of life. Based on report (World Bank, 2017) earthquake has been caused the greatest numbers of deaths since 1900. As discussed north and north-eastern parts of the country is under high risk of earthquake hazards. Particularly most of the earthquake record was observed along the borders with Tajikistan, Uzbekistan, and Pakistan. Based on reports (World Bank, 2017) 10,000 people were killed since 1990 as a result of earthquake. As shown in Fig. 2-10 Kabul, capital of Afghanistan is under high risk due to its location in earthquake prone area and the concentration of assets. So far Kabul has the highest average estimated damage compared to all regions in Afghanistan. (World Bank, 2017). Figure 2-10 presents the people and GDP exposure to the earthquakes.

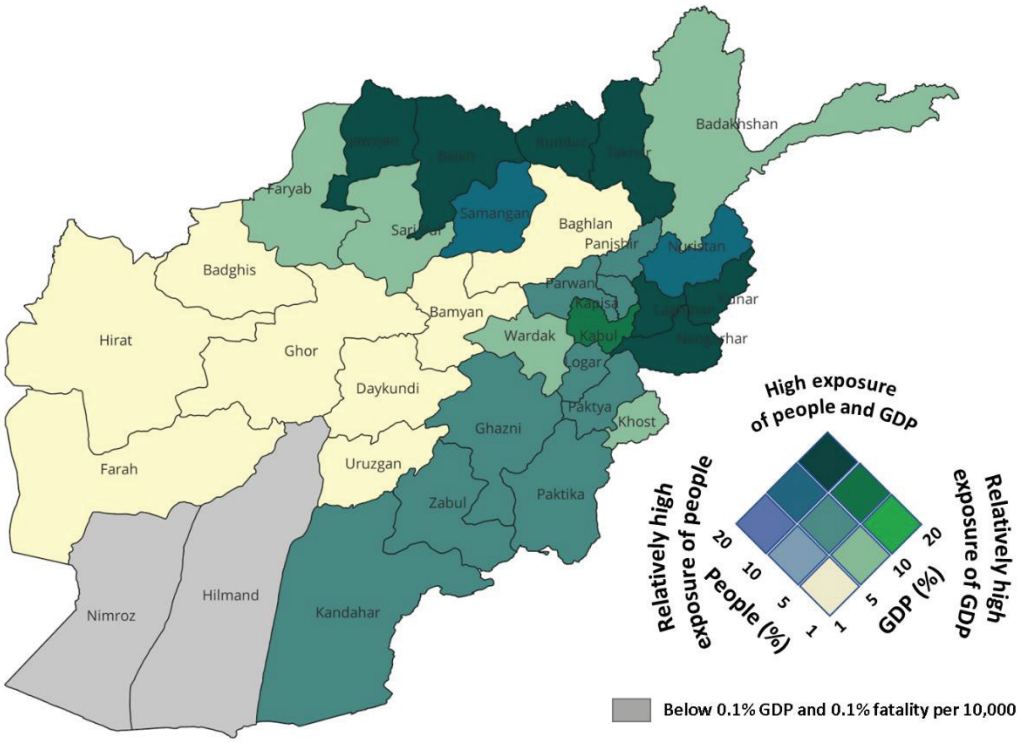

Figure 2-10. Population and GDP exposure to earthquake in Afghanistan. (World Bank, 2017)

Based on a study conducted by (World Bank, 2017) an earthquake with high magnitude in Kabul highly likely cause approximately more than 8000 deaths and over $500 million in damages, due to high concentration of population and GDP.

The exposure assessment of essential assets is presented in Fig 2-11, it shows the location where each asset intersects with these hazards, and the vulnerability of those assets. This map is produced based on historical records of earthquakes which on the other hand illustrates the location of earthquake hazard prone areas. The information created from the assessment are important and useful for policy makers as basis for plans and interventions on preparedness, early warning, response recovery, and mitigation. In Afghanistan earthquakes, primarily affecting people, private buildings, roads, healthcare facilities, education related buildings and facilities, and energy related facilities as shown in (Fig. 2-11). The impacts of earthquake on each asset are different, it is mostly depending on the characteristics of the assets. Moreover, from Fig. 2-11 it clearly can be noticed that the cities which is susceptible to the earthquake and having high concentration of any assets having more exposure to the earthquake.

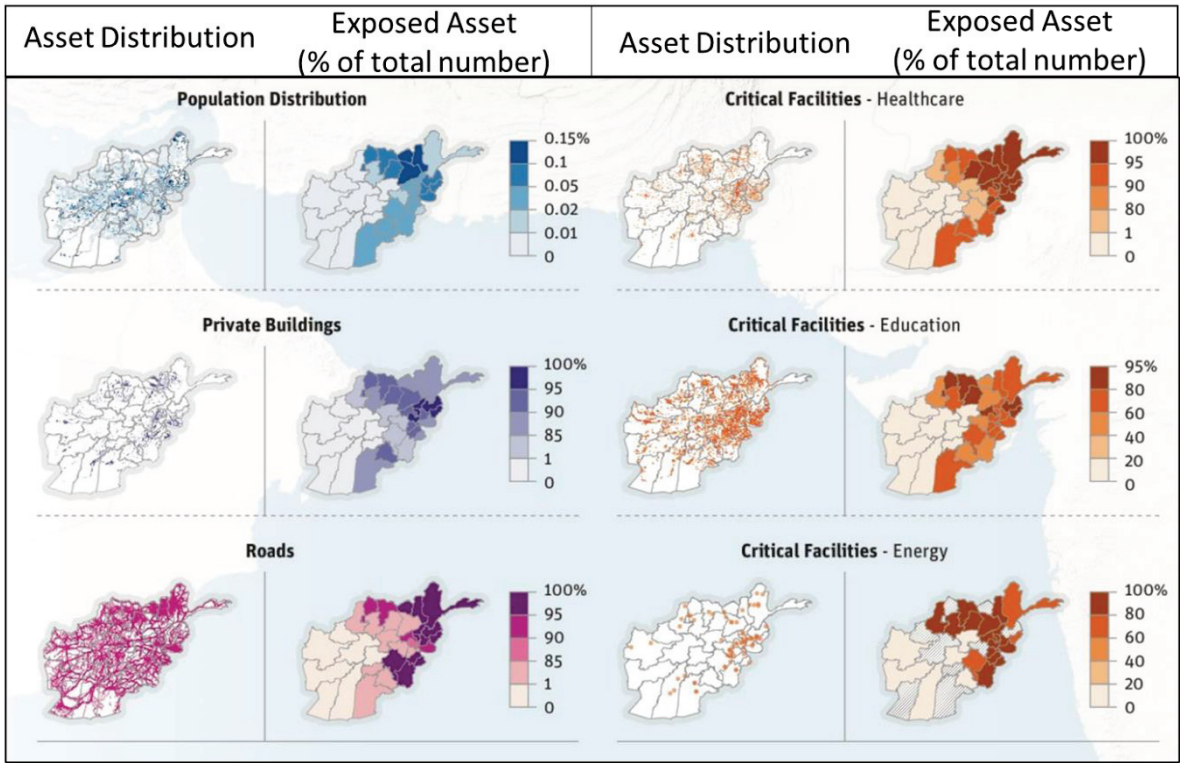

Figure 2-11. Presents the distribution of assets and its exposure to the Earthquake across all Afghanistan. (World bank, 2017).

As can be seen in Fig 2-11, north and north-eastern parts of the country's assets are under high exposure. Particularly, Kabul province with highest population density has the highest exposure of the population to the earthquakes. The percentage of population exposed to earthquake ranges from 0 to 0.15 percent. Likewise, private buildings, roads healthcare and education related buildings are found to be exposed to earthquake and percentage of exposure is shown in Figure 2-11.

2.3.2. Recommendations

As mentioned north and north-eastern part of Afghanistan suffers from one of the highest earthquake rates in Afghanistan. The proximity of the boundary between the Indian and Eurasian tectonic plates means that there is a lot of seismic activity going on almost constantly. Most of these earthquakes go unnoticed, but every now and then a larger scale quake hits the area and the impacts of it can be felt for a long time afterwards. Constructing new structures based on updated seismic design code, retrofitting existing building can reduce the building collapse and fatalities from earthquake significantly. Moreover, lack of consciousness also play an important role in high rate of fatalities due to earthquake. Therefore, learning some basic earthquake safety tips can help reduce the death tolls considerably.

2.4. Landslide

Due the mountainous terrain, unstable soil, heavy rainfall, frequent earthquakes more than 60 % of land in Afghanistan, from the northeast to the western region are susceptible to landslides. Lack of landslide hazard maps and lack of consciousness of the people make them to build their houses in susceptible places which leads loss of life and properties. In Fig 2-12 exposure of two categories of assets are illustrated. The intersection of hazard and exposed datasets has been carried out by using landslide susceptibility maps produced at the national level (Afghanistan-MHRA, 2017). As can be seen in Fig 2-12 in province such as Badakhshan, Nuristan, Daikundi, and Ghor large number of people exposed to landslide. Similarly, in Badakhshan, Takhar, and Ghor province large numbers of assets values under exposure of landslides. Based on reports (World Bank, 2017) deforestation, land-use change and increase in heavy rainfall increase the severity of the landslide hazard to the houses and settlements.

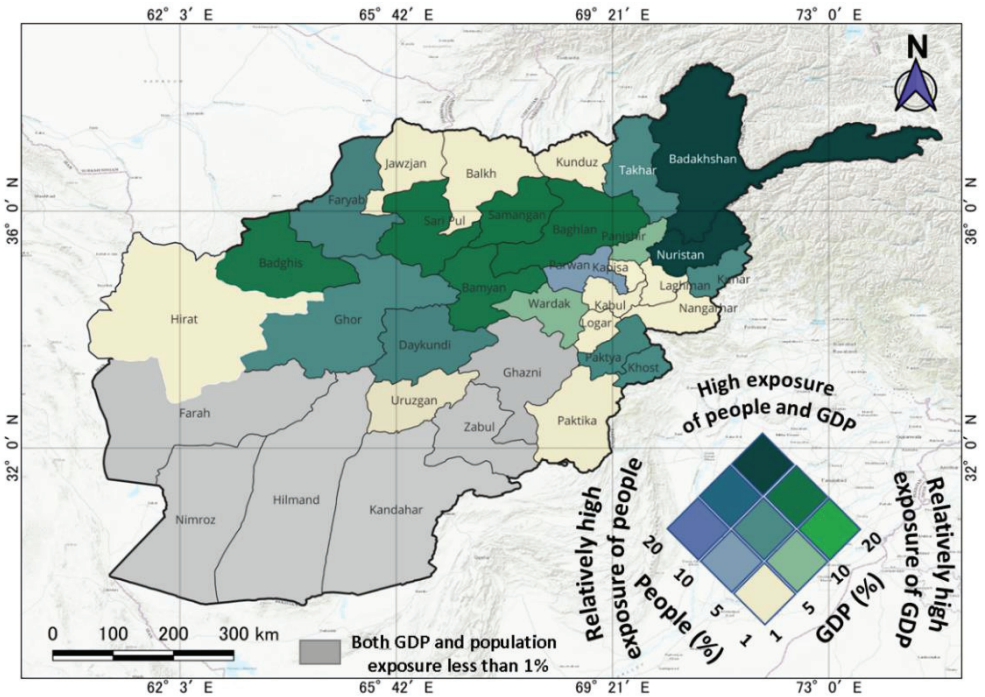

Figure 2-12. Population and GDP exposure to landslide in Afghanistan. (World bank, 2017).

2.4.1 Landslide Risk and its impact on assets in Afghanistan

This study evaluates the significance and socioeconomic value of assets (people, infrastructures, schools, health facilities, highways, etc.) in relation to their exposure level. Such an approach provides a comprehensive overview of the general exposure at the national level. The available exposure data layer for each category (population, government buildings, commercial and residential buildings, agricultural, infrastructure, and GDP) are shown in Fig. 2-13.

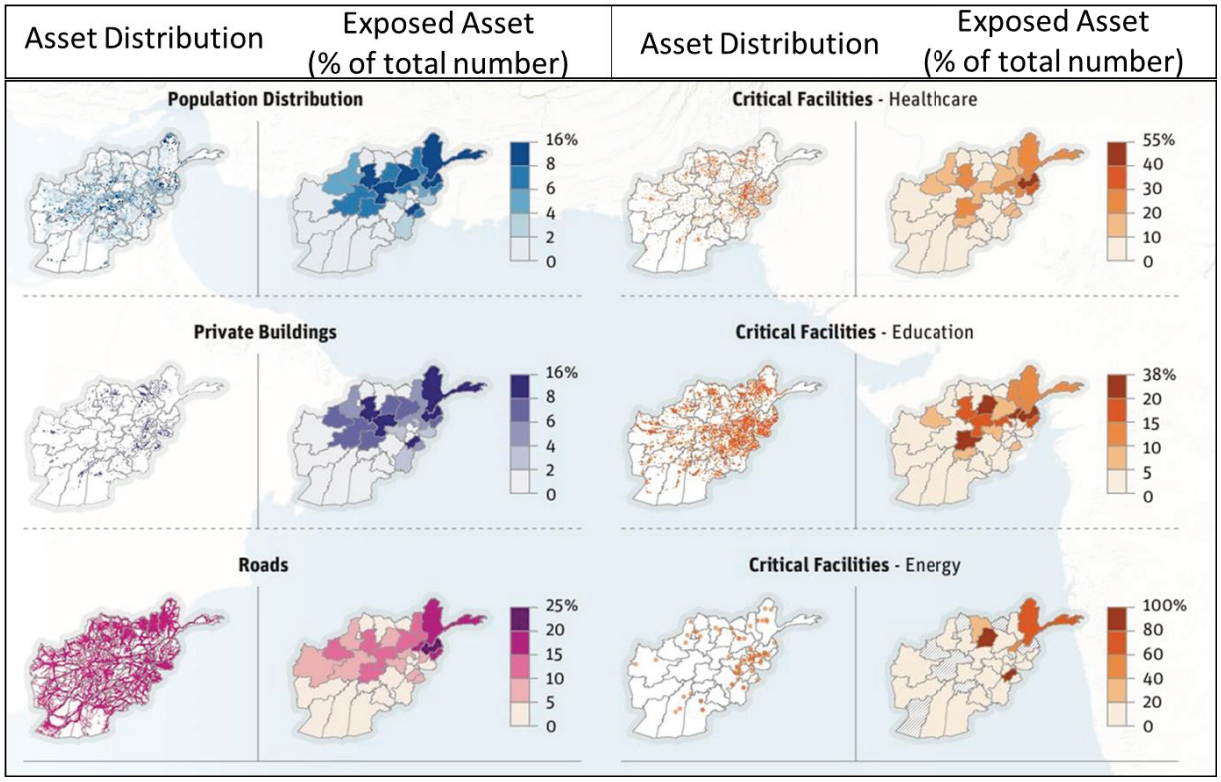

Figure 2-13. Presents the distribution of assets and its exposure to the landslides across all Afghanistan. (World bank, 2017)

As can be seen in Fig 2-13 highest number of assets exposed to landslide are located in north, north-eastern, and central parts of the country. Based on findings of (World Bank, 2017) over 3 million people area exposed to landslides in Afghanistan. Badakhshan has more than 800 million dollars' worth of assets and more than 280,000 people exposed to landslide. an

example of a devastative landslide in Afghanistan would be Abe-Barek landslide which caused death hundreds to thousands of people.

2.4.2. Recommendations

It is stressed that landslide is a common natural disaster causing deaths and economic losses each year. The risk of landslide can be reduced by increasing consciousness of the people in the national and local level avoid building their houses landslide prone areas. Moreover, government also prepare the landslide hazard maps in local level to better understand the risk in each area. Furter, it is government job to recognize the landslide susceptible area and avoid the construction of transport networks or service lines and other important infrastructure. In most of the landslide prone countries local monitoring of slopes is very effective and it can help identify the landslide hazard early. It is also noteworthy that if a landslide susceptible area identified then strengthening of the slope would reduce the potential risk of landslide to some extent. Passive measures such as gathering of boulders in the foot of hillside, geosynthetic and geotextile can also reduce the impact of small landslide from reaching to the assets.

2.5. Snow Avalanches

Avalanches are a common natural disaster found in most mountain snowy regions of the world. Avalanches are rapid mass movement of snow caused by gravity and are considered meteorologically induced dangers. There are various types of avalanches such as wet type, dry type. All avalanches from starting point to the stopping point has three stages: origin, transition, and runout. Typically avalanches occur in steep terrain of 30° to 45° having large accumulation of snow (Fuchs et al., 2019). On terrain below 15°, the avalanche slows down and stops. The flow velocity of avalanches is ranges between 50-200 km/h, whereas wet avalanches are denser and slower (20-100 km/h). (Fuchs et al., 2019) Avalanches can trigger naturally or artificially. Whereas spontaneous natural avalanches pose a major threat to buildings and infrastructure.

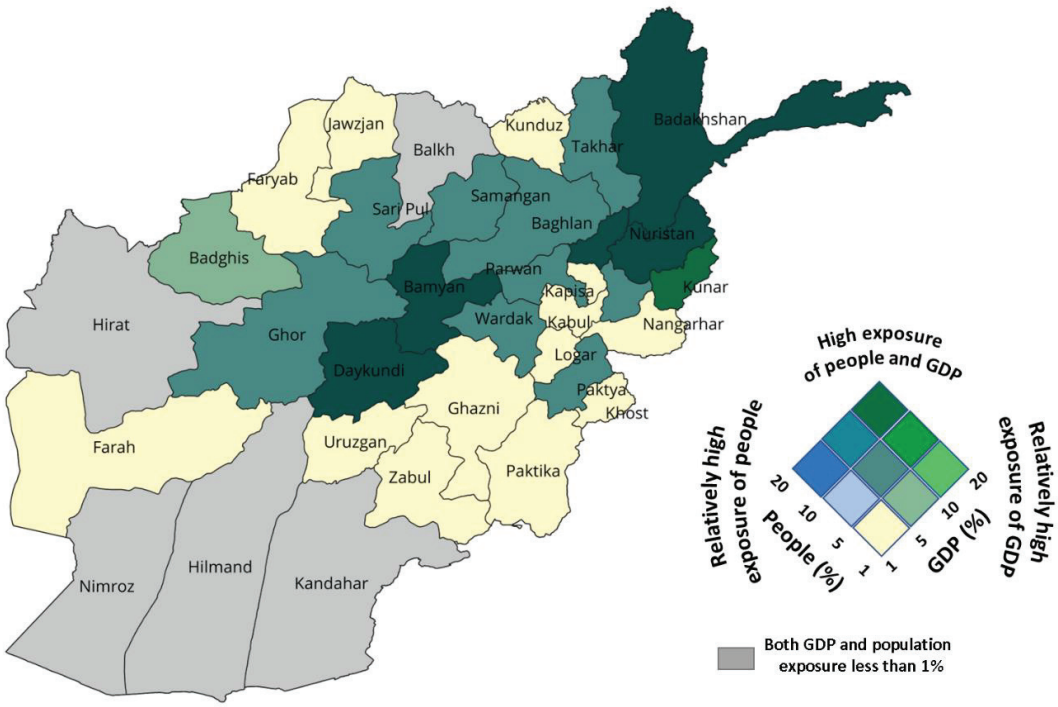

Figure 2-14. Population and GDP exposure to snow avalanches in Afghanistan (World bank, 2017).

Figure 2-14. presents the avalanche prone province in Afghanistan. As can be seen from Fig. 2-14 the majority of north-eastern to western, and central parts of the country are very susceptible to avalanches due to the availability of snow in most of the seasons in high mountains Hindu Kush.

Snow avalanches affecting the people living in those hazardous areas. Avalanche deaths continue to increase in Afghanistan. The latest avalanche in 2022 in Afghanistan killed at least eight people, including three children, have been killed and 10 others wounded in three separate incidents of landslide and avalanche in Afghanistan (Xinhua, 2022). The worst avalanche was occurred in Salang Pass (Fig 2-15) on Feb 2010 which is the only road connecting Kabul to the northern provinces and more than 180 people have been killed there which was the worst avalanche in a past 30 years. (World bulletin, 2010).

Figure 2-15. Long line of traffic jam including different vehicles are half-buried in snow after avalanches killed at least 180 people at the Salang tunnel in Parwan province, Afghanistan on February 10, 2010. (Photo: Shah Marai)

Accessing and providing assistance to in emergency time to such remote places is the biggest challenge with the avalanche's events particularly in unstable country like Afghanistan. As illustrated in Fig 2-14 Badakhshan, Kabul, and Daikundi have the greatest number of people and GDP affected by avalanches.

2.5.1 Snow avalanches' risk and its impact on assets in Afghanistan

In order to illustrate the population, infrastructures, schools, health facilities, roads, etc. level of exposure to the avalanches, this study consider their relevance and socioeconomic value accordingly. Such an approach very helpful for overviewing of the general exposure at the national level. The available exposure data layer for each sector (population, government buildings, commercial and residential buildings, agricultural, infrastructure, and GDP) is shown in Fig. 2-16.

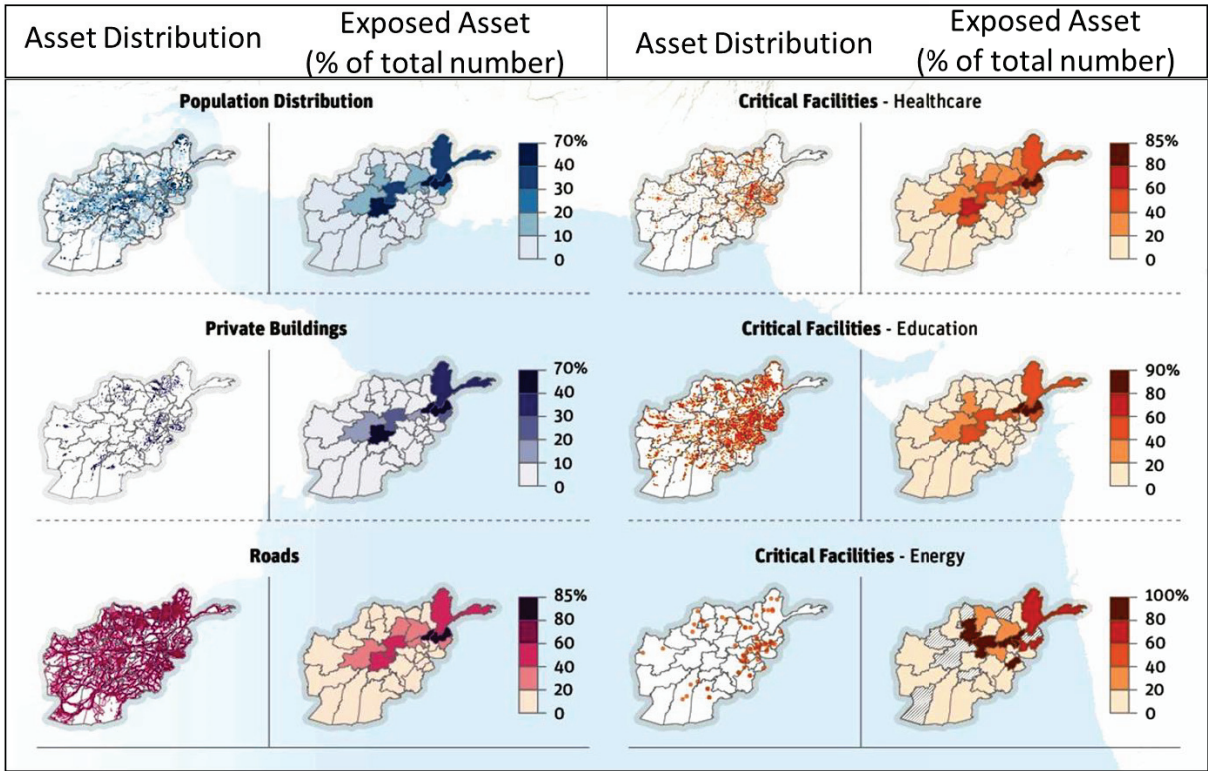

Figure 2-16. Presents the distribution of assets and its exposure to the avalanches across all Afghanistan. (World Bank, 2017).

As can be seen in Fig 2-16 highest number of assets exposed to landslide are located in north, north-eastern, and central parts of the country. Based on findings of (World Bank, 2017) over 2 million people area exposed to landslides in Afghanistan. Badakhshan has more than 990 million dollars' worth of assets. From 2000 to 2015, over 153,000 people were affected by avalanches in Afghanistan (World Bank, 2017).

2.5.2. Recommendations

As discussed in this section avalanches are a common natural disaster causing deaths and economic losses each year in Afghanistan. The risk of snow avalanches similar to other natural disasters can be reduced by increasing consciousness of the people in the national and local level avoid building their houses in landslide prone areas. Building retention structures such as snow supporting structures, artificial release of avalanches in susceptible areas, building dam avalanches, and avalanches galleries can reduce the avalanches risk of exposure to different assets.

2.6. Droughts

Afghanistan has arid and semi-arid climate condition suffers from recurring droughts with varying lengths and severity. Agriculture in Afghanistan contributes to 80 % of Afghanistan's total income. Frequent occurrence of droughts in Afghanistan affects millions of people and causing large economic damages to agriculture, households, and other lifeline structures. Its annual water budget relies heavily on winter rainfall in its mountains, which accumulate in the form of glaciers, snow, and ice. The amount of water available depends on the amount of rainfall and stable weather patterns, which causes snow and ice to melt continuously during the planting season. The Hindu Kush Mountains in Afghanistan are the source of 80% of the country's renewable water. Afghanistan experienced severe drought in the past (e.g., 1970, 1996 and 2001), but in the southern provinces of Kandahar, Helmand, Zabul, Uruzgan and Nimroz, it was so severe that in 2000, the United Nations estimated that nearly three million people needed emergency assistance (OCHA, 2001).

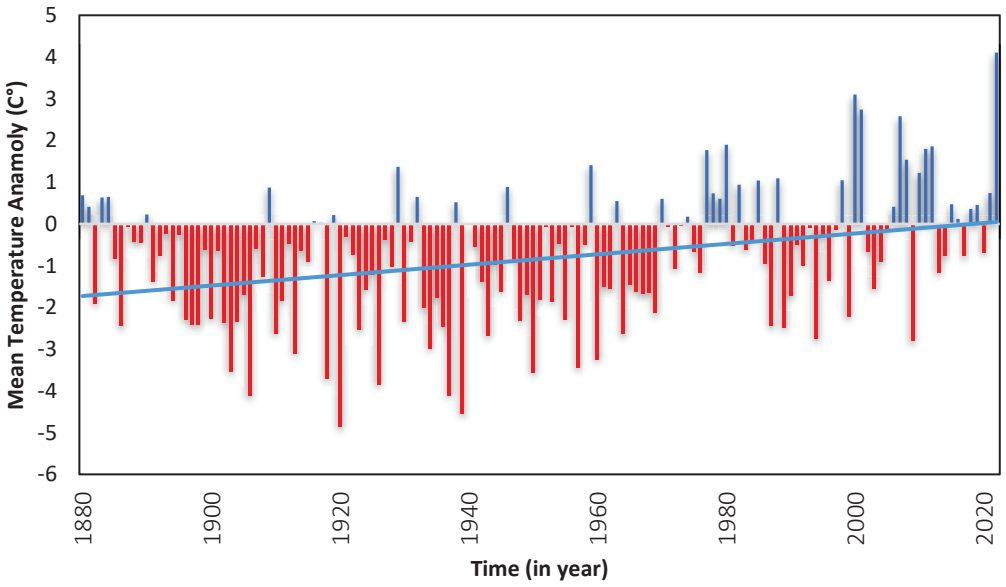

Figure 2-17. Time series of annual values of Afghanistan mean temperature anomalies and its trends (Base period 1981-2010) (NOAA data).

Figure 2-17 presets the Time series of annual values of Afghanistan mean temperature anomalies and its trends from 1880 to 2022. A positive anomaly means that the temperature was warmer than normal; a negative anomaly indicates that the temperature was cooler than normal. As can be seen the year recorded as warmer temperature or low negative winter often corresponds to the driest year or drought.

Droughts causes further threat to livelihoods, income, poverty of the people which 80 % of their livelihood rely on agricultural. Lack of water resources led to excessive reduction of wheat yields and drying of fruit trees, plants, grasses, and the loss of 50 to 60 percent of livestock in those provinces. The drought caused so much famine that the United Nations named the worst-hit areas, from northwestern Afghanistan to the central Hazaras, the "Hunger Belt."

Afghanistan's drought cycle lasts from three to five years once a decade (Arthur et al, 1966). In the last two decades, Afghanistan has experienced drought twice a decade, in the 2000s in 1996-2001 and 2007-2009, in 2010 in 2011-2013 and 2016.

Afghanistan is expected to be affected by climate change and uncertain rainfall and frequent droughts, and the increased risk of flooding would come in secondary concern. Annual drought in many parts of the country is likely to become common by 2030. As can be seen in Fig.2-18 population and assets in southern provinces are under high exposure and threat of droughts

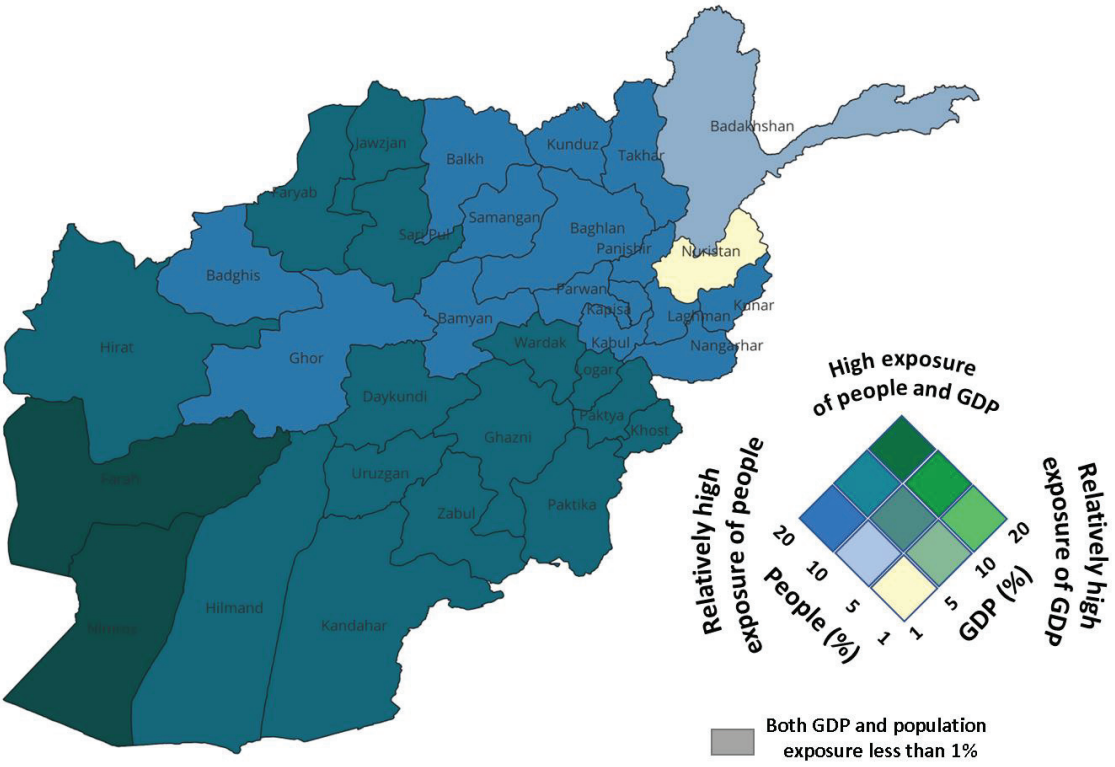

Figure 2-18. Population and GDP exposure to Droughts in Afghanistan. (World Bank, 2017).

Based on reports (World Bank, 2017) on average, droughts cause 280 million of economic loss to agriculture each year. Due to the climate change consequences, the hydropower production will decrease to zero once in every 10 years in Kajaki Hydropower, and once in Naghlu Hydropower (World Bank, 2017).

2.6.1 Drought risk and its impact on assets in Afghanistan

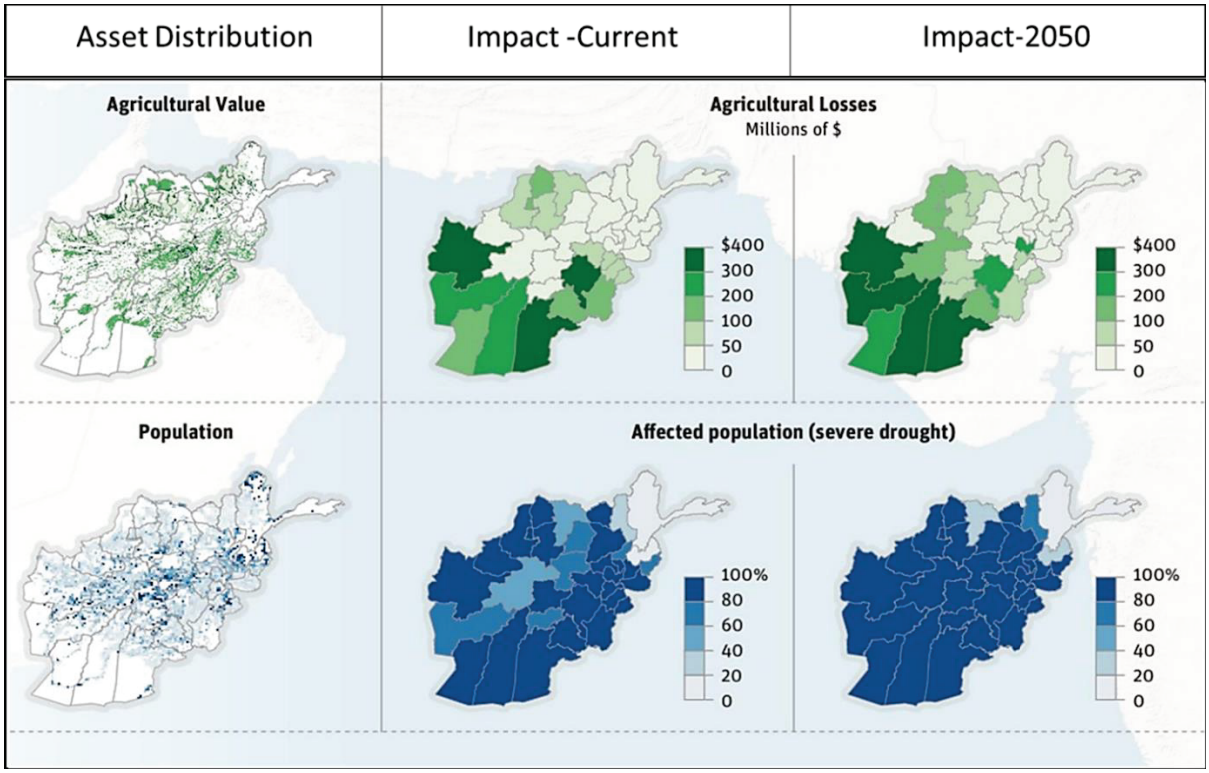

Figure 2-19. Presents the distribution of assets (e.g., agriculture, and population) and the current and future impacts of snow avalanches on them in different part of Afghanistan. (World Bank, 2017).

Drought has a direct impact on crops and thus on people. Therefore, the impact of current and future droughts on agriculture and people will be introduced. Assessing drought and its potential impact on agriculture in vulnerable areas is very important, especially in drought-prone areas. Quantifying the impact of agricultural drought on food supply may enable policy makers to make more sustainable agricultural decisions. This requires a thorough assessment of the relationship between spatiotemporal drought variability, agricultural systems, irrigation effects and the availability of water resources. To illustrate the population, and agricultural impacts, level of exposure to the droughts, this study consider their relevance and socioeconomic value accordingly. Such an approach very helpful for overviewing of the general exposure at the national level. The current and future impacts of droughts in Afghanistan are shown in Fig. 2-19. The effects of drought on agriculture and population

modeled by FAO for Afghanistan are shown in Figure 2-19, which shows that approximately 90% of Afghanistan will be affected by drought by 2050.

2.6.2. Recommendations

There is an urgent need to enhance public awareness to improve the possibility of wastewater sampling and decrease water use in light of the anticipated precipitation over the next few months. Additionally, farmers should shift to crops that produce greater yields per unit of water applied to irrigable land. This will maintain the water balance and minimize drought danger to some degree. Beyond these short-term remedies, the government must prioritize a comprehensive drought risk management plan. By enhancing the agricultural system's resilience, sustainable development can reduce vulnerabilities to climate change. In addition, applying a successful model of a nation that has experienced drought along with best management techniques on farms and in agriculture might reduce the danger of drought to some extent. Implementing a low water consumption restriction policy during the high-water season and conserving that quantity of water in particular areas, such as the southern provinces, might also be an effective method for promoting sustainable living.

CHAPTER III

Assessment of the Abe-Barek Landslide using Remote Sensing Analysis

3.1. Introduction

A devastating landslide hit Abe Barek village of Argo District, Badakhshan Province, Afghanistan (Fig 3-1) in May 2014. It was the worst landslide in 2014, killing 300 to more than 2700 people (Zhang et al., 2015). According to the locals, two landslides occurred within a short period of time. The villagers may lack the specialized knowledge, training, and necessary equipment to perform triage and started the search and rescue operations for assistance to the first trapped victims shortly after the first incident (New York Times, 2014). Tragically, many volunteer rescuers become secondary victims themselves (The Guardian, 2014). Considering the remoteness of the landslide area, rough road conditions, insufficient capacity for fast and well-timed transfer of machinery, and the necessary equipment, the government quickly concluded that retrieving the buried bodies is unattainable. Hence, the site was declared a mass grave (CNN, 2014). Figure 3-2a, taken by (Kohsar, 2014), and outlined with a yellow color, shows the landslide's downward movement direction in a sufficiently inclined surface rupture over a considerable distance and buried the settlements along its pathway. Moreover, Figure 3-2a, b clearly illustrates previous landslides' boundaries in the same position with red lines.

The study area with a latitude of 37°1′ 18″ N and a longitude of 70°22′01″ E is situated 21 km away from Faizabad, the capital of Badakhshan province. Badakhshan is one of the 34 provinces of Afghanistan, located in the northeastern part of the country along the Pamir and Hindu Kush Mountains. Some of its mountains lay between 3000–7000 m above sea level and are covered with snow and glaciers throughout the year. Badakhshan is one of the most remote,

least developed, and disaster-prone regions, which borders Tajikistan to the north, Pakistan to the south, and China to the easternmost (Figure 3-1a).

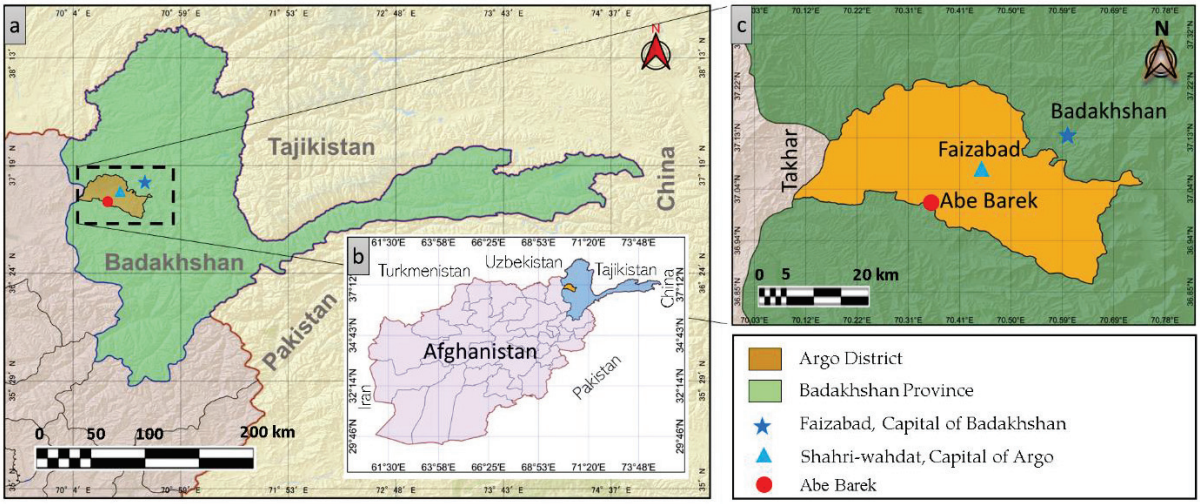

Figure 3-1. Location of the study area. (a) Afghanistan, study area, and borders with neighboring countries, (b) Badakhshan province, (c) Argo district, and Abe Barek village.

The presence of two active plate boundaries (Shroder, 2014), namely "North Afghan Platform and Transgressional Plate boundary", and the passing of three major active faults through the province (Boyed et al., 2007), namely the Central Badakhshan Fault, Darvaz Fault, and Henjvan Fault, making it the highest seismic prone region in the country and is arguably one the most vulnerable regions to all kinds of natural disasters. With this regard, most of the researchers relate the majority of the landslide hazards to earthquakes. Argo district (Figure 3-1c), of which Abe Barek is one of its villages, with 10% of the whole province population, is the most populous district in Badakhshan (UNFPA, 2003). According to the previous study (Zhang et al., 2015), 30.2% of the entire land in Badakhshan province is covered by a slope gradient of 20–30°, and in the area where the landslide occurred, 78% of its land is made up of a slope gradient of 20 to 40°. This might be considered as one of the reasons why this area is prone to landslides.

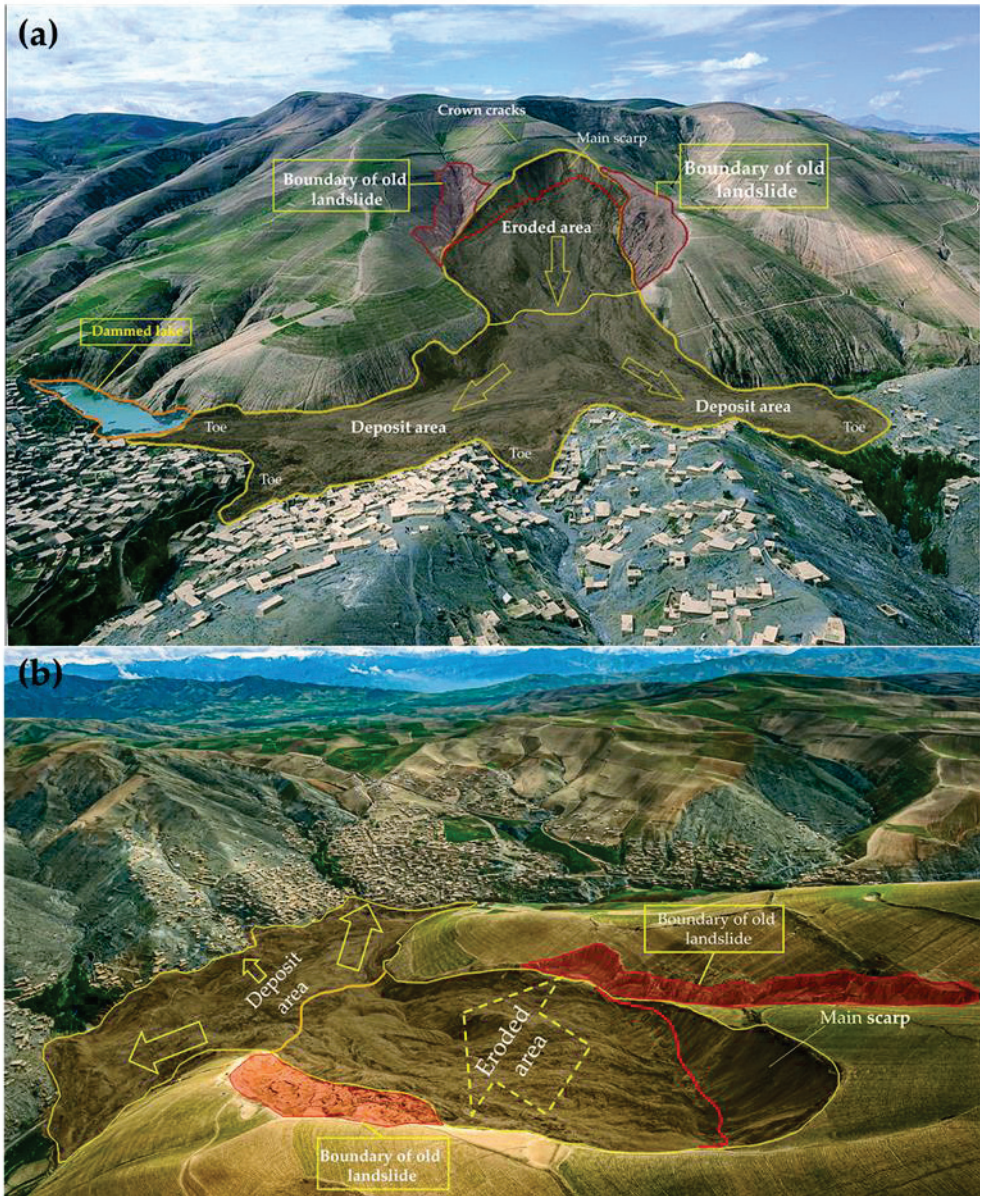

Figure 3-2. Collapsed area. (a) Front view of the Abe Barek landslide area, the yellow outlines indicate the boundary line on the current landslide, the red outlines represent the boundary of old landslides, and the photograph was taken on May 5, 2014, by (Kohsar, 2014). (b) Top bird view of the landslide area shows how steep the slope is, the red outlines reflect the boundaries of the old landslides, the photograph was taken on May 5, 2014, by (Kohsar, 2014).

The Abe Barek landslide area brutally buried houses and killed large numbers of people, which can be categorized as the most life-threatening (Zhang et al., 2015) natural disasters after two incidents of the 1998 earthquakes (Boyed et al., 2007; Wheeler et al., 2005) occurred in this area. To date, (Shroder et al., 2011a; Shroder et al., 2011b) has determined 34 large loess landslides that are commonly triggered by saturation and liquefaction in this area. Knowing the cause of the landslides is extremely important. However, as mentioned, not so many studies have been conducted in the area of interest to figure out the main reason. The only research conducted in the study area is the susceptibility assessment in the Abe Barek (Zhang et al., 2015). Landslide factors such as topography, climate (rain), geology and seismicity of the area, land cover and land use, and previous earthquakes were reviewed deeply. Eventually, they identified the following factors as a leading cause of the incident:

- Weakening of the rock-based silt-covered area due to the repeated seismic events.
- Slope instability further intensifies due to the remaining too loose materials from the previous landslides at the same position.
- Slope instability due to the increased infiltration of rainwater into the loose soil.
- The presence of sensitive material which is very prone to landslides.
- Increasing the soil water content from the rapid melting of deep snow and spring rains up to 200 mm.
- Land use and irrigation activities.

Finally, it can be concluded that the cause of the landslide is not one. Rather, a set of triggering factors (e.g., complex geology, the presence of landslide-prone material (Shroder et al., 2011a; Shroder et al., 2011b), previous earthquake records, and close distance to the fault line's intersection (Wheeler et al., 2005), summer rains, and melting snow) or a combination of any of such mentioned factors possibly lead to this unfortunate situation.

Even though this tragic event caused loss of hundreds of people and buried hundreds of houses, yet there was no research conducted to illustrate the size (area and volume of landslide) and number of affected houses.

3.2. Satellite imagery used in landslide analysis

In this study, stereo pair high-resolution satellite images were gathered to generate pre- and post-event DEMs. The pan-sharpened GeoEye-1 images with the spatial resolution of 0.5 m observed in June 2012 were analyzed to create the pre-event DEM. The pan-chromatic IKONOS-2 images with the spatial resolution of 0.8 m observed 2 months after the event in 2014 were analyzed to create the post-event DEM. Table 3-1 shows the characteristics of the satellite images used in this study and their observation conditions. Since the pre-event images were observed on the same day with different off-nadir angles, the pair images' quality can be judged as very good. On the other hand, since the time interval of the observations of the post-event images is 8 days, and land cover changes were slightly observed between the images, the pair quality of the post-event images are judged as good.

Table 3-1. Distinguished features of the satellite imagery used in this study and their observation conditions.

	Pre-Event		**Post-Event**	
Image ID	105041000005F800	10504100000CBE100	106001000932AC00	1060010009356D00
Date	13 June 2012	13 June 2012	7 July 2014	15 July 2014
Satellite	GeoEye-1	GeoEye-1	IKONOS-2	IKONOS-2
Band	Pan-sharpened	Pan-sharpened	Panchromatic	Panchromatic
Spatial resolution (m)	0.5	0.5	0.8	0.8
Off-nadir (deg.)	18.4	29.6	24.1	9.6
Satellite azimuth (deg.)	N63.1E	N36.8E	N220.1E	N169.4E
Sun elevation (deg.)	68.7	68.6	70.0	67.8
Sun azimuth (deg.)	N124.2E	N124.0E	N132.4E	N129.0E
Cloud cover (%)	1.0	5.0	3.0	0.1
Overlapped area (km^2)	24.5		30.5	
Pair quality	Very good		Good	

Figure 3-3 shows the flowchart for the DEM generations from the acquired satellite im-ages. The DEMs and orthorectified images were generated by a dense stereo matching technique using commercial software (Agisoft Metashape Professional Ver. 1.6.3). The technique consists of a photo-alignment, generation of the three-dimensional dense point cloud, and building of the mesh.

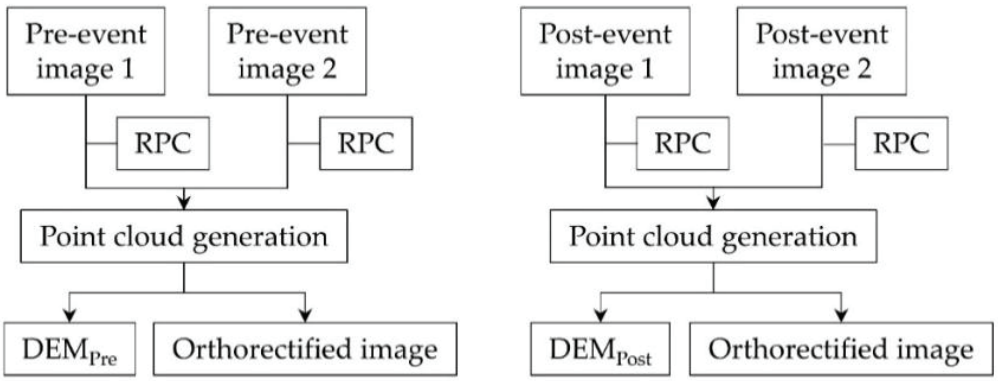

Figure 3-3. Flowchart for the data acquisition and digital elevation model (DEM) generations.

Approximately 168 thousand tie points and 34 mil-lion-point clouds were extracted in the pair of the pre-event images, indicating that the mean cloud density is 1.4 points per square meter. On the other hand, approximately five thousand tie points and 16 million-point clouds were extracted in the pair of the post-event images, demonstrating that the mean cloud density is 0.5 points per square meter. The images' geographic locations were coordinated using rational polynomial co-efficient (RPC) files. The RPC files were provided by the supplier as a standard positioning assistance dataset, including polynomial equations to relate geographic locations (latitude, longitude, and height) with locations in the image (row and column).

Figure 3-4a, and b illustrate the pre- and post-event DEMs created from the images, respectively, and Figure 3-4 c, d shows the hillshades effects on the DEMs. Unexpected small concavities and convexities were found in the post-event DEMs (Figure 3-4d), probably due to the lower density of the point clouds. Figure 3-4(e), (f) shows the pre- and post-event orthorectified images, respectively. Figure 3-4 (g), (h) illustrates the close-up of the generated point clouds in a rectangular area shown in Figure 3-4(e), (f). From the close-up image, the concentration of the cloud points in the pre-event DEM is substantially higher than that of the post-event DEM. The pre-event data spatial resolutions were 1.0 m, whereas the post-event

data spatial resolutions were 1.5 m due to the different spatial resolutions of the original images. Since the spatial resolution and the pair quality of the pre-event data are higher, the post-event DEM and orthorectified image were resampled to a 1.0 m resolution by the cubic convolution technique for the following change detection operation in order to obtain a detailed morphological change.

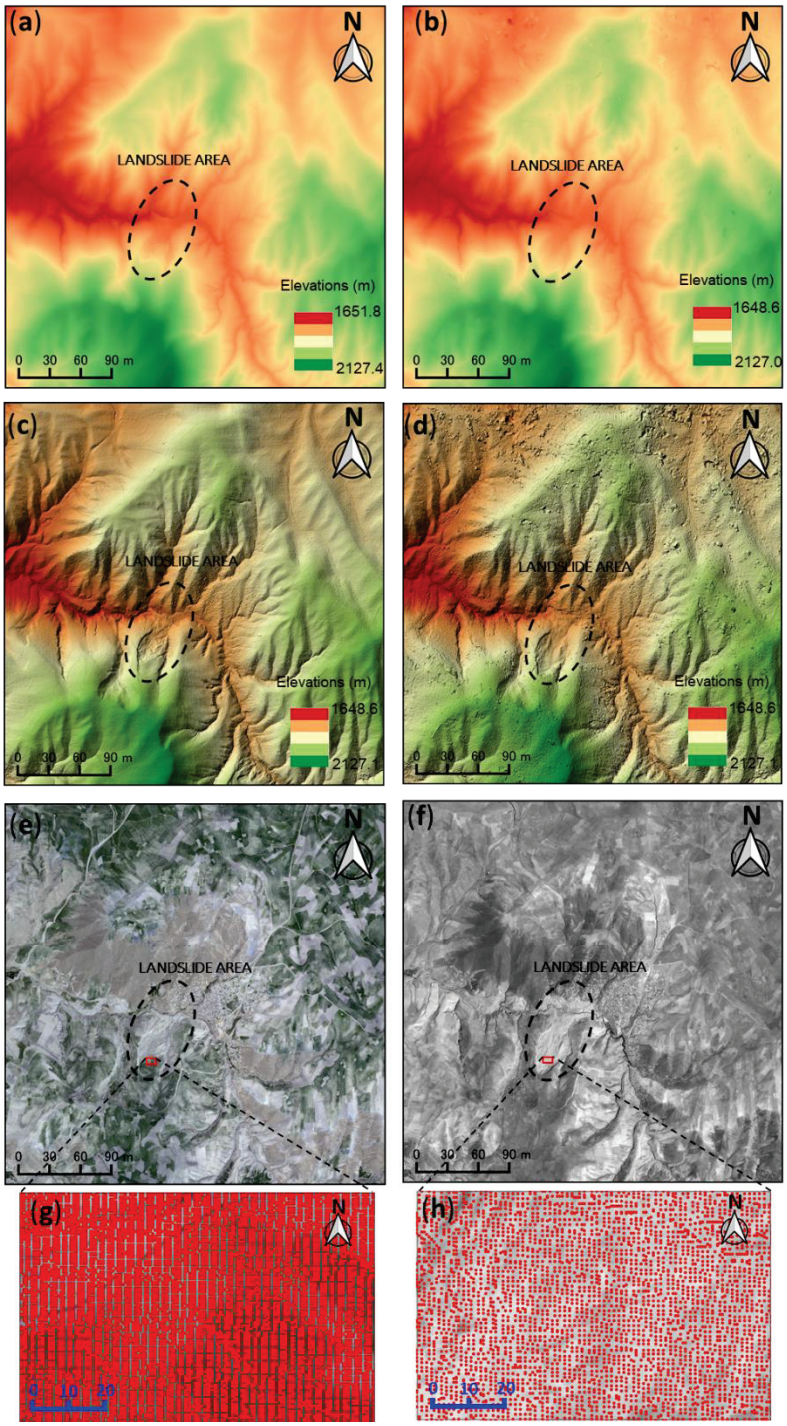

Figure 3-4. Data used in this study. (a) Generated 1 m-resolution pre-event DEM from the GeoEye-1 Satellite in June 2012; (b, c) pre-and post-event hillshades effects to the DEMs overlay with colors showing clear details of the study area; (d) generated 1 m-resolution post-event DEM from the IKONOS-1 Satellite in July 2014; (e) pre-event orthorectified multispectral image derived from GeoEye-1 images (0.5 m-resolution); (f) post-event orthorectified panchromatic image derived from IKONOS-1 images (0.8 m-resolution); close-up view of the generated point clouds of pre-event data (g) and post-event data (h) presents the rectangular area shown in (e, f).

The derived DEMs were georeferenced in GIS during the stereo matching operations based on the RPC files. Then, they were applied to the DoD technique by subtracting the pre-event image from the post-event image. The DoD (post-pre) obtained from the pixel-based change detection is shown in Figure 3-5. Although the DEMs were geometrically corrected by the RPC files, significant noises or errors in height values were found even in unaffected areas. These false detections would probably arise from the locational errors (e.g., horizontal errors) in the DEMs, indicating that two DEM images were not perfectly matched. Therefore, a further geometric correction would be necessary to accurately enhance the DEM's matching and accurately extract the geomorphological change. Here, in this study, a nonlinear mapping technique would be utilized to diminish the DEM's locational errors generated in DoD.

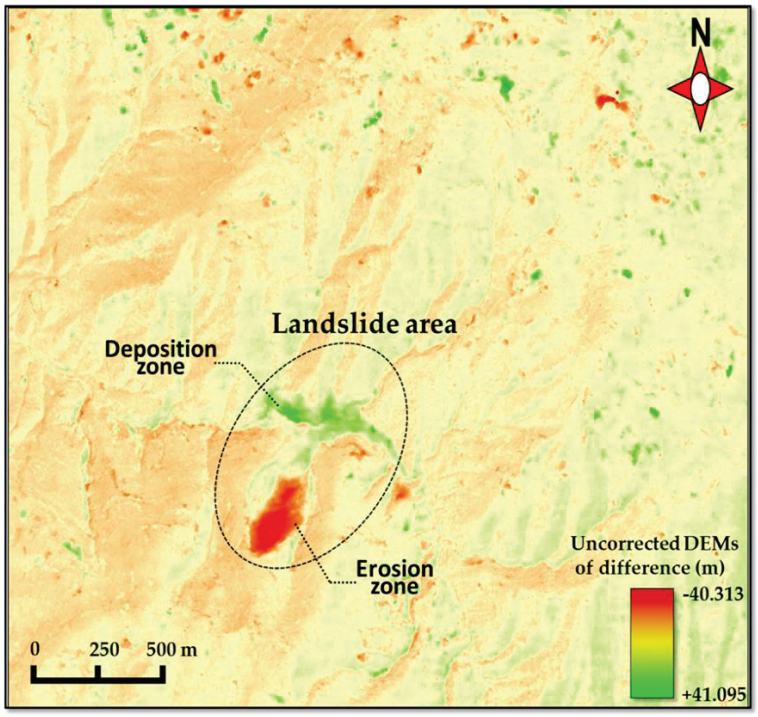

Figure 3-5. Uncorrected DEMs of difference (DoD) obtained from the pixel-based change detection using the pre-and post-event DEMs.

3.3. Nonlinear Mapping Method

An adaptive nonlinear mapping method was introduced by Kosugi et al., 2004, and Nakamura et al., 2002 to superpose a pair of aerial or satellite images accurately and detect pixel-by-pixel changes automatically. The method can geometrically correct the images even if rotational gaps and local skews are obtained in the images. The method was applied not only to aerial images but also to LiDAR-derived DEMs by one of the authors for quantifying volumes of debris flows (Miura, 2015). Hence, this technique was applied to the obtained DEMs in this study.

The flowchart of the nonlinear mapping technique for pre-and post-event DEMs is presented in Figure 3-6. This method consists of four operations: Shifting vector generation in subareas, consensus operations for shifting vectors, interpolation of consented shifting vectors, and the repetition of three previous operations until a satisfactory outcome has been achieved. In this analysis, the pre-and post-event DEMs are defined as the controller (reference) data and follower data, respectively. First, both DEMs are divided into subareas with the window size of N_W-by-N_W pixels (Figure 3-7). The segmented subarea ($N_W \times N_W$ pixels) in the follower data looks for the best-matched segment in the given segment's neighborhood (N_S pixels for left, right, upward, and downward) in the corresponding controller data by adopting the smallest elevations' difference using the following formula:

$$s(i_c, j_c) = \frac{1}{{N_W}^2} \sqrt{\sum_{j=-(N_W-1)/2}^{(N_W-1)/2} \sum_{i=-(N_W-1)/2}^{(N_W-1)/2} \{d_1(i_c + i, j_c + j) - d_2(i_c + i + dx, j_c + j + dy)\}^2} \quad (3\text{-}1)$$

The elevations' difference (s-value) is calculated in each subarea. Here, d_1 and d_2 are the elevations in the pre-and post-event DEMs, respectively, and i_c and j_c indicate the subarea's central location in x- and y-directions, respectively. The shifting vectors are determined from dx and dy in pixels when the minimum s-value is obtained within the given search area in N_W-

by-N_W pixels. It would be difficult to search for the appropriate shifting vectors in landslide-affected areas due to the fact that the ground movement significantly changes the topography after the event. Since the false shifting vectors would be generated in such changed areas, the shifting vectors need to be corrected considering the vectors in the altered areas' vicinities.

The consensus operation will be performed to correct the overestimated shifting vectors or false generated shifting vectors. The first scalars of the shifting vectors are calculated using Equation (3-2) in all the subareas.

$$d = \sqrt{dx^2 + dy^2} \tag{3-2}$$

Figure 3-8a shows the schematic diagram for the histogram of the vectors and threshold selection to two classes. The threshold value of the vectors (d_{th}) is determined by maximizing the ratio of inter-class variance (σ_B) to the total variance (σ_T) calculated Equations (3-3) to (3-5) (Kosugi et al., 2004; Nakamura et al., 2002; Otsu, 1979)

$$d_{th} = d \text{ s.t. } \max_d \left(\frac{{\sigma_B}^2(d)}{{\sigma_T}^2(d)}\right) \tag{3-3}$$

$${\sigma_B}^2 = \frac{n_1(m_1-m_0)^2+n_2(m_2-m_0)^2}{m_1+m_2} \tag{3-4}$$

$${\sigma_T}^2 = {\sigma_1}^2 + {\sigma_2}^2 \tag{3-5}$$

Here, m_0, m_1, and m_2 indicate the mean value of d for all the vectors, the mean value in class 1, and the mean value in class 2, respectively. Additionally, n_1 and n_2 are the number of vectors in classes 1 and 2, respectively. In a similar manner, σ_1 and σ_2 represent the variances of the vectors in classes 1 and 2, respectively. When the d-value in a subarea is larger than d_{th}, the vectors are classified to class 2. In that case, the shifting vectors are corrected by giving median values of dx and dy obtained within the neighborhood subareas (N_C-by-N_C subareas), as shown in Figure 3-8b. The shifting vectors are provided to all the pixels from the subareas'

vectors by the bilinear interpolation technique. These operations are repeated by the given number of iteration (*n*). Finally, the controller data is geometrically corrected based on the shifting vector in each pixel. Figure 3-9 illustrates the comparison of the schematic plan and profile before and after the nonlinear mapping-based geometric correction. Four parameters, N_W, N_S, N_C, and n are required to perform the nonlinear mapping technique.

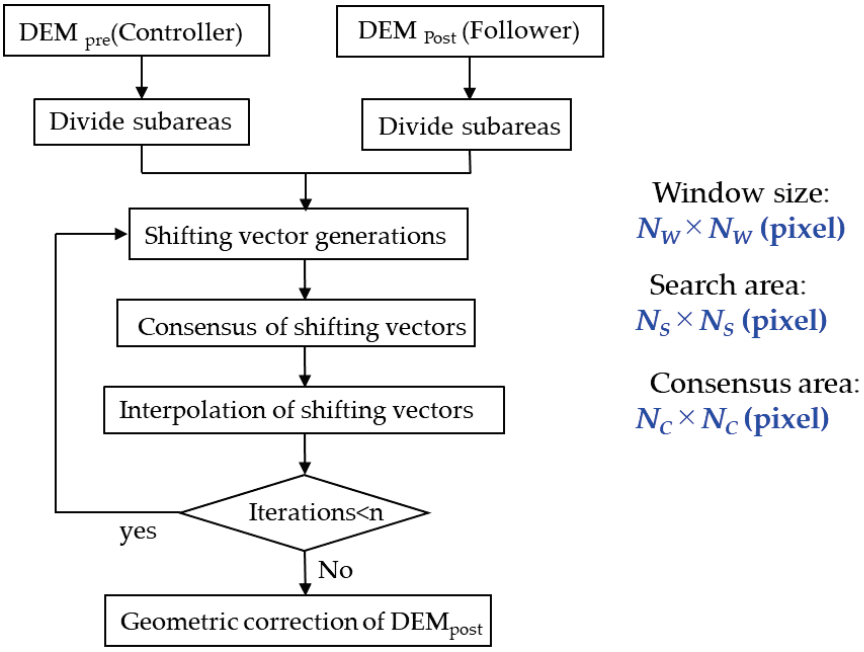

Figure 3-6. Flowchart of the nonlinear mapping technique.

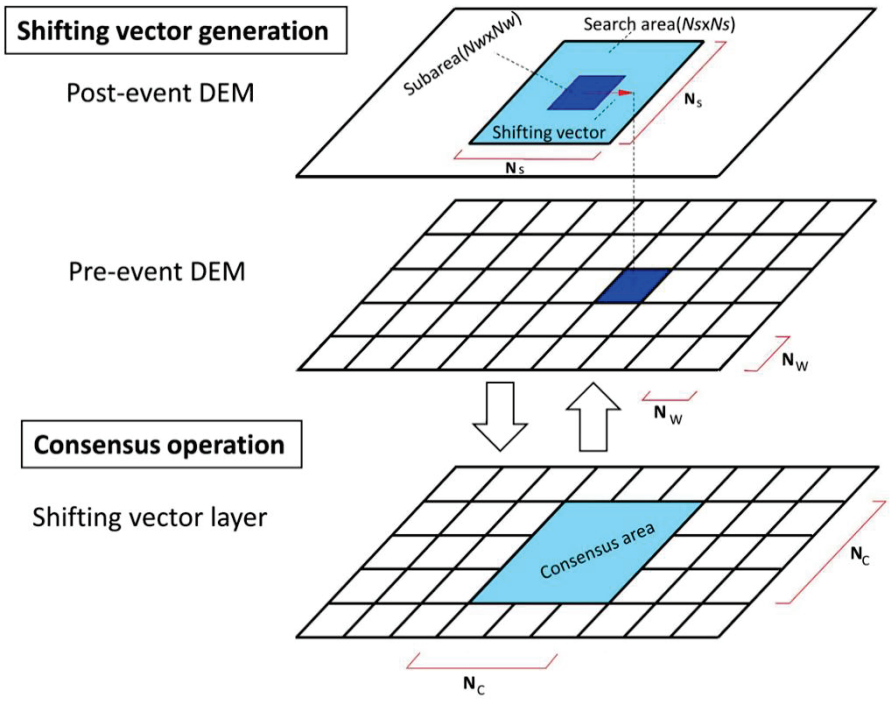

Figure 3-7. The schematic diagram for nonlinear mapping operations presents the segmentation of both pre – and post – event DEMs, the matching segments process, generating shifting vectors, and correcting false generated shifting vectors using the consensus operation, the figure is modified from (Miura, 2015).

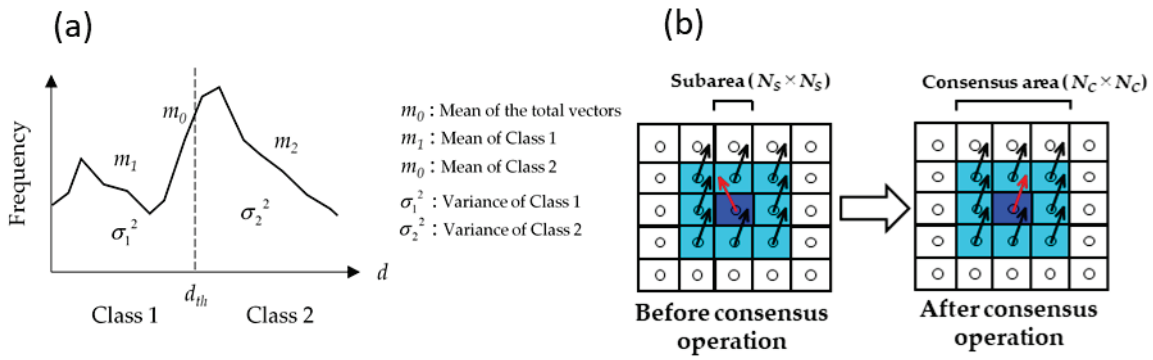

Figure 3-8. Schematic diagrams of (a) the histogram of shifting vectors and thresholding (b) present how the direction of generated shifting vector (red arrow) is corrected in the same way as the neighboring arrows using the consensus operation, modified from (Miura, 2015).

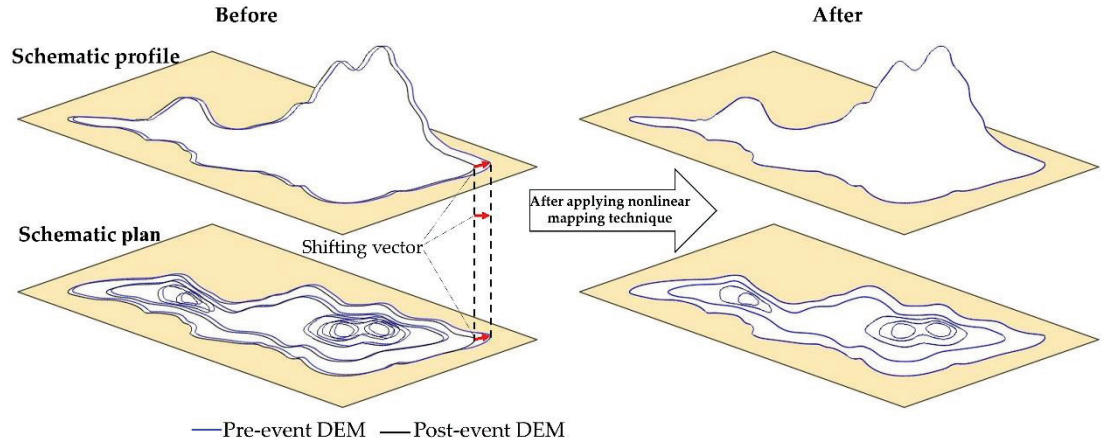

Figure 3-9. Schematic plan and profile denote a comparison of DEMs before and after the nonlinear mapping-based geometric correction.

3.4. Evaluation and Applicability of the Method

To apply the nonlinear mapping method to the pre-and post-event DEMs, the algorithm needs a combination of entry parameters. These key input parameters are N_W (window size or size of subarea), N_S (search area), N_C (consensus area), n (number of iterations). The selection of the parameters in the method was discussed in a selected testing zone with different combination values of these parameters. In this study, a set of scenarios were examined with different values of N_W, N_S, N_C, and n. In the following subsections, statistical and shifting vector assessments was performed. Based on the quality assessment result, the best possible combination of parameters (N_W, N_S, N_C, and n) was selected.

3.4.1. Statistical Assessment

As shown by the dotted rectangle in Figure 3-10, the nonlinear mapping technique was applied repeatedly with different scenarios for the selected test area. For instance, in every process of the analysis, the pre-event DEM subareas were given a different search area (pixel value) and consensus value to automatically search and match with the best possible corresponding reference point in the post-event DEM. Typical parameters illustrated in Table 3-2 were selected for the accuracy assessment. It is convenient to use descriptive statistics (mean and standard deviation) to evaluate different categories and identify the differences among other scenarios. If the geometric correction is successfully performed to the data, the DoDs mean value would be zero or close to zero in the unaffected areas. As shown in Table 2, different window sizes (e.g., N_W = 5,7,9…31) and search areas of $N_S \times N_S$ (3 × 3, 5 × 5, 7 × 7…31 × 31) pixels are evaluated through a repetitive iteration procedure. Finally, in this study, the window size (N_W = 5 pixels) and search area (N_S = 9 × 9) highlighted in Table 3-2 with bold text were chosen based on the lowest mean and standard deviations of DoD maps.

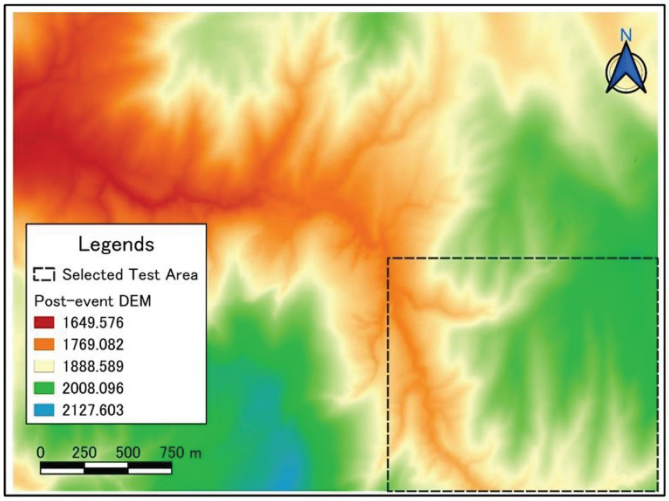

Figure 3-10. The selected test area is shown in a rectangle outlined with a dotted line.

Table 3-2. Means and the standard deviations of the DoDs for different parameters in the test area. Bold texts indicate the chosen parameters, which have the lowest mean and standard deviation.

No.	Size of Subarea (N_W)	Search Area (N_S, Pixel)	Consensus Area (N_C)	No. of Iterations (n)	Mean Value (m)	Standard Deviation (m)	Sum of Square	Remarks
1	0	0	0	0	1.278	3.337	2.00×10^7	Uncorrected
2	5	5	3	3	0.475	1.467	3.87×10^6	Corrected
3	5	7	3	3	0.221	1.254	2.83×10^6	Corrected
4	**5**	**9**	**3**	**3**	**0.152**	**1.152**	$\mathbf{2.39 \times 10^6}$	**Corrected**
5	7	5	3	3	0.862	2.197	8.68×10^6	Corrected
6	7	7	3	3	0.492	1.592	4.56×10^6	Corrected
7	7	9	3	3	0.166	1.308	3.08×10^6	Corrected
8	9	5	3	3	0.500	1.672	5.03×10^6	Corrected
9	9	7	3	3	0.247	1.468	3.87×10^6	Corrected
10	9	9	3	3	0.187	1.436	3.71×10^6	Corrected

3.4.2. Shifting Vectors Assessment

Figure 3-11(a)-(i) illustrate the generated shifting vectors for the scenario numbers 2-10 of Table 3-2. The selected test area of the pre-event DEM based on the entry-parameters described above; looked for the best matching segment in the vicinity of the corresponding reference point in the chosen test area of the post-event DEM. As shown in Figure 3-11, shifting vectors were generated if the best matching point is not the same as the reference point. During the operation analysis, more than nine profiles of shifting vectors have been generated. Here, in Figure 3-11, nine of them have been shown. A moderate vector movement that brings reasonable smoothness in the DEMs quality and considerably removes the locational errors in the unaffected area compared to another set of shifting vectors would be chosen from all the generated shifting vectors. After the comparison, in Figure 3-11, shifting vector with label c were selected, which corresponds to the parametric combination ($N_W = 5$, $N_S = 9$, $N_C = 3$, $n = 3$). Since the shifting of the vectors in the selected parameters is smaller than the other shifting vectors (e.g., scenario number five to ten in Table 3-2 shown by Fig. 3-11(d)-(i), the corrected DEM eliminated the locational errors in the unaffected area significantly compared to the other shifting vector-related DEMs. Moreover, the selected shifting vector had the smallest mean, deviation, and sum of squares, as discussed and shown in Table 3-2.

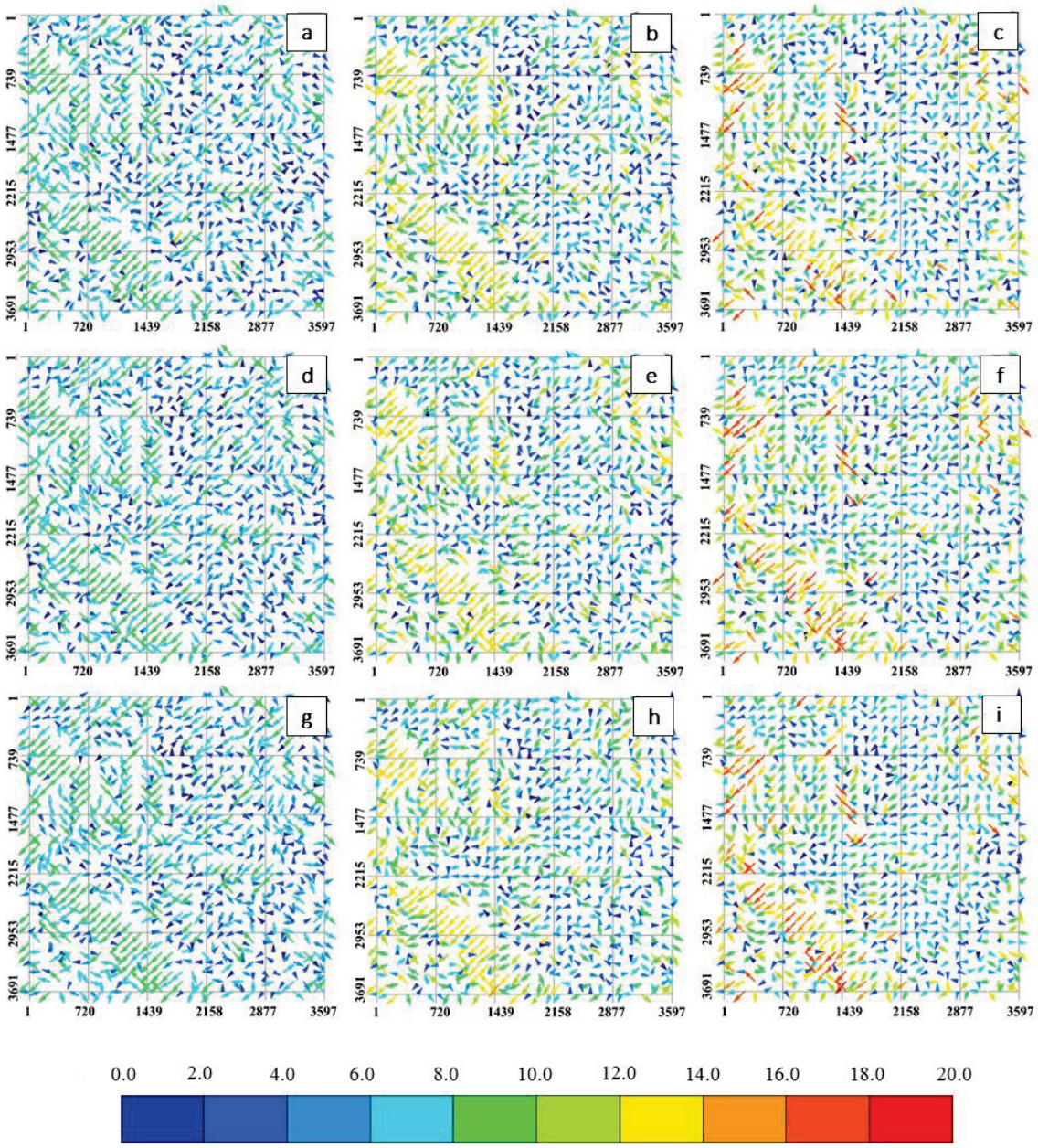

Figure 3-11. Generated shifting vector for nine scenarios. (a)-(i) correspond to the parameter combinations shown by the scenario numbers (2)-(10) in Table 3-2, respectively.

3.5. Quality Assessment

The histogram is a very handy way of graphically displaying the information contained in a single band of remotely sensed images (Jensen et al., 2015). In remote sensing, scientists usually examine histograms for each band to determine the quality of satellite images. The histogram presents the information by which one can figure out the quality of image data. In most cases, scientists show the before and after histogram graphs to compare the effectiveness of their image enhancement methods (Abdullah-Al-Wadud, et al., 2007). Hence, the distribution of the difference of elevations in the corrected DEM has been compared with the uncorrected DEM using histograms.

As shown in Figure 3-12, the uncorrected DoDs histogram (red line) generated a negatively skewed distribution shape histogram indicating the poor quality of the data or the presence of additional noise in data. However, the corrected DEM histogram (blue line) produces a symmetrical frequency distribution. The values are distributed around a central value, and the pixel numbers decline away from this central point. The distribution graph completely changed to a bell-shaped and is called a normal distribution. It can be concluded that the data quality in DoD after applying the nonlinear mapping method dramatically increased. Meanwhile, the incorrectly detected errors have drastically decreased after conducting the nonlinear mapping method and choosing the parametric combination.

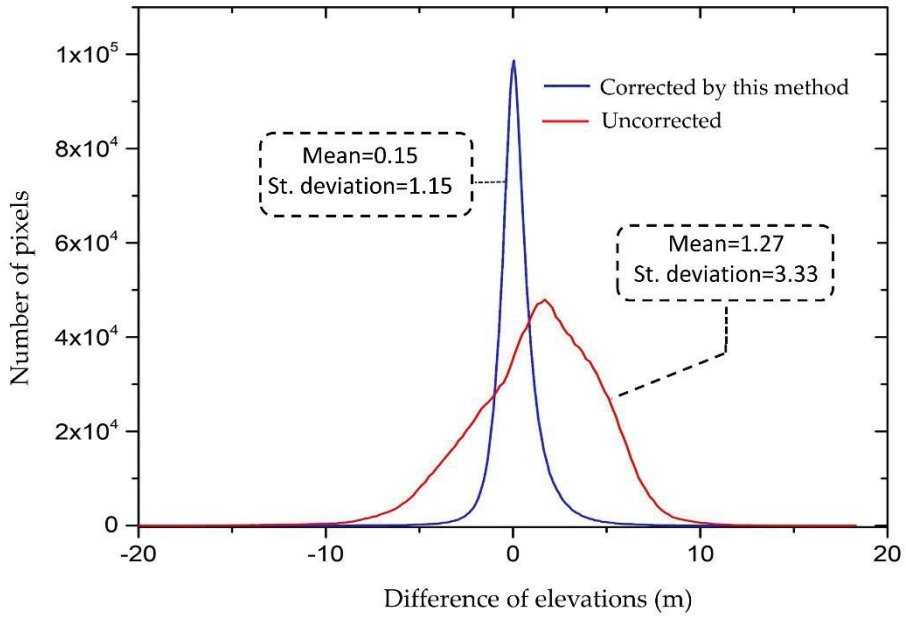

Figure 3-12. Comparison of histograms of the corrected and uncorrected DoD.

3.6. Landslide based nonlinear method's results

In this section, the profile cross-sections are evaluated using the corrected DEMs, including the landslide area to validate the nonlinear mapping method in Section 3.6.1, and presented the estimation of the soil volume through a comparison of the volume estimated from the uncorrected DEMs in Section 3.6.2.

3.6.1. Corrected and uncorrected DEMs profile cross-sections

The profile cross-sections are compared between the corrected DEMs and uncorrected DEMs to confirm the nonlinear technique's quality. Figure 13a shows the DoD obtained from the uncorrected DEM. Two cross-section lines was selected in the affected and unaffected areas, as illustrated by the A-A' and B-B' lines in Figure 3-13(b), (c), respectively. It was observed from the profile cross-sections that significant gaps between the pre-and post-event elevations are prominent throughout the cross-sections in the uncorrected DEMs. Figure 3-14(a) illustrates the DoD obtained from the corrected DEMs in this study, and the cross-sections in the A-A' and B-B' lines are shown in Figure 3-14(b), (c), respectively. It is confirmed that the locational errors (e.g., horizontal gaps) were significantly decreased, and the post-event line matches very well with the pre-event topographies.

The model performance was also evaluated in decreasing the locational errors using the quantitative value of the root means square error (RMSE) to confirm the degree of the matching in both corrected and uncorrected data in the unaffected area (Figures 3-13 and 3-14). This indicator has been frequently used to evaluate the prediction error quantitatively (Rawat et al., 2019). The RMSE of the corrected profile cross-section was obtained at 0.81 m, whereas the RMSE for the uncorrected profile cross-section was obtained at 3.81 m, which is more than four times larger than that of the corrected one. It suggests that the horizontal locational errors are the leading cause of the change detection errors not only in the unaffected areas but also in

the affected areas. The employed geometric correction model of the current study can be utilized for accurately extracting the geomorphological changes.

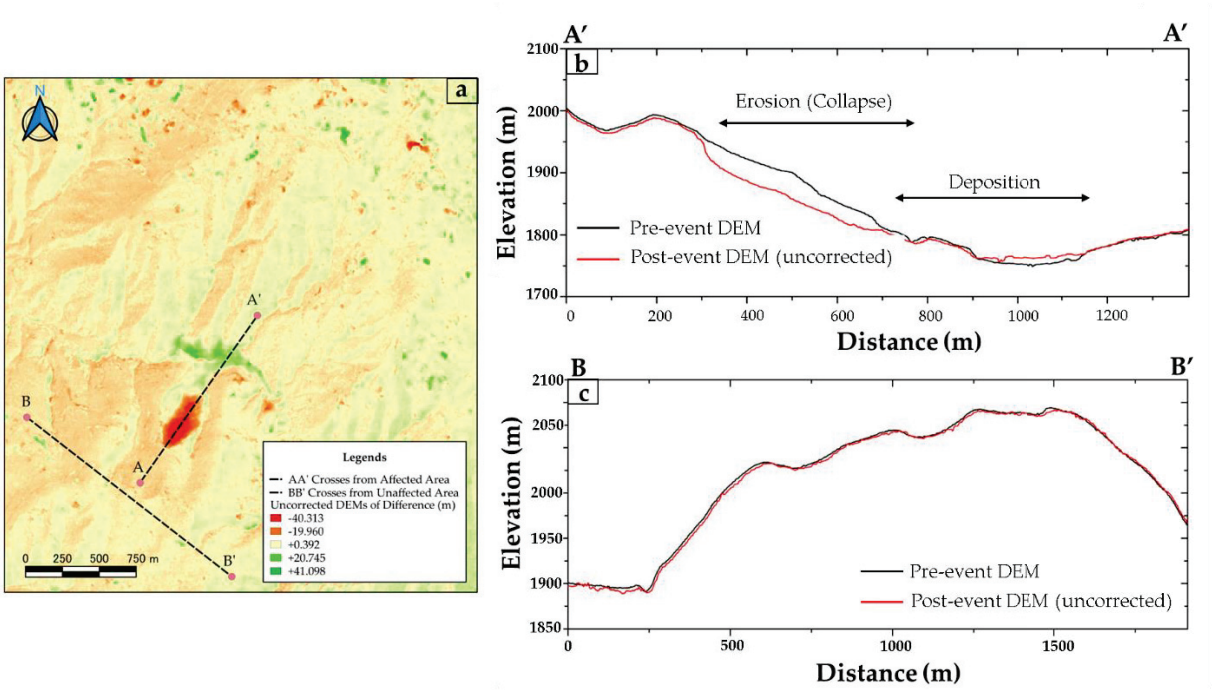

Figure 3-13. (a) Uncorrected DoD with the A-A′ and B-B′ cross-section lines. (b) Profile cross-section line (A-A′) passing through the affected area. (c) Profile cross-section line (B-B′) passing through the unaffected area.

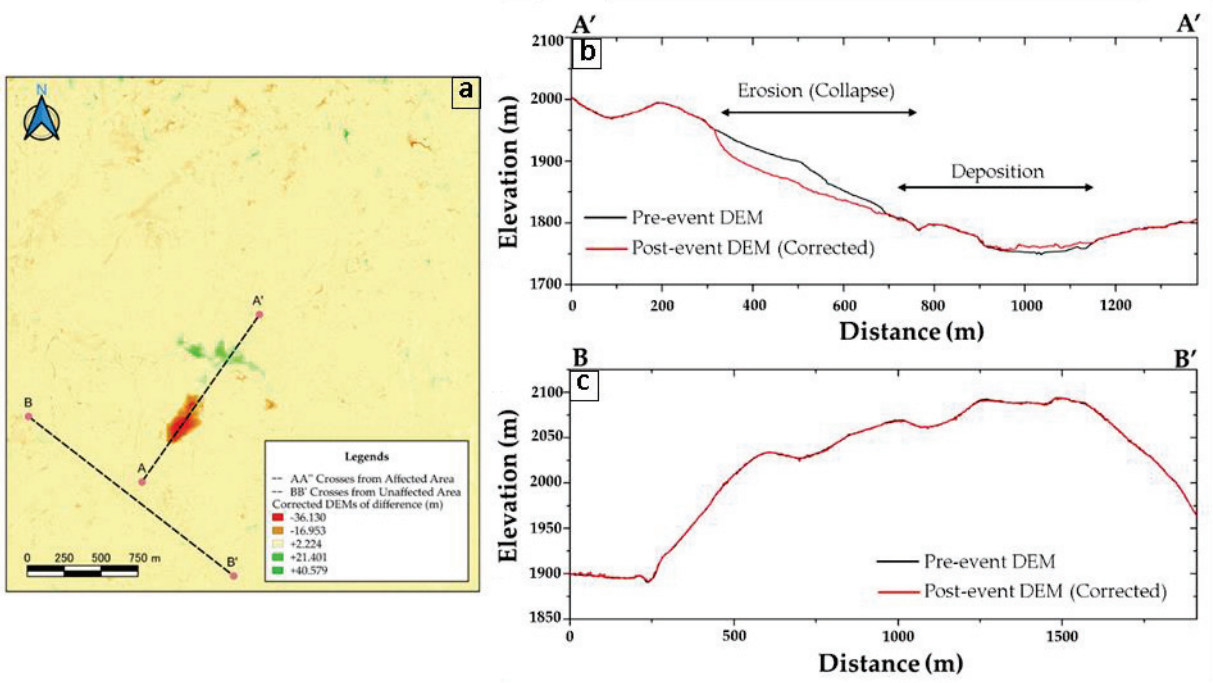

Figure 3-14. (a) Corrected DoD with the A-A′ and B-B′ cross-section lines. (b) Profile cross-section line (A-A′) passing through the affected area. (c) Profile cross-section line (B-B′) passing through the unaffected areas.

3.7. Volume Estimation

Before quantifying the volume of the displaced soil, the boundary line of erosion and deposition areas of the landslide need to be delineated. Figure 3-15(a) shows the DoD map (post-pre) obtained from the corrected DEMs with the landslide area delineated by the combination of the satellite images, the ground photos shown in Figure 3-2, and the cross-sections shown in Figure 3-15(b). The colors in the DoD map in Figure 3-15(a) illustrate the distribution of displaced soil depths in the Abe-Barek landslide disaster area. The DoD map consists of positive and negative pixel values. The negative values indicate soil erosion, which is filled in red to orange color pixels, and the pixel values range from (-37 m < DoD < 0 m). On the other hand, the positive pixel values correspond to the deposition of the displaced soil as shown in the blue to green pixel colors, and the pixel values vary from (0 m < DoD < +41 m).

Referring to the cross-sections drawn in Figure 3-15(b), the landslide moved in a complicated fashion in the erosion-affected sections. The post-event elevations were significantly decreased in the southern areas such as lines C-C', D-D', E-E', F-F', and G-G', whereas the elevations were increased after the landslide in the northern areas such as lines I-I', J-J', and K-K', as shown in Figure 3-15(b). Judging from the cross-sections in Figure 3-15(b), it can be claimed that in the upper slope section line C-C' to the line G-G' the erosion occurred, in which the eroded mass of the material is thought to move as a rigid block with a significant depth. By contrast, from the cross-section H-H' onward, which is the ending boundary of the erosion-affected area, the displaced material′s movements became more complicated. In other words, the mass of the material that was moving almost in a rigid block turned into many sub-slide surfaces at the lower reach of G-G', and each block in a separated fashion, choosing its direction to reach a remarkable distance.

From section I-I' onward, the post-event elevation increases as the movement continues with a distance towards the northern direction. It means that the landslide started depositing from I-I' on to the stopping points in the deposition zone. Finally, the landslide material that accumulated along the purple boundary polygon filled with a green color in Figure 3-15(a)caused the severe building damage. The redline polygon and dotted purple line polygon in Figure 3-15(a) shows the erosion area (upstream) and the deposition area (downstream) of the displaced materials, respectively.

The volume of the displaced material was estimated using the corrected DoD map by aggregating the positive and negative pixel values separately in their boundaries and multiplying them to the corresponding area boundaries. As an example, in Figure 3-16, the elevation change is presented along the cross-section line A-A'. It indicates the elevation difference between the pre- and post-event DEMs along the mentioned cross-section line shown in Figure 3-15. The positive values indicate the deposition of the material, whereas negative values indicate erosion of the materials. The maximum erosion depth along the cross-section line was obtained at 37.7 m, while on the contrary, the maximum deposition depth throughout the A-A' was estimated at around 12.7 m.

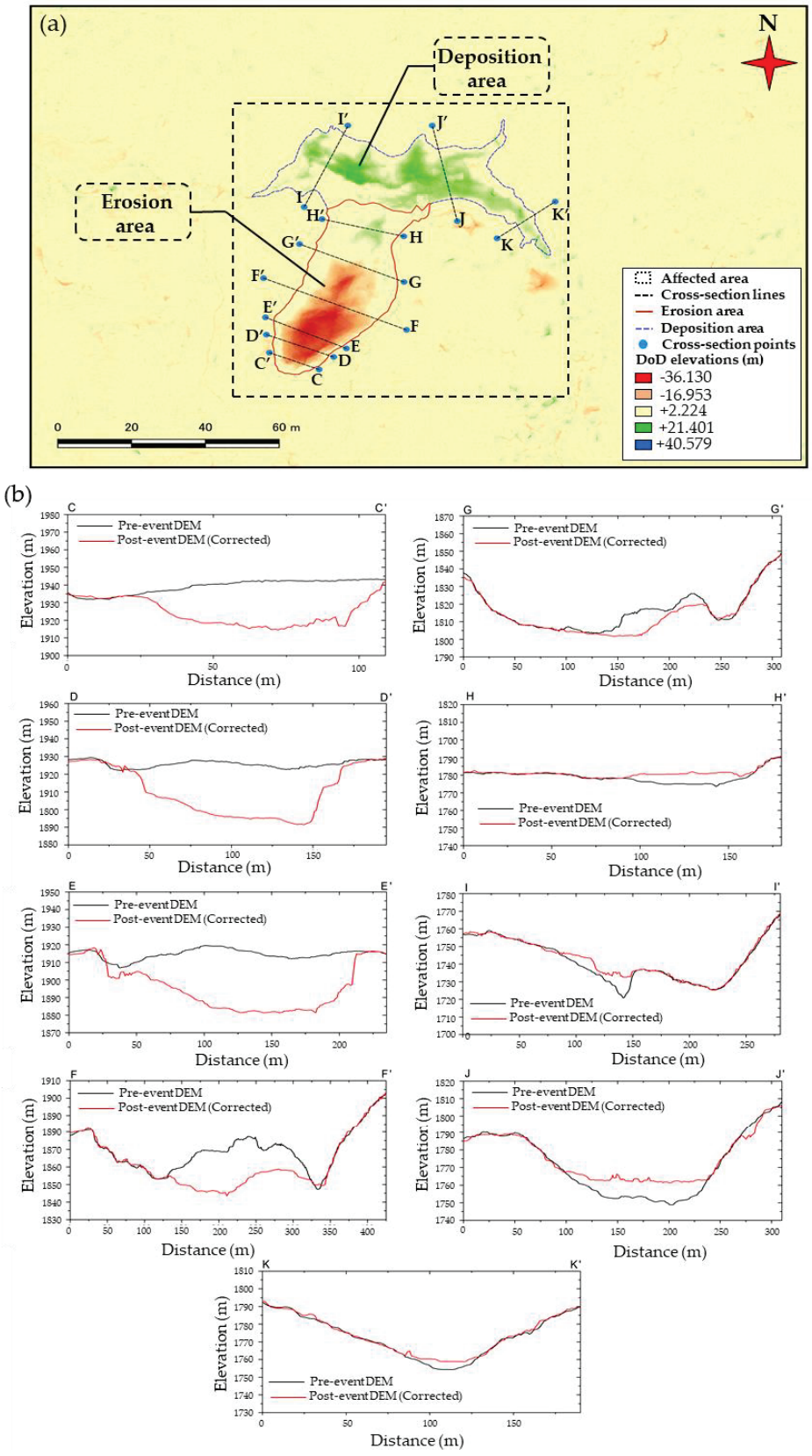

Figure 3-15. (a) DoD map obtained from the corrected DEMs presents the delineation of the landslide affected area and cross-section lines. (b) Cross-section profiles present the pre-and post-event surface difference throughout the landslide area.

The total erosion and deposition soil volumes in the upstream and downstream are summarized in Table 3-3. As highlighted in Table 3-3, the total volume of the eroded and accumulated soil in the landslide area by applying the nonlinear method was estimated at 1.05 × 10^6 m^3 and 5.73 × 10^5 m^3, respectively. The total erosion volume was nearly twice larger than the total deposition volume. This would be due to the fact that the soil in the downstream zone was dragged into buildings and parts of them flowed into the river.

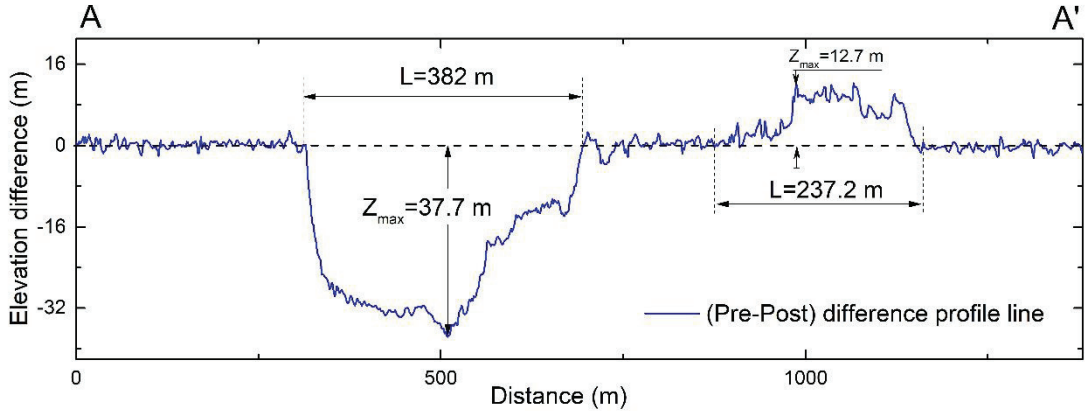

Figure 3-16. Elevation difference along the cross-section line A-A′ obtained from (pre-post) DEMs.

In addition to that, the volumes of the displaced materials were also estimated for the uncorrected DEMs and summarized in Table 3-3. The total erosion volume of 1.61 × 10^6 m^3 was approximately 53% larger than the one estimated from the corrected DEMs. The total deposition volume in the uncorrected DEM is 54% larger than that of the adjusted DEMs. The percentage increase between the corrected and uncorrected DoDs in the erosion and deposition zones was also summarized in Table 3-3. From the percentage increase, clearly, one can appreciate that the estimated parameters (volumes and depths) in the uncorrected DoD were significantly more extensive than that of the correct one. This implies that applying the proposed method considerably decreases the estimated volume of the soil. Furthermore, it reveals that the direct use of DoD without correcting the errors, leads to the overestimation of the landslide volume.

Table 3-3. Summarized erosion and deposition volumes for the corrected and uncorrected DoD.

	Corrected A			Uncorrected B			$(B-A/A)$ %	
	Erosion m^3	Deposition m^3	Total m^3	Erosion m^3	Deposition m^3	Total m^3	Erosion %	Deposition %
Upstream	-1.03×10^6	4.78×10^4	1.08×10^6	-1.56×10^6	8.74×10^4	1.61×10^6	51	57
Downstream	-1.58×10^4	5.25×10^5	5.41×10^6	-4.26×10^4	7.96×10^5	8.38×10^5	170	52
Total	-1.05×10^6	5.73×10^5		-1.61×10^6	8.83×10^5		53	54
Area (m^2)	1.22×10^5	1.23×10^5		1.22×10^5	1.23×10^5		-	-
Ave. depth (V/A), m	-8.6	4.6		−13.2	7.2		53	57

Similarly, the average erosion and deposition depths defined as the volume divided by the area were estimated by aggregating all the positive and negative pixel values within the landslide boundary line. The average depths were also presented in Table 3-3 for both the corrected and uncorrected DoDs, respectively. The average erosion and deposition depths for the corrected DoD were estimated at around 8.6 and 4.6 m, respectively. The average deposition depth was considerably lower than that of the erosion in the DoDs. This is due to the fact that parts of the deposited material were washed away to the downstream river, as mentioned above.

3.7.1 Previous landslide's volume versus current estimated one

In order to understand the scale of the Abe Barek landslide, a comparison was made with the area-volume relationship or power-law relation derived from the previous studies (Simotett, 1967; Rice et al., 1969; Abele, 1974; Innes, 1983; Whitehouse, 1983; Larsen et al., 1998; Martin et al., 2002; Guthrie et al., 2004; Guzzetti et al., 2008; Imaizumi et al., 2008; Rice et al., 1971; Guzzetti et al., 2009; Zhang et al., 2020) having a high confidence level at locations in different countries. The number of sample data, the study areas' limitations, and the obtained

relationships were summarized in Table 3-4. As reflected in Figure 3-17, the volume of the landslide appears to be slightly larger relative to the ground surface area. It reflects that the landslide occurred in a relatively small area with a significant loess thickness. Overall, Figure 3-17 indicates that the volume estimated by our analysis shows a good agreement with the previous studies and is located within correlation lines corresponding to the previous research.

Table 3-4. Empirical relationships linking the landslide area (A_L) to the landslide volume (V_L) obtained by various researchers.

No.	Number of Data	Maximum A_L	Minimum A_L	Equation	Source
1	207	1.9×10^5	2.3×10^0	$V_L = 0.1479 A_L^{1.368}$	Simotett, 1967
2	29	2×10^2	2.1×10^0	$V_L = 0.234 A_L^{1.11}$	Rice et al., 1969
3	53	6×10^7	2×10^5	$V_L = 0.242 A_L^{1.250}$	Abele, 1974
4	30	5×10^2	3×10^1	$V_L = 0.0329 A_L^{1.385}$	Innes, 1983
5	45	3.9×10^6	4×10^4	$V_L = 0.769 A_L^{1.250}$	Whitehouse, 1983
6	1019	1.6×10^4	5×10^1	$V_L = 1.826 A_L^{0.898}$	Larsen et al., 1998
7	615	5.2×10^4	2×10^2	$V_L = 1.0359 A_L^{0.880}$	Martin et al., 2002
8	124	$1/2 \times 10^5$	7×10^2	$V_L = 0.1549 A_L^{1.0905}$	Guthrie et al., 2004
9	539	1×10^9	1×10^1	$V_L = 0.0844 A_L^{1.4324}$	Guzzetti et al., 2008
10	11	4×10^3	5×10^1	$V_L = 0.19 A_L^{1.19}$	Imaizumi et al., 2008
11	37	1.5×10^3	1.1×10^1	$V_L = 0.328 A_L^{1.104}$	Rice et al., 1971
12	677	1×10^9	2×10^0	$V_L = 0.074 A_L^{1.450}$	Guzzetti et al., 2009
13	50	2.1×10^5	9.6×10^2	$V_L = 0.333 A_L^{1.399}$	Zhang et al., 2020

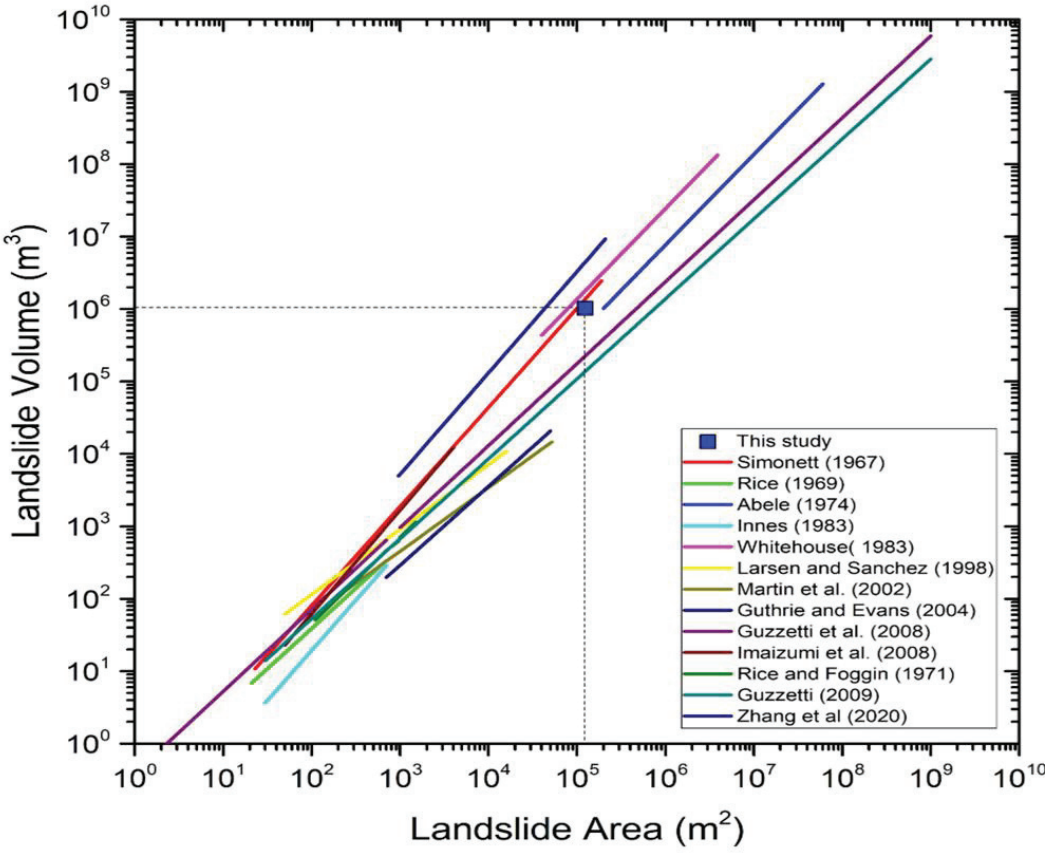

Figure 3-17. Comparison of the estimated landslide volume from current study with the empirical relationships linking the landslide area (AL) and volume (VL) resulted from previous studies.

3.8. Advantages and Shortcoming of the Method

The advantages of the technique presented in this study are summarized as follows: It can reduce geometric errors in the DoDs output almost automatically by providing adequate parameters without collecting GCPs; it can be applied to the DEMs, even significant morphological changes such as a large-scale landslide are observed in the data; and consequently, it can provide a more accurate volume quantification of the displaced material by landslides than a simple DoD analysis.

On the contrary, one of the nonlinear mapping method's main shortcomings is the time spent in scenarios for choosing the ideal input parametric combinations. For choosing such a parametric combination (N_W, N_S, N_C, n), it is needed to compare each scenarios' results and choose them based on a thorough evaluation, which will take a relatively long time. With the exception of that being said, the rest of the method is very fast.

Since in this study no discussion has been made about the absolute geo coordinate accuracy by using GCPs, the corrected DEM would still inevitably contain errors. A true error assessment can typically be conducted with enough GCPs (Tsutsui et al., 2007; Martha et al., 2010; Hsieh et al., 2016; Simonett, 1967; Nadi et al., 2020), which provides an actual error estimation. However, the error estimation using GCP in an insecure place, located in a remote area with high mountain and poor traffic accessibility, makes it nearly impossible to collect such data. Although some studies conducted such an assessment using the LiDAR-derived DEM as GCP (Tsutsui et al., 2007; Hsieh et al., 2016), the LiDAR observation has never been conducted in this area. Martha et al., 2010 suggested that aligning images using RPCs alone is enough for volume estimation. However, in this study, the nonlinear mapping technique is employed to align the DEMs with the maximum extent possible, to decrease the noise in the unchanged area, and to increase the accuracy of the analysis to the extent feasible.

3.9. Future Studies

Although the nonlinear mapping method's application significantly decreased the noise in the DoDs output, it subsequently may increase the accuracy of the landslide volume estimation result to a certain level. However, the error estimation has not been discussed in this work with the actual GCPs. Once such data are collected, much additional work needs to be done. For example, an error estimation of both depths and volume obtained from the nonlinear mapping and real GCP can be compared in a similar procedure conducted by (Tsutsui et al., 2007) using the evaluation change analysis technique. The shortcoming addressed in the earlier section may need further research to find a possible way of automatically selecting those parameters to accomplish the analysis faster. A comparative study, together with other techniques aimed at reducing undesired noises, can be applied to highlight the method's efficacy.

As final remarks, it should be emphasized that, in this study, the attention was to decrease the extra accumulated noises in nonaffected areas of DoDs output and to illustrate the impact of the adopted nonlinear mapping technique in decreasing the estimated landslide volume compared to the result coming from directly using DoD. The approach applied in this study aimed to estimate the volume of a large-scale landslide after decreasing the accumulated noises in the DoDs output. In addition, it has the potential to quantify the volume of the landslide in a critical disaster time with a relatively shorter time, without using any extra actual GCPs.

3.10. Summary of this chapter

The nonlinear mapping technique is utilized to detect and estimate the volume of the landslide affected area using stereo pair high-resolution satellite imagery. It is being stressed that the method can successfully be used in the image processing analysis to conduct mapping tasks, diminishing the geometric errors accumulating in the unchanged areas of the DoDs output, and finally, obtain the volume and average depth of the displaced material in the disaster area to ease the crisis management support and contribute very well to the more effective planning of the disaster relief and restoration.

The technique presented in this study was employed in a large-scale landslide that occurred on 2 May 2014, in Abe Bare village, Badakhshan, Afghanistan. Using the DEMs of the difference change detection technique, the DEMs of the landslide affected area was generated from the pre-and post-event satellite stereo-pair images. Although the DEMs were corrected using the RPC method, registration noises or locational errors were still spotted in the nonaffected areas. The nonlinear mapping technique was employed to diminish the aforesaid geometric inconsistencies or registration noises and enhance the accuracy of the process analysis. The proposed method has been coded in such a way that, in the selected testing zone with the given combinations of parameters, the post-event DEM (follower data), superimposes on the pre-event DEM, and pixel by pixel, scanning neighboring vicinities for the best possible matching points in the pre-event DEM (controller data). In this study, nine scenarios were examined with different values of N_W (window size or size of the subarea), N_S (search area), N_C (consensus area), n (number of iterations). As the quantitative and graphical comparison revealed, the locational gaps significantly reduced, and a bell-shaped histogram, also known as a normal distribution, was obtained. Moreover, statistical values, in particular, mean and standard deviations, decreased more closer to zero and one, respectively. Additionally, the obtained RMSE values also verified the nonlinear mapping's applicability in

decreasing the locational errors quantitatively. The required input components ($N_W = 5$, $N_S = 9$, $N_C = 3$, and $n = 3$) for processing the method were chosen after a thorough comparison and observation of the assessments.

The total eroded soil volume in the landslide area after adopting the nonlinear mapping method was approximately estimated at about 1.05×10^6 m^3, and the volume of the deposited soil acquired 6.73×10^5 m^3. The landslide's estimated volume was compared with the volumes obtained from the previous studies. The erosion volume of the soil obtained in this study showed a good agreement with that achieved in the previous studies. The average depth of erosion, mostly situated on the mountain's hilly side, was 8.6 m. On the contrary, the average depth of deposition, which typically situates in a flatted area, was estimated at 4.6 m. This highlights that nonlinear mapping has a considerable potential to reduce locational errors in mountainous regions. Therefore, it indicates a good applicability of the nonlinear mapping technique. It suggests that the method can be used efficiently on a routine basis and runs whenever a new landslide event has occurred if high-resolution stereo-pair images of the area become available.

CHAPTER VI

Assessment of the Charikar Flood Using Remote Sensing Analysis

4.1 Introduction

Flood is the most frequent and most damaged caused natural disaster which affects more people than any other types of weather-related natural disaster in Afghanistan. Low coping capacity and less consciousness of the people in Afghanistan is a prominent reason for most of the fatalities. Control of flood is very difficult, and, in most cases, it is very economically unaffordable for country like Afghanistan. However, it is possible to minimize the effects thorough efficient policy like enhancing the consciousness of the people by providing reliable information, providing flood susceptible area. To predict, prepare, prevent, and mitigate flood damage, preparing flood maps in flood-prone areas using remotely sensed data is very safe, affordable, and time-saving that plays an important role. Therefore, a method is proposed by which can rapidly detect, monitor, and predict the flood inundation area in any types of land, such as flat, built up, vegetated or even non-vegetated area. Since Normalized Difference Vegetation Index (NDVI) commonly used to detect land cover changeIn this study, the Relative Difference in Normalized Difference Vegetation Index (rdNDVI) approach is designed to identify and monitor flooding in Charikar based on NDVI values. The intention was to use same methodology as used in Landslide to detect and estimate the flood inundation area, but as discussed due the nature of nonlinear mapping techniques pairs of stereo satellite imagery was needed. Due to the lack of stereotype satellite image in the flooded area, this study employed the rdNDVI approach.

4.2 Study Area and the Flash Flood in Charikar

The study area is located between latitudes 35° 01′ 9.3’’ W and longitude 69° 09′ 55.67’’ N, which includes parts of the capital of the Parwan province (Fig. 4-1). The city lies on the Afghan Ring Road, 69 km from Kabul along the route to the northern provinces. It connects Kabul and western parts of Afghanistan to northern parts of Afghanistan such as Mazar-i-Sharif, Kunduz, and Puli Khumri. Despite the proximity to Kabul, slightly more than half of the land is not built-up.

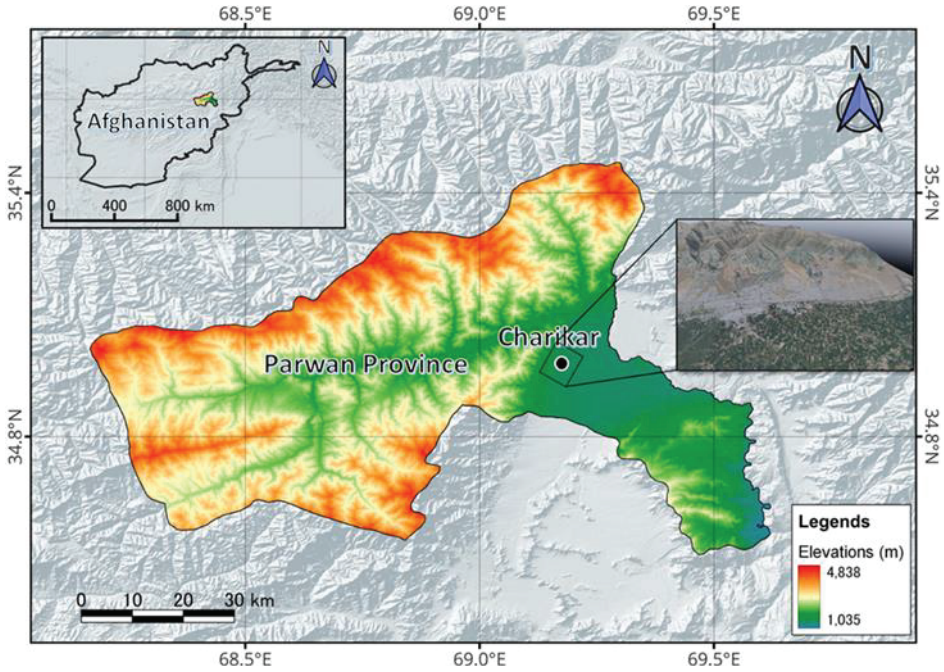

Figure 4-1. Topographical map of the study area showing how Charikar city is surrounded by high mountains of Hindukush which the elevation is between 1000 - 4000 m.

The study area includes the central Charikar district which has a total land area of 30,500 hectares that part of the city was affected by flood (Fig. 4-2). Ghorband river is flowing through Parwan province. It is a tributary of the Panjshir river, then a sub-tributary of the Indus River, then the Kabul river. The Ghorband runs entirely in Parwan province, where it gave its name to the Ghorband district. It is born in the eastern Sheybar pass (which connects the provinces of Parwan and Bamyan, or watersheds of the Ghorband and Kunduz river) and passes

in an eastbound direction which it maintains throughout most of its course. It runs along the south and the imposing central range of the Hindu Kush, receiving meltwater in the Sheybar pass area of Salang. It flows from this in a long valley between the high range of the Hindu Kush (north) and Koh-i-Baba in the south. It then converges with the Panjshir, on its right bank, 10 km east of Charikar. It flows through the districts of Sheikh Ali, Shinwari, Ghorband, and Surkh Parsa.

Parwan is located at a high altitude, 1,800 m (5,900 feet) above sea level. Winter is cold, with an average temperature in January of -1 °C, usually with freezing nights, and with possible peaks of -20/-25 °C; snowfalls are frequent and sometimes heavy. Summer is hot during the day, sometimes scorching, but nights remain usually cool. Precipitation in Charikar, fairly low, amounts to 300 mm per year. The rainiest season is spring. In summer, it rarely rains. In Charikar, the sun shines quite often even in winter, while in summer, it regularly shines.

4.3. The flash flood in Charikar

A devastating flash flood occurred near the residential areas in Charikar city of Parwan Province, Afghanistan on Aug. 26, 2020, killing over 100, most of the victims were children and women. More than 150 were injured (Tolo News, 2020), In the flash flood event, more than 17,000 people have been affected and nearly 2,000 homes were destroyed (The New York Times, 2020), The midnight floods surprised locals who were asleep. According to local witnesses, a roar was firstly heard and then a flood was arrived at their houses (The Guardian, 2020). Even police soldiers attempted air shooting to wake up people but unfortunately, most of the people did not notice. Rescue teams, locals and social groups were searching for the bodies of the victims. But many people were missing. Based on a report (Independent Farsi, 2020), a person was missing nine members of his family. The substandard mud houses on the mountainside near the Opyan village (Fig. 4-3) and some other areas around Charikar turned into rubble after the flood as shown in Fig. 4-2.

Figure 4-2. The affected area in Charikar A) people walking near the damaged houses after heavy flooding in the Charikar, Parwan province, Wednesday, Aug. 26, 2020. the photograph is taken from (Gul, 2020) accessed via Fox news; B) a man standing in front of what is left of his house after covering all his properties under heavy debris of flash flood Photograph taken from (Gul, 2020), C) Villagers soldiers search for victims in a mudslide resulted after a flash flood affected the area at Sayrah-e-Opiyan in Charikar (Photograph is taken from (Jalali, 2020). D) flash flood brought debris and boulders into the house and covered the car and injured and killed the people, (Photograph is taken from (Azadmanish, 2020), E) A general view of a building in Charikar covered with flooded debris of flooding in Parwan, Afghanistan August 26, 2020, this picture obtained in (The Guardian, 2020).

This tragic event, in addition to the intense war and the Covid-19 epidemic, further affected the health system, which is completely dependent on foreign aid for even some of its

most basic services. Charikar city is located in an area where a series of flood channels and valleys directly can put the residentials of the city under critical threat. Population pressure, flat area shortages, and inappropriate land development lead most of the people in Afghanistan to live in hilly flood-prone areas such as Charikar which highly likely lead to an increase in flood-induced building damage.

Figure 4-3. Compounds in Charikar city are at risk of flood due to a lack of regular urban planning, the flood path information is taken from the Surface Water Resources Department of Afghanistan.

As can be seen in Fig. 4-3, flood paths or valleys are shown in red color where each red area contains hundreds of residential buildings where the life of their residents can be in danger at any moment by floods. Government control and regular urban planning have been neglected in the construction of new towns and buildings. Irregular and arbitrary sale of land by landlords and local bullies, and most importantly, the absence of floods in the city of Charikar in recent years have encouraged people to feel that these susceptible areas are safe to buy and build the houses. The building and construction were growing at an unprecedented rate until a

devastating flash flood occurred and affected the people's life and the economy as shown in Fig. 4-2.

4.4. Materials

4.4.1. Sentinel-2 imagery

Sentinel-2 satellite imagery is a constellation of two earth observation satellites, developed by the European Space Agency (ESA) and the European Commission's ambitious Copernicus Program, consists of two identical satellites: Sentinel-2A, launched on June 23, 2015, and Sentinel-2B launched on March 7, 2017, available in various processed formats (ESA, 2015). Because the so-called Multispectral Instrument (MSI) products experience different stages of processing to reach a Level that becomes accessible by the users. From the main stages of Level-0, Level-1A, Level-1B, Level-1C, and Level 2. However, Level-0 and Level-1A are not accessible by users and are in the instrument source packet (ISP) format, which is a compressed raw image data format. Level-1B has radiometrically corrected imagery with Top-Of-Atmosphere (TOA) radiance which is made of granules 25 by 23 km long. Level-1C has formed in 100 × 100 km tiles in an orthorectified format in UTM/WGS 84 projection (ESA, 2015). Level 2A can be processed from Level-1C products using Sentinel-2 Toolbox. Level -1C and Level-2A are the most used product in land cover/ use mapping. This dataset is available free to the public domain as part of the free, full, and open data policy of the European Commission and European Space Agency.

Sentinel-2 data have been utilized in numerous research studies of earth sciences and atmospheric sciences since its launch and are ideal for agriculture, forestry, and other land management applications. (Szostak et al., 2018; Miranda et al., 2018; Wang et al., 2018; Taberner et al., 2020), flood mapping (Caballero et al., 2019; Dinh et al., 2019; Rättich et al., 2020), wetland monitoring (Solovey, 2020) and agricultural activities (Zhang et al., 2019; Kobayashi et al., 2020). The radiometric and geometric quality of Sentinel-2 data is technically superior to data acquired by other low spatial resolution data such as Landsat data. The

dominance of the Sentinel-2 is including a 10-day revisit time at the equator and a 5-day revisit time at mid-latitudes, as well as a spatial resolution of 10 m. Although they have the disadvantage of being affected by cloudiness, optical imaging satellites would be preferred for flood studies since the surface conditions of the affected areas are easily confirmed from the images compared to radar satellites.

In this study, Sentinel-2 data with Level 1C processing available in the GEE were used. These data have been orthorectified and radiometrically corrected providing top-of-atmosphere reflectance values. Bands 4 (Red) and 8 (Near Infrared) were used with original spatial resolutions of 10 meters. An automatic cloud masking procedure was applied on both opaque clouds and cirrus clouds using a bitmask band QA60 of the S2-1C product which has cloud mask information. As indicated in Table 4-1, two months containing nine photographs are selected for the pre-event period, and two months containing five images are selected for the post-event period. Unfortunately, the first post-event image after the flood event was not used in the analysis because the affected area was heavily covered with clouds in the image.

Table 4-1. Distinguished features of the satellite imagery used in this study and their observation conditions.

No	Image ID	Date Acquired	Cloud Cover (%)	Relative Orbit	Pass direction	Processing level	
1	S2A_MSIL2A_20200605T060641	2020-06-05	1.10	134	Descending	Level-1C	Before event
2	S2A_MSIL2A_20200615T060641	2020-06-15	0.63	134	Descending	Level-1C	
3	S2A_MSIL2A_20200625T060641	2020-06-25	4.23	134	Descending	Level-1C	
4	S2A_MSIL1C_20200705T060641	2020-07-05	23.75	134	Descending	Level-1C	
5	S2A_MSIL2A_20200715T060641	2020-07-15	35.2	134	Descending	Level-1C	
6	S2A_MSIL2A_20200725T060641	2020-07-25	8.63	134	Descending	Level-1C	
7	S2A_MSIL2A_20200804T060641	2020-08-04	3.06	134	Descending	Level-1C	
8	S2A_MSIL2A_20200814T060641	2020-08-14	1.20	134	Descending	Level-1C	
9	S2A_MSIL2A_20200824T060641	2020-08-24	9.87	134	Descending	Level-1C	
10	S2A_MSIL2A_20200913T060641	2020-09-13	8.7	134	Descending	Level-1C	After event
11	S2A_MSIL2A_20200923T060641	2020-09-23	0.23	134	Descending	Level-1C	
12	S2A_MSIL2A_20201003T060711	2020-10-03	0.82	134	Descending	Level-1C	
13	S2A_MSIL2A_20201013T060821	2020-10-13	11.82	134	Descending	Level-1C	
14	S2A_MSIL2A_20201023T060921	2020-10-23	0.68	134	Descending	Level-1C	

4.5. Methodology

The GEE cloud platform was used to execute multiple tasks impeccably from concurrent Sentinel-2 optical satellite data retrieval for flood mapping and to identify its impact on land use and land cover, and population on a parallel processing architecture. The Sentinel-2 images were retrieved during the pre-flood period (June 5 to Aug. 24, 2020), the event date (Aug. 26, 2020), and the post-event date (Sep. 13 to Oct. 23, 2020). The various pre-processing techniques have been conducted by the GEE beforehand.

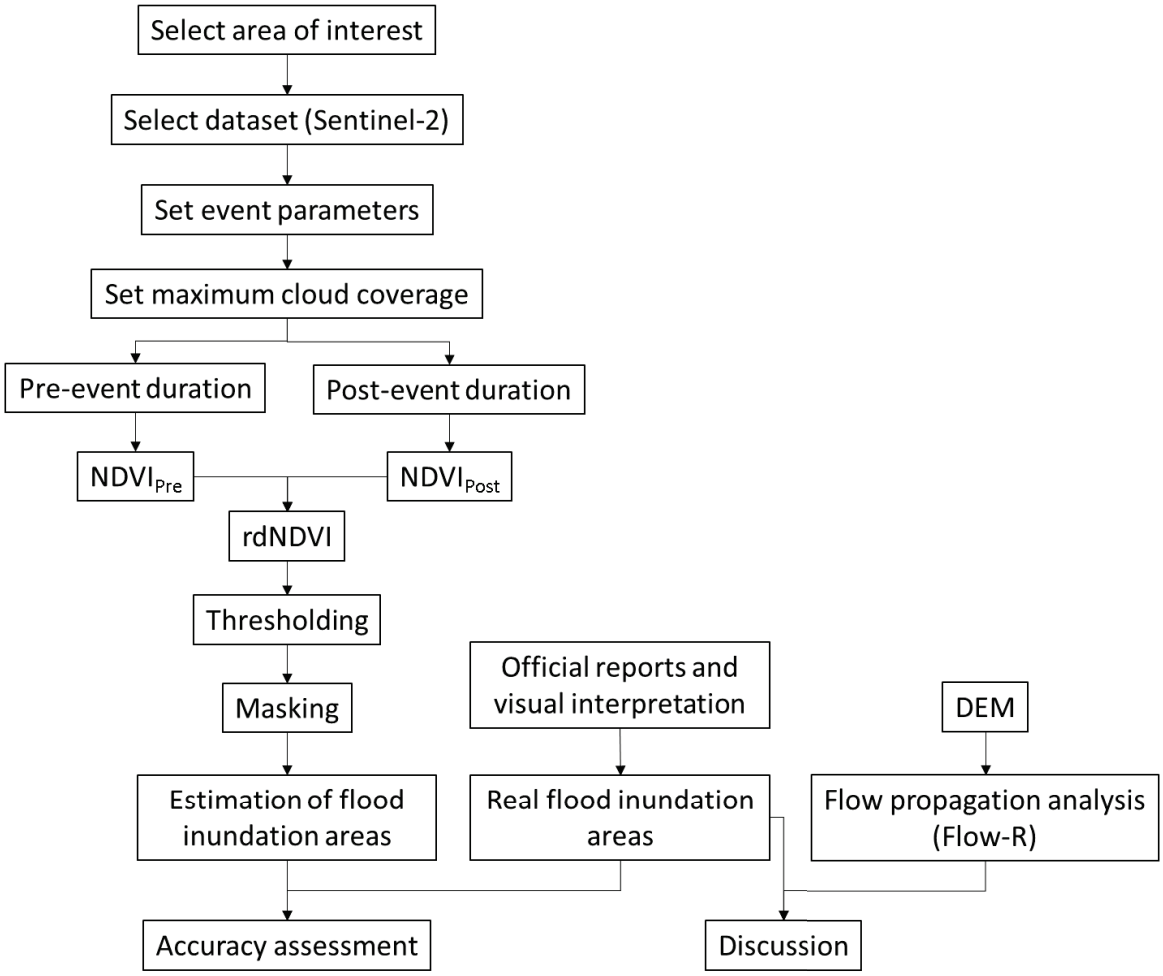

Figure 4-4. Flowchart of the methodology used in this study.

4.5.1 NDVI and Spectral water indices

This study did not attempt extracting or identifying the body of water in the impacted area because there was no standing water. However, the NDVI index is utilized to assess and identify the flooded zone because researchers have developed numerous indices for identifying flooded areas. This study would shortly examine the application of various indicators in the affected area in order to evaluate their performance in the affected region. To extract water bodies from remotely sensed data, several spectral water indices have been established, mainly by computing the normalized difference between two image bands and then applying an appropriate threshold to classify the outputs into two groups (water and non-water features).

The MNDWI and NDMI indices are utilized by most researchers to extract water bodies such as lakes, rivers, ponds, etc. The current study's purpose is to use rdNDVI to delineate the inundated area following a flash flood where there are no leftover water bodies. Then, a correlation is calculated between NDVI and three spectral water indices, and the output of each indicator for identifying changes induced by the flash flood in the research area is illustrated. Figure 4-5 (a) and (b) shows the true color Sentinel-2 images observed before the flash flood on Aug. 24 and after the flood on Sep. 13. Examining the rectangular rectangles depicted in Fig. 4-5 reveals a trail of the inundated area that remains mostly due to the flood event. The color of the soil in the affected area changed as a result of increased soil moisture after the flash flood. The reflectance of such darken wet soil is significantly low in infrared band such as near infrared (NIR) and short wavelength infrared (SWIR) as shown in Fig. 4-5 (c)-(f). It means spectral indices using NIR and/or SWIR would be effective to detect the flood-inundated areas.

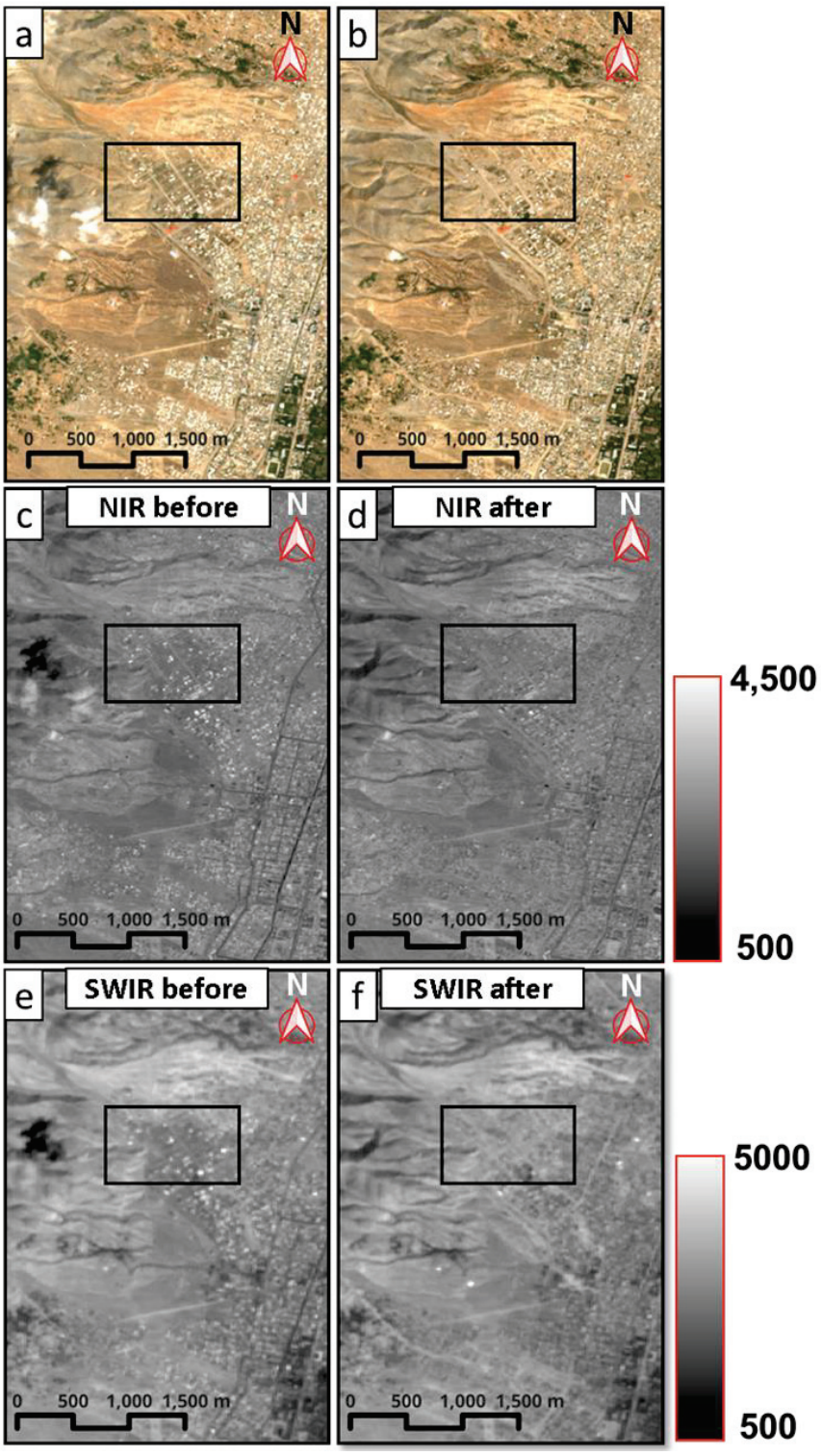

Figure 4-5. Observation of changes in the study area using pre- and post-event Sentinel-2 satellite images a) True-color images acquired on Aug 24, 2020; b) True-color image acquired on Sep 13, 2020. c) NIR band acquired on Aug 24, 2020; d) NIR band acquired on Sep 13, 2020; e) SWIR band acquired on Aug 24, 2020; f) SWIR band acquired on Sep 13, 2020; Rectangular area is selected on those areas to analyses the NDVI time series.

4.5.2. Normalized Difference vegetation Index (NDVI)

The NDVI index uses reflected light in the visible and near-infrared bands to detect and quantify the presence of live green vegetation. Simply put, NDVI is a metric that may be used to classify land cover in remote sensing areas and can measure the density and health of vegetation in each pixel. The first formal report of the NDVI was in (Rouse et al, 1973). The NDVI is expressed by Eq. (4-1):

$$\boldsymbol{NDVI} = \left(\frac{\boldsymbol{NIR} - \boldsymbol{Red}}{\boldsymbol{NIR} + \boldsymbol{Red}}\right) \qquad (\mathbf{4-1})$$

Where NIR is the near-infrared band and red is the visible red band. This index ranges from -1.0 to 1.0, essentially depicting green, with negative values originating from clouds, water, and snow, and values close to zero originating from rocks and bare soil. The NDVI function has very low values (0.1 or below) that correlate to vacant expanses of rocks, sand, or snow. Shrubs and meadows are represented by moderate values (0.2 to 0.3), while temperate and tropical forests are represented by large values (0.6 to 0.8). The estimated image of the NDVI index is visually presented in Fig. 4-6 to see the changes in the flash flood inundated area.

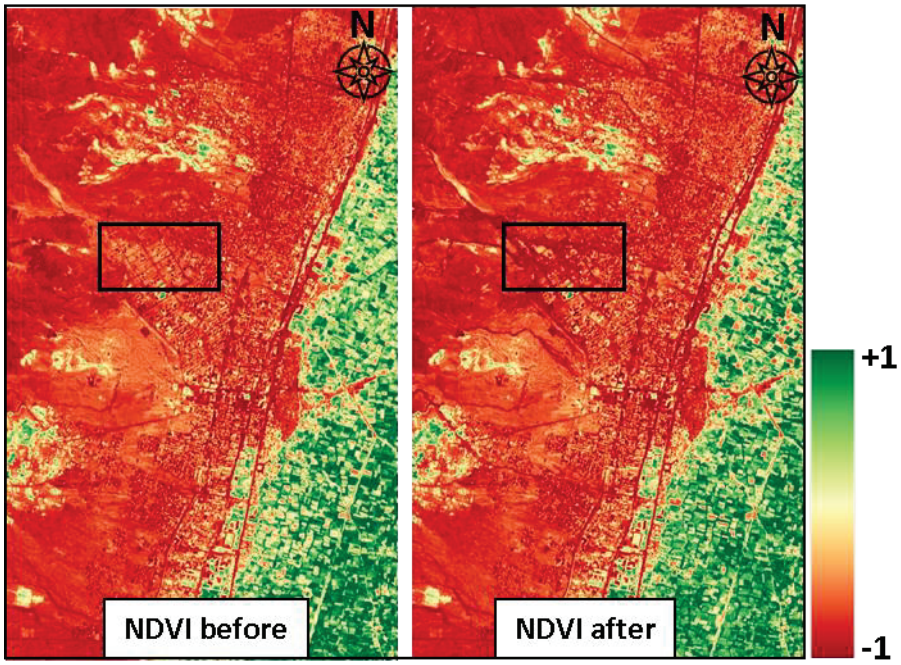

Figure 4-6. Observation of changes in the study area using pre- and post-event NDVIs.

4.5.3. Normalized Difference Water Index (NDWI)

The normalized difference water index (NDWI) was developed by (McFeeters, 1996) for detecting surface water in wetland regions and surface water measurement and is defined as:

$$NDWI = \left(\frac{GREEN - NIR}{GREEN + NIR}\right) \qquad (4-2)$$

Where, for Sentinel-2, green and NIR are the reflectance of green (band 3) and NIR (band 8), respectively. The NDWI value ranges from -1 to 1. (McFeeters, 1996) determined the threshold value at zero. That is to say, if NDWI is greater than zero, the type of cover is water; alternatively, if NDWI is less than zero, the type of cover is not water. According to the previous study (Xu, 2006), NDWI was unable to entirely differentiate built-up features from water features. Because the NIR reflectance was lower than the green reflectance, NDWI

displayed positive values in built-up features that were comparable to water. Therefore, (Xu, 2006) proposed the modified NDWI (MNDWI), which substituted the SWIR band (Landsat TM band 5) for the NIR band in McFeeters' NDWI equation (4-3):

$$MNDWI = \left(\frac{GREEN - SWIR}{GREEN + SWIR}\right) \qquad (4-3)$$

Where, for Sentinel-2, SWIR is the reflectance of short-wave infrared bands (Band 11). Eq. (4-3) is used to enhance open water features that are dominated by built-up areas. Noises from built-up land, vegetation, and soil is reduced considerably. This study visually presents the estimated image of the MNDWI index in Fig.4-7. This made it possible to observe the changes that had occurred in the region inundated by the flash flood.

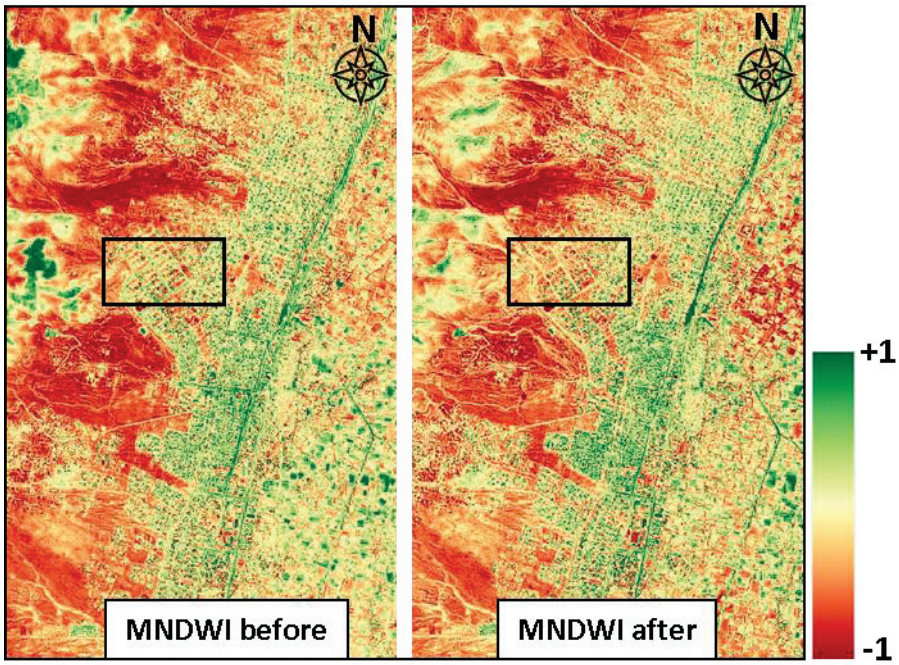

Figure 4-7. Observation of changes in the study area using pre- and post-event MNDWIs.

4.5.4. Normalized Difference Moisture Index (NDMI)

The Normalized Difference Moisture Index (NDMI) was used to determine vegetation water content. For Sentinel-2, the normalized difference moisture index (NDMI) is derived as a ratio between the NIR (band 8) and the SWIR (band 11) using Eq. (4-4):

$$NDMI = \left(\frac{NIR - SWIR}{NIR + SWIR}\right) \qquad (4-4)$$

Like most indices, the NDMI value ranges between -1 and 1. Negative numbers approaching -1 indicate water stress, whereas positive values suggest waterlogging. NDMI can detect water stress in early stages, before it becomes a serious problem. Furthermore, employing NDMI to monitor irrigation, particularly in locations where crops require more water than nature can provide, aids crop growth tremendously. In order to determine whether or not it is possible to observe the changes in the study area as a result of the impact of the flash flood using NDMI, the NDMI images in the study area is illustrated in Fig. 4-8. Initially, the performance of NDVI, MNDWI, and NDMI in the flooded area is evaluated, and then the correlation between these indices and NDVI is demonstrated.

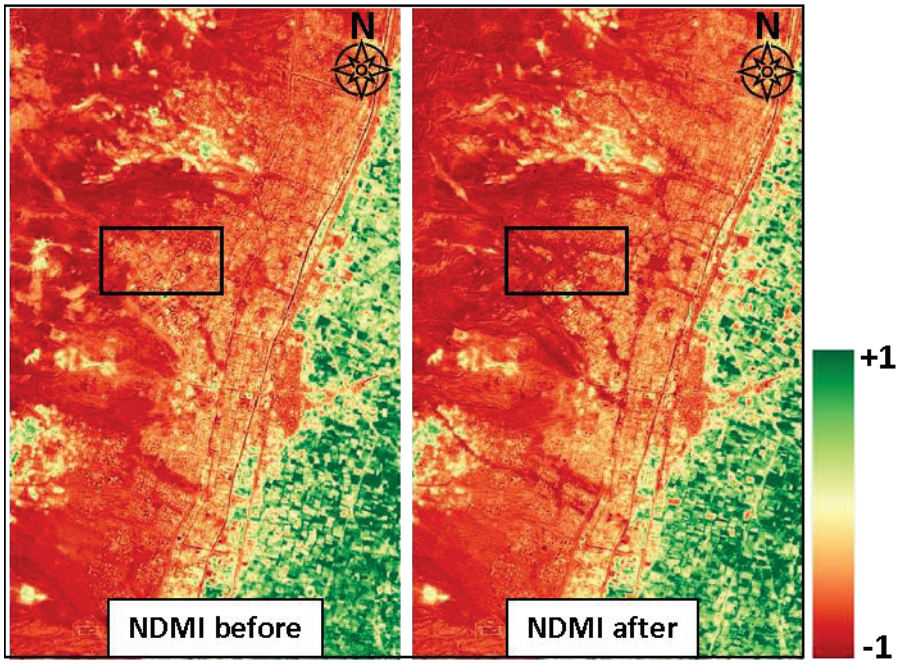

Figure 4-8. Observation of changes in the study area using pre- and post-event NDMIs.

The estimated images of the indices in Fig. 6-8 are visually presented to see the applicability of the index in detecting the changes in the flash flood inundated area. To examine how the images would alter after the flood, a completely identical color table ranging between

(-1 to +1) is specified for all of the estimated indices. As can be observed in Fig. 4-6, the color in the rectangle area of the NDVI-post event shifted to dark red (+1), although in the same area some changes were noticed in the MNDWI-post event (Fig. 4-7), but it's not as pronounced as the NDVI. Additionally, the NDMI, in the selected rectangular area, depicts the changes as a result of the flood more pronounced (Fig. 4-8), compared to the MNDWI (Fig. 4-8), particularly in the NDMI-after image, vast areas at the tops of the hills (surrounding the rectangular areas), are altered to darker colors (+1), indicating an overestimation of the detecting the inundation area.

In the inundated area depicted by the rectangular area in Fig. (4-6)-(4-8), a time series of NDVI, MNDWI, and NDMI is also displayed in Fig. 4-9 for the months of February through December of 2020. The result demonstrates that both NDVI and MNDWI values decreased just after the event over the flood affected area. However, NDMI does not follow a similar trend. In order to evaluate the relationship between the indices the correlation between NDVI, MNDWI, and NDMI is illustrated in Fig. 4-10.

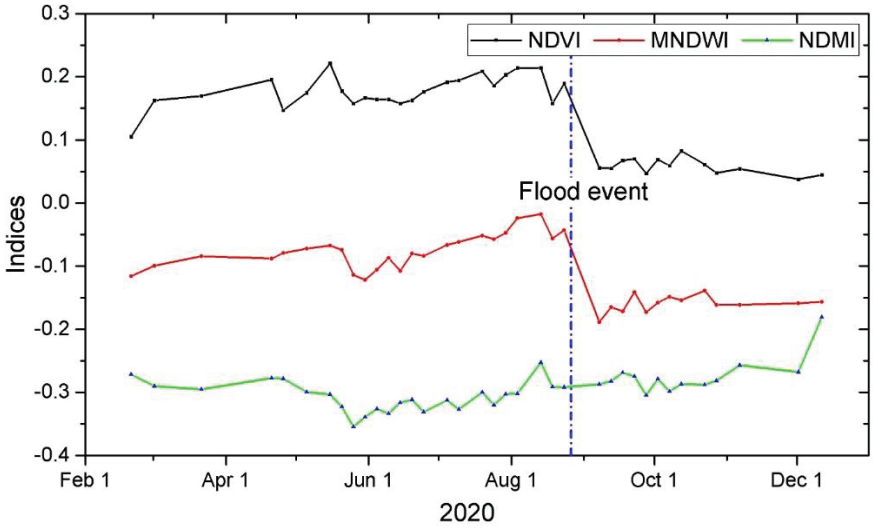

Figure 4-9. NDVI, MNDWI, and NDMI time series over the course of one year in affected area

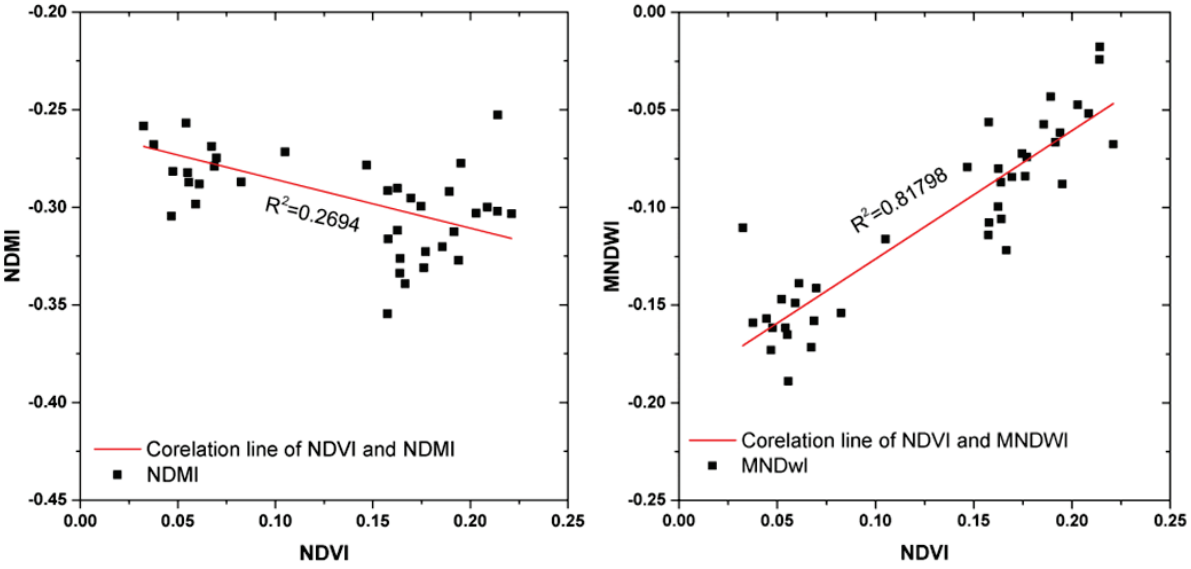

Figure 4-10. Correlation graphs between NDVI and NDMI and MNDWI.

It is clear from Fig. 4-10 that NDMI and NDVI have a weak negative correlation ($R^2 = 0.27$). NDVI and MNDWI, on the other hand, show a high positive correlation ($R^2 = 0.82$).

It is possible to identify the changes using most of the stated spectral water indices due to the impact of the flood on the affected area by manipulating the color table to some extent. These results indicate that the flood inundated areas can be detected not only by MNDWI but also by NDVI. Furthermore, the NDVI has a higher spatial resolution (10 m) compared to those of MNDWI (20 m) and NDMI (20 m) because the spatial resolution of the SWIR band is 20 m in the Sentinel-2 images. Higher spatial resolution images are expected to detect the inundation areas in more detail. For those reasons, this study intends to employ NDVI applicability in detecting flood-inundated areas.

4.5.5. Relative Difference NDVI (rdNDVI)

It is self-evident that the information contained in any given index varies substantially depending on the seasons and type of land cover, such as vegetation types. As a result, using a

single indicator to assess complex landscapes is technically difficult because change does not always correlate to the degree of effects (Miller et al, 2007). It's difficult to quantify changes in fractional forest, grass, or shrub cover since an NDVI drop in a low-NDVI drought-sensitive open forest area can have a greater impact than a similar percent loss in a high-NDVI dense forest (Norman et al, 2016). As a result, (Norman et al, 2020) proposed the Eq. (4-5):

$$rdNDVI = \left(\frac{NDVI_{Post} - NDVI_{Pre}}{\sqrt{NDVI_{Pre} + NDVI_{Post}}}\right) \times 100 \qquad (4-5)$$

In Eq. (4-5), $NDVI_{Pre}$ and $NDVI_{Post}$ present the greenest pixel composites in multitemporal pre- and post-event satellite imagery, respectively. Eq. (4-5) was originally used to help not only interpret or quantify the changes in complex landscapes such as fractional forest, grass, or shrub cover, particularly with low resolution imagery, but also help partially overcome problems that arise from NDVI's nonlinear responsiveness or NDVI "saturation" effect (Norman et al, 2020). When forest cover is low, a few trees added (or lost) have a higher impact on NDVI than a few trees lost in a dense forest cell. When both areas experience the same absolute change in NDVI, taking the square root of the denominator makes cells with high and low NDVI values fall more similarly. The result of Eq. (4-5) represents a normalized percentage of NDVI gained or lost. Later, (Scheip et al, 2021) used the rdNDVI technique to detect surface changes, primarily vegetation area changes, as a result of fire, volcanic eruptions, and landslides. (Scheip et al., 2021) never discuss the feasibility of the method in detecting flood inundated areas, particularly in non-vegetated areas, unlike the current work. This study focusses on feasibility of the rdNDVI-based detection, delineation, assessments of inundated area in non-vegetated arid region in Charikar, Afghanistan.

In this study, two temporal composites are made. One is a stack of all pre-event images, and the second contains all post-event images. Then, pre- and post -event NDVI is calculated for the so-called stacks. The greenest-pixel composite is a single composite or tiled image

generated from all images within the user-defined pre- and post-event window that records the pixel with the highest NDVI result as shown in Eq. (4-1). Instead of differencing true-color composites such as red, green, and blue bands, it exploits changes in surface vegetation by developing and differencing an NDVI band from the greenest-pixel composite image. Simply, the algorithm works in a way that from all-composite images it retains only the pixels with the highest NDVI value from the entire stack. This composite indicates the peak phenological cycle of pre- and post-event conditions. The rdNDVI indicator was derived using the peak phenological cycle calculated from the user input duration (in months) for the pre- and post-event duration.

4.5.6. Histogram-based segmentation

The thresholding-based segmentation algorithm is one of the simplest, most powerful, and most commonly used algorithms for the segmentation process. Segmentation based on histogram applies a thresholding value. This technique is used to segment the area of interest (AOI) from images with a uniformly bright background. Based on AOI, the threshold might have a single or multiple value. The entire image is pixel-by-pixel scanned in order to designate pixels as objects or background according to gray-level value and thresholding function (T). In the current study, to discriminate between the inundated and non-inundated area pixels, a histogram-based thresholding technique is used to find a set of thresholds. The method associates each pixel of the image (*f*) with a binary number that depends on the intensity of the pixels and a threshold T:

$$\mathbf{G(m,n)} = \begin{cases} \mathbf{1} & \boldsymbol{if} \;\; \boldsymbol{f(m,n) \geq T}, \\ \mathbf{0} & \boldsymbol{if} \;\; \boldsymbol{f(m,n) < T} \end{cases} \qquad \mathbf{(4-6)}$$

The above equation simply defines the binarization method. The thresholding process produces a binary image as its output. In eq. (4-6), pixels with an intensity value of 1 correspond to objects (inundated area), while pixels with a value of 0 correspond to the background (non-

inundated area). In histogram-based thresholding, it is critical to select the optimum threshold, and this process needs to be carried out in a way that produces the least amount of bias possible. The optimal value was obtained manually by iterating the value and observing the outcome. This procedure was repeated until it was determined that, with the selected value, the image contained almost all of the pixels from the original image. The histogram-based methods typically produce results that contain noise that needs to be removed before further analysis can be performed. In this particular research area, using sieve analysis in ENVI 5.3 to exclude each individual pixel that is less than 10. It is possible to eliminate noise by using larger (11 or 12 pixel) values. However, using pixels less than 10 would diminish most of the single pixel of such size in the vicinities of the inundated area, which may underestimate the inundation area.

4.5.7. Accuracy assessment procedures using confusion matrix

To validate the rdNDVI detection result, the flood inundation map was first created using visual interpretations of pre- and post-event Sentinel-2 images, as well as governmental reports from after the flood, as shown in Fig. 4. Confusion matrix is employed to evaluate the accuracy of detected inundation compared to the inundation map of the visual interpretation. Confusion matrices, also known as error matrices, are typically utilized as the quantitative method for characterizing the accuracy of image classification. These matrices contain information about actual and predicted classification. It is a table that illustrates the correspondence between the classification result and a reference image. The generation of a confusion matrix requires ground truth data, such as cartographic information, manually digitized photographs, and GPS-recorded results of field work or surveys. This data is also referred to as reference images. In this analysis, the reference image is a manually digitized version of an image that was compiled from various sources, including photographs taken after

the flood, published reports, and government survey reports. It is necessary to make a comparison between the pixels that have been classified and the truth data. The inundated and non-inundated regions of this study area were generated utilizing binarization thresholding techniques. This study utilized the results of the visually identified inundated reference map data to perform the accuracy assessment. The estimated inundated pixels located within the boundary of the reference map (visually identified inundated map) is the number of correctly identified pixels. On the basis of the confusion matrix, a pixel-by-pixel analysis of the image's accuracy was carried out. The accuracy of the outcome is determined by considering the user's accuracy, the producer's accuracy, the overall accuracy, and the kappa coefficient.

4.5.8. Flood susceptibility mapping model based on Flow-R

Remote sensing technology is a very useful tool for detecting and monitoring land-use changes after natural disasters. However, evaluation and prediction of hazardous areas for flooding are also important issues in considering countermeasures for future events. In order to talk about how well the simulation method works for figuring out flood inundation areas for future flash floods, semi-automatic debris flood mapping susceptibility is made using Flow-R and free DEM from ASTER Global DEM (ASTER-GDEM) (NASA et al, 2018) with 30 m spatial resolution (see Fig. 4). Flow-R is a freely available simulation software developed by (Horton et al, 2013) that has been used to simulate the flow propagation of debris flows and debris floods through a DEM. The Flow-R software is a path assessment of gravitational hazards that provides a substantial basis for a preliminary susceptibility assessment at a regional scale (Horton et al, 2013). It has been successfully applied to different case studies in various countries with variable data quality and satisfying accuracy. This study utilizes the Flow-R simulation to discuss the applicability of the technique in assessing flood areas for a future event. Although in this study, Flow-R is applied to a true disaster, such a simulation

technique is especially useful to identify vulnerable areas before the sources of an event are provided. The main input requires two steps to apply the technique. For applying Flow-r first, it is needed to provide source points using morphological and/or user-defined criteria. Second, debris floods are being propagated from the given source points based on simple frictional laws and flow spreading algorithms. Debris floods are caused by water moving quickly through steep channels with a lot of debris in them. Their peak flow is similar to that of water floods (Hunger et al., 2014).

The DEM used for the simulation of flood susceptible areas were 30 m, which is very low resolution. However, the developer of the Flow-R (Horton et al., 2013) reported that the quality of the produced map is of major importance for the result accuracy. In addition, Horton et al. (2013) suggest that a DEM resolution of 10 m is a good compromise between the amount of time it takes to process the data and the quality of the results. In addition, the hazard map that is generated by Flow-R is a possible future hazard map, which means that compatibility of one hundred percent is not required to be achieved. Because it only shows the areas that could potentially be hazardous. For Flow-R analysis, this study follows the methods described by (Horton et al., 2013).

4.6. Extraction of flood inundated areas

As described in the preceding chapter, the pre-event and post-event periods for this study are two months and two months, respectively. There were 14 photos available for the given time period. This study considered the total number of pre-event images and then changed the number of post-event images during the course of the study in order to evaluate and determine the shortest time required for the rdNDVI to analyze and identify the affected area. As illustrated in Figure 4-11, the analysis technique starts by combining all pre-event composites into a single post-event image (a). In the subsequent stages of analysis, two post-

event images are gathered, and in the final iteration, all pre-event images and post-event data in the study area are compared, as depicted in Figure 4-11 (a)- (e).

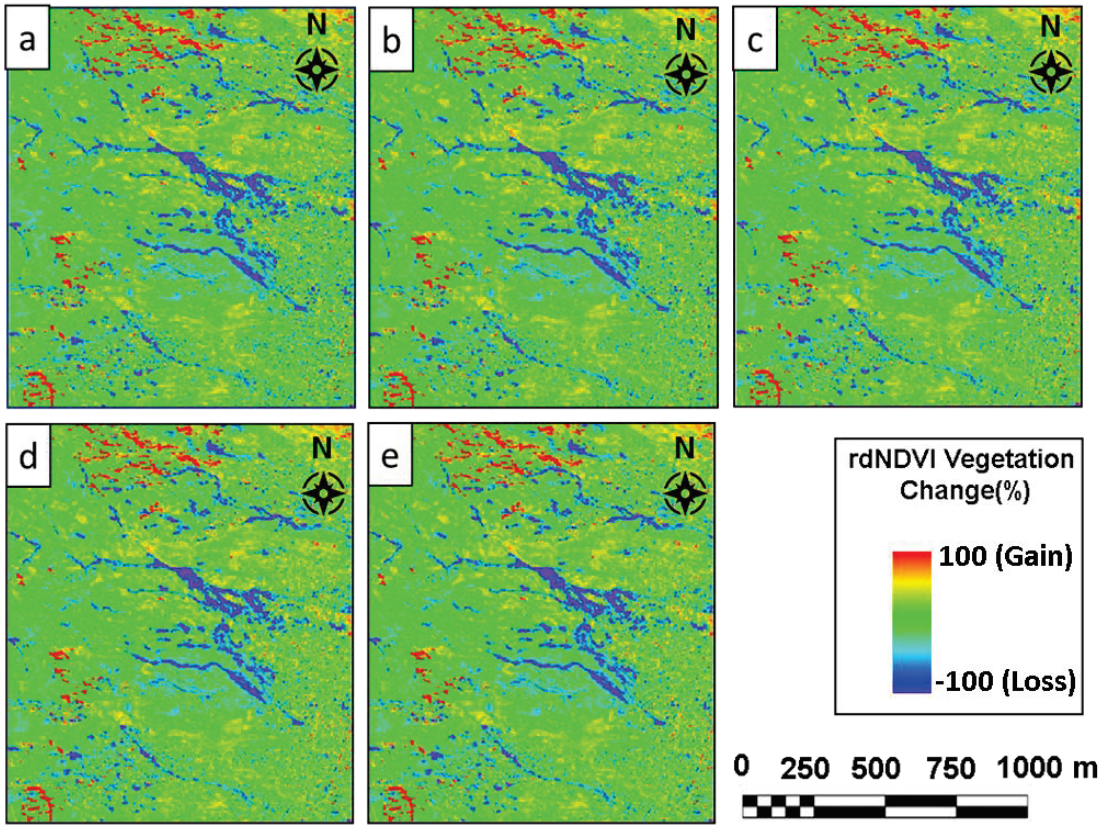

Figure 4-11. Result of rdNDVI map for five scenarios. Pre-and post-event images were acquired between June 5, 2020, and October 31, 2020. Figures (a)–(e) show the results of rdNDVI for all pre- and post-event images that were available and used in this study. (a) presents the result of rdNDVI which was generated with only one post-image acquired on Sep. 13, 2020. (b), (c), (d) and (e) represents the results obtained from two, three, four and five post-event images, respectively.

Figure 4-11 presents the rdNDVIs′ inundation map where blue color illustrates the decrease of NDVI as a result of the flood event. The colors other than blue show no change (green) and vegetation gain (red color). From Fig. 4-11, it can be clearly seen that by considering only one post-event image, a clear inundation map is obtained. By increasing the number of the post-event images, a slight change is noticed in the result of the inundation map.

The changes were so small that they were barely can be noticeable without a close-up of the image. Therefore, using only one post-event image and the rdNDVI algorithm, the utilized method can detect the flooded area. This study employs the image shown in Figure 4-11(a) for the rest of the study.

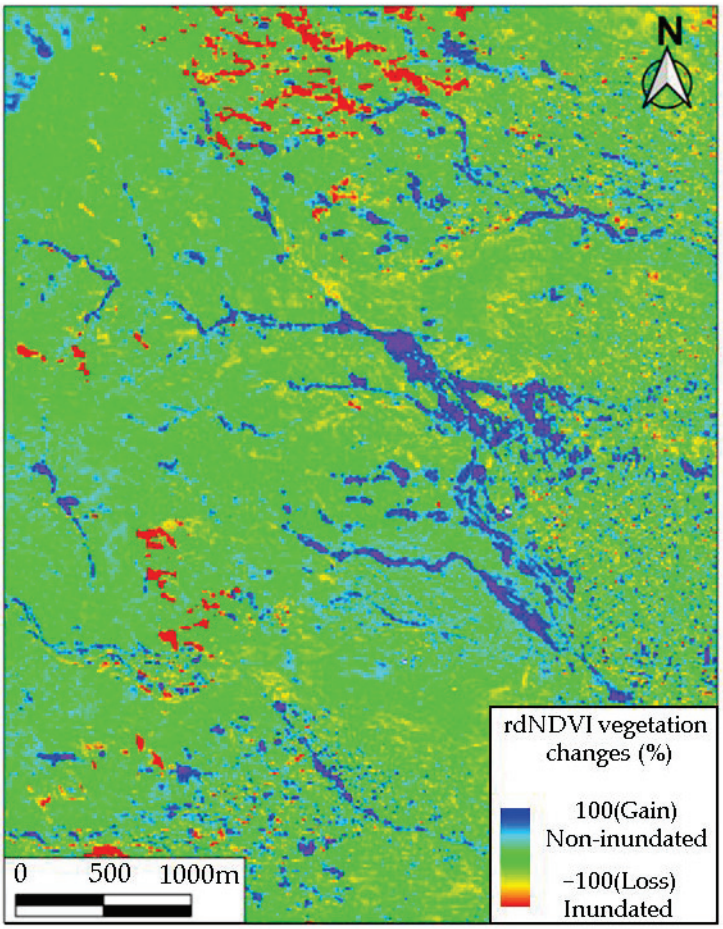

Figure 4-12. rdNDVI-based change detection image and greenest pixel composites (pre-event time: 2-months; post-event time: 16 days).

Figure 4-12 presents the larger map of the rdNDVI vegetation change in percentage. The blue color represents the loss of vegetation, which here means inundated areas. Whereas

red colors indicate vegetation gain or non-flooded areas' detection. As can be seen, the current technique rapidly detects the inundated area using the explained methodology.

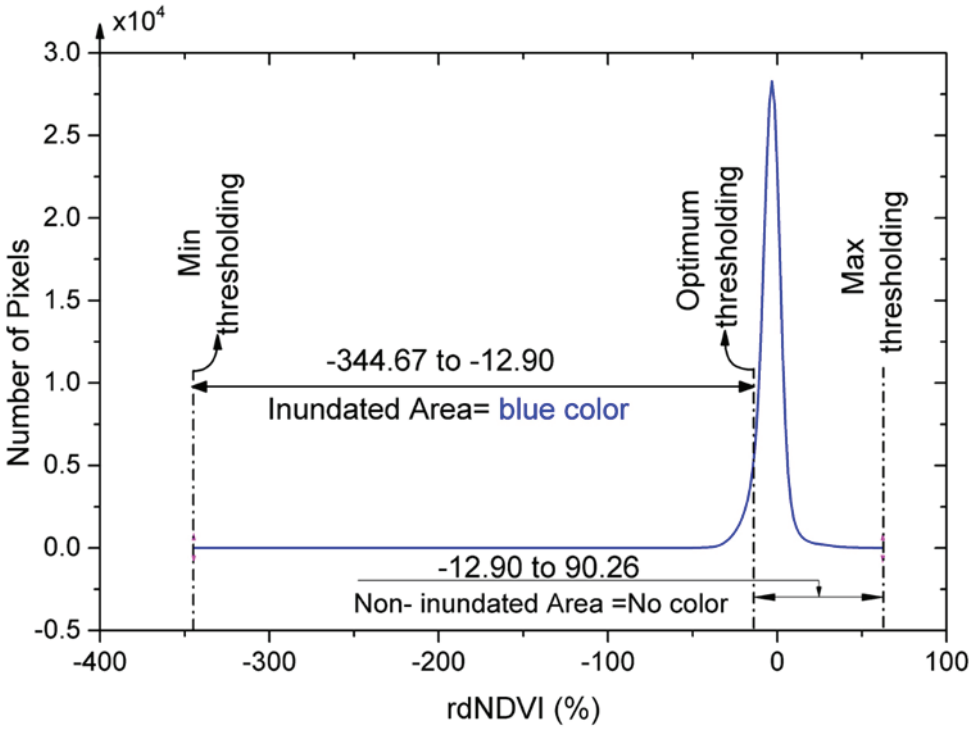

Figure 4-13. Histogram of the rdNDVI image with the chosen thresholds.

However, there were falsely detected areas due to the existence of a sharp slope that reflected as a shadow. Hence, those undesired noise are canceled out using sieve analysis. Additionally, wrongly detected spots caused by steep slopes (greater than 30 degrees) are masked out. To undertake an error assessment, it was necessary to first simplify the representation of the flooded image into an easily recognizable map. As presented in Fig.4-13, this study used a histogram-based thresholding technique as explained in the methodology to find a set of thresholds that can discriminate between pixels that are inundated and pixels that are in the background. Figure 4-13 presents the histogram of the rdNDVI image with the minimum, optimum, and maximum thresholding. The image is segmented based on the optimum thresholding of -12.90 into two different colors. The optimum value was obtained manually by iterating the value and observing the result. This process was repeated until it is

noticed that, with the selected value, the image contained nearly all of the pixels from the original image. For values less than the optimal value, the color blue is selected to indicate the flooded area. Values larger than optimum thresholding were segmented into a non-inundated area which is presented in white or non-color. The result of binarization is illustrated in Fig. 4-14 (a), which only consists of two classes of inundated and non-inundated zones. However, the result of threshold binarization contains unwanted salt-and-pepper noise. As illustrated in Figure 4-14(b), the so-called undesired noises with a size of 10 or less than 10 pixels are masked out. All noises with small areas were canceled out using the Sieve analysis in ENVI 5.3 software, as shown in Fig. 4-14 (b).

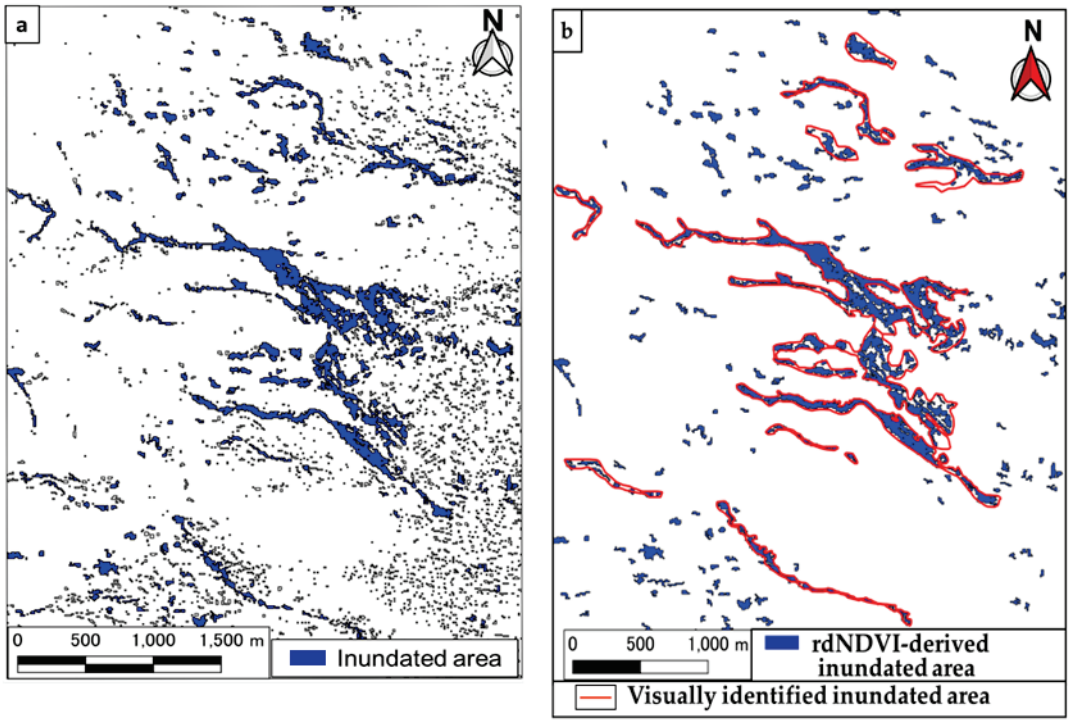

Figure 4-14. Extraction of inundated and non-inundated areas from the rdNDVI result based on binarization for two thresholds. a) The left image presents the result of threshold binarization with unwanted salt-and-pepper noise. b) In the left image, the right image presents the inundated area (red lines) is superimposed on the result of theextracted image of the threshold-binarization after removing salt-and-pepper noise.

Figure 104-14 (b) shows the final inundation map of Charikar, which occurred on August 26, 2020. A total of 300 hectares of built-up area were extracted as inundations.

4.7. Inundation map by visual interpretation

To draw the true inundation of Charikar, this study collected the reports published mainly in the local language by the Disaster Management Authority, the National Statistic and Information Authority (NSIA) (HashtiSubh, 2020), and the National Water Affairs Regulation Authority. Moreover, the pre- and post-event satellite images are side by side compared to identify the changes between the flood events. The Sentinel-2 satellite images acquired before the event (Aug. 24, 2020) and after the event (Sep. 13, 2020) are used as reference data.

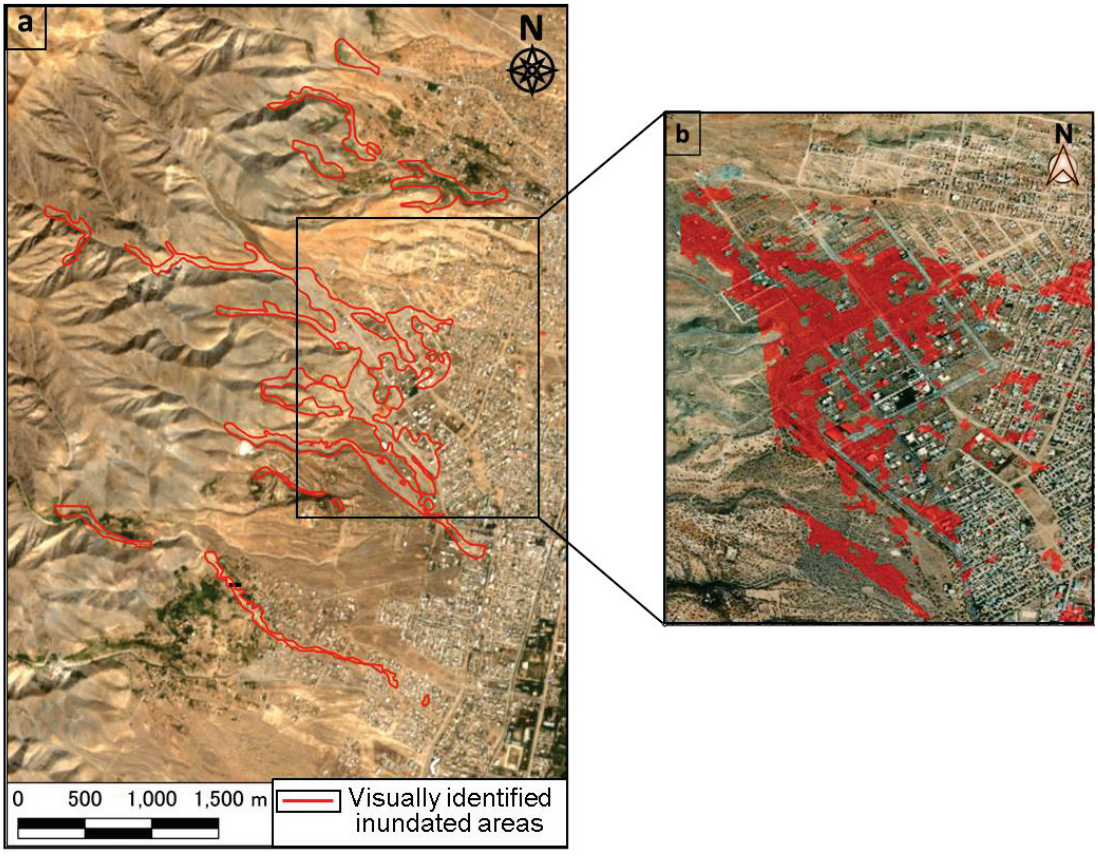

Figure 4-15. Visual interpretation of the flood inundated area. a) Drawn from visual interpretation with government reports, b) Inundation area mapped by (IWMI, 2020).

The true Charikar inundated vector data is overlaid in red color, which is similar to the true impacted site. Because of the resolution of the satellite images, only significant changes were considered. Therefore, minor damage may not be visible, and it was neglected in this study. Although the inundation area by the Charikar flood was also estimated by visual interpretation in a previous study (IWMI, 2020), the interpreted area was limited. This study estimates the inundation map over a larger area. In the process of visual interpretation, the previous inundation map created by IWMI (2020), and official reports are examined. The official reports by the government were reflected in the inundation map. For example, when building damage was reported in some towns in the official documents, inundation areas were identified in the town by the visual interpretations. Figure 4-5 (a) presents the result of visual interpretation carried out in this study. Figure 4-5 (b) shows the result of the previous inundation map in (IWMI, 2020). Based on the visual comparison of the images, it can be confirmed that the inundated area obtained in this study has good agreement with the previous visual interpretation.

4.8. Accuracy assessment

The accuracy assessment of the results obtained in this study was made through a confusion matrix explained in the methodology. The result of the rdNDVI-based change detection shown in Fig. 4-14(b) is overlaid on the visually identified inundation map shown in Fig. 4-15(a). The error assessment was conducted pixel-by-pixel based on the confusion matrix. The result of the confusion matrix is presented in Table 4-2. It presents the user's accuracy, the producer's accuracy, the overall accuracy, and the Kappa coefficient. The accuracy assessment obtained from the analysis of this study shows an overall accuracy of 88.44 % with a Kappa coefficient of 0.75, which indicates a good agreement between thematic maps generated from images and the reference data.

Based on the inundated map obtained in this study, most of the affected houses were in built-up areas, and it was also confirmed by government reports. Another significant point of this method is the ability to detect changes with a single post image. Increasing the number of post-event images does not increase the quality of the detected image. Therefore, the rdNDVI algorithm has the potential to quickly identify the flood-affected area immediately after an event on a routine basis, typically with comparable accuracy to on-site reports, to help decision makers find a quick way to contribute significantly to the post-disaster activities.

Table 4-2. Accuracy assessment result using the confusion matrix**.**

		Actual change status			User's accuracy (%)	Producer's accuracy (%)
	Classes	Inundated (Pixels)	Non-inundated (Pixels)	Row total (Pixels)		
Modeled change status	Inundated	2,323	524	2,847	81.59	88.23
	Non-inundated	310	4057	4,367	92.9	88.56
	Column total	2,633	4581	7,214	Overall accuracy	88.44
					Kappa Coefficient	0.75

4.9. Monitoring the changes in the affected area in two years

The spatial resolution of remote sensing data accessible to state, local, and regional agencies has markedly improved. It is very helpful for the public sector and local governments to consider the use of new remote sensing technologies to monitor and efficiently act based on needs. The use of satellite data and remote sensing applications already brings significant efficiency to the decision-makers and policymakers of developed countries. However, developing countries such as Afghanistan do not have the technical capacity to use remote sensing data and applications for post-disaster activities. In most cases, even having information about the affected area, the government does not reach out to the people to help them in the recovery process.

From the NDVI time series (Figure 4-16) in the affected region depicted by the rectangle in Figures (4-5) - (4-8), it can be seen that the NDVI decreased following the Charikar event. As can be seen, even after one year, the NDVI values did not recover. This study illustrates the rdNDVI changes one year after the event in Fig. 4-17. The rdNDVI image time series shows very minor and negligible changes, indicating that the damaged area has not yet recovered considerably. Probably one factor behind the lack of changes in the NDVIs is the limitation of economic and human resources in the Afghanistan government, which they failed to utilize to revitalize and rebuild the affected areas. People also could not rebuild their houses, probably due to their poverty. This result shows that the NDVI and rdNDVI techniques are very useful for monitoring the event, and it will particularly be useful to observe how long it will take for the recovery of the affected area.

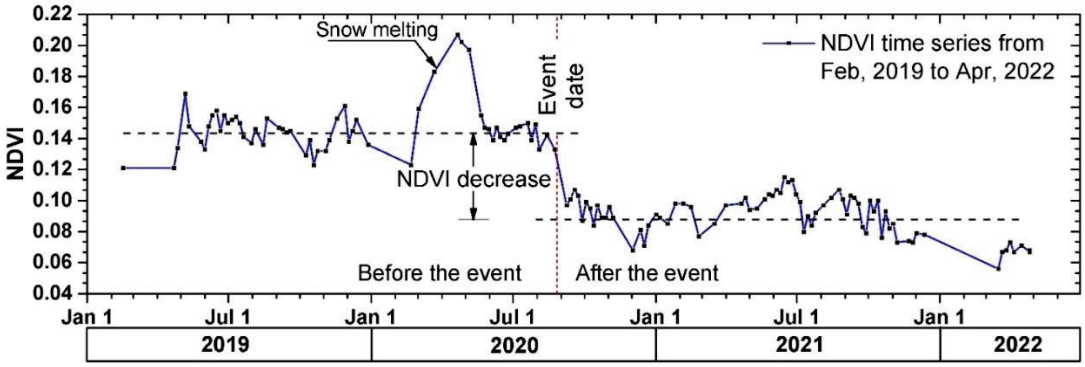

Figure 4-16. NDVI time series over the study area; the blue line indicates the raw NDVI from Feb. 2019 to Apr. 2022.

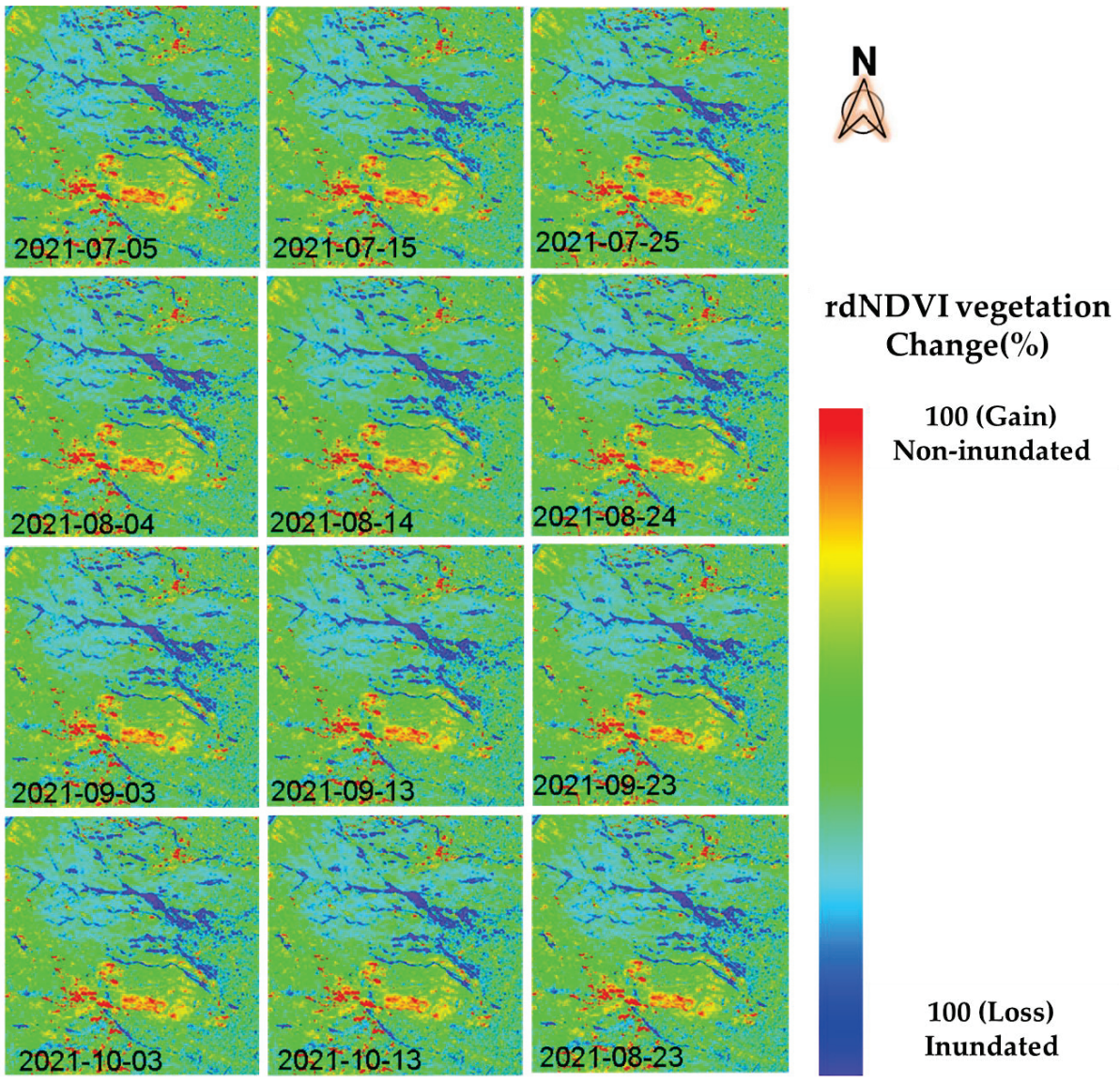

Figure 4-17. rdNDVI changes in Charikar after one year period.

4.10. Flow propagation analysis by Flow-R

The freely available ASTER-GDTM with 30 m spatial resolution was used in the simulation of the Charikar flood event. The initial pixels of the detected inundated areas in the mountains were selected as the predefined source points. The parameters for flow spreading in Flow-R were provided as shown in Table 4-3.

Table 4-3. Debris-flood parameters used in Flow-R.

Types of input	Flow-R Parameters	Value
Directions algorithm	Holmgren (1994 modified)	Dh=2, exponent=4
Inertial algorithm	Weights	Default
Friction loss function	Travel angle	4, 5, 6 Degrees
Energy limitation	Velocity	15 m/sec

These parameters were also used in the evaluation of the debris flow events in Hiroshima prefecture, Japan in July 2018 (Miura, 2019). Three different travel angle iterations for the analysis, as illustrated in Table 4-3 are considered, because the threshold of the travel angle largely controls the propagation areas. The result of each iteration is shown in Fig. 4-18. The overlaid red lines are the visually identified inundation maps. The results show the estimated spreading areas well reproduced the inundation areas by the flood. It is noticed that smaller travel angles such as 4 degrees overestimated the inundation areas as shown in Fig. 4-18 (a), and larger travel angles such as 6 degrees underestimated the flood inundation areas (Fig. 4-18 (c)). The result with a travel angle of 5 degrees shown in Fig. 4-18 (b) gave moderate spreading areas. Figure 4-18 (b) depicts a spread region that is slightly bigger than the inundation areas that were determined, but the simulation that used a travel angle of 5 degrees was able to better reproduce these inundation areas. These results indicate that hazardous areas

for future flood events can be evaluated if appropriate source points are provided in the simulation. Such simulations would be useful not only for government officials but also for residents living in natural hazard susceptible areas, particularly flood and debris flow prone areas, to increase their awareness of mitigating future disasters.

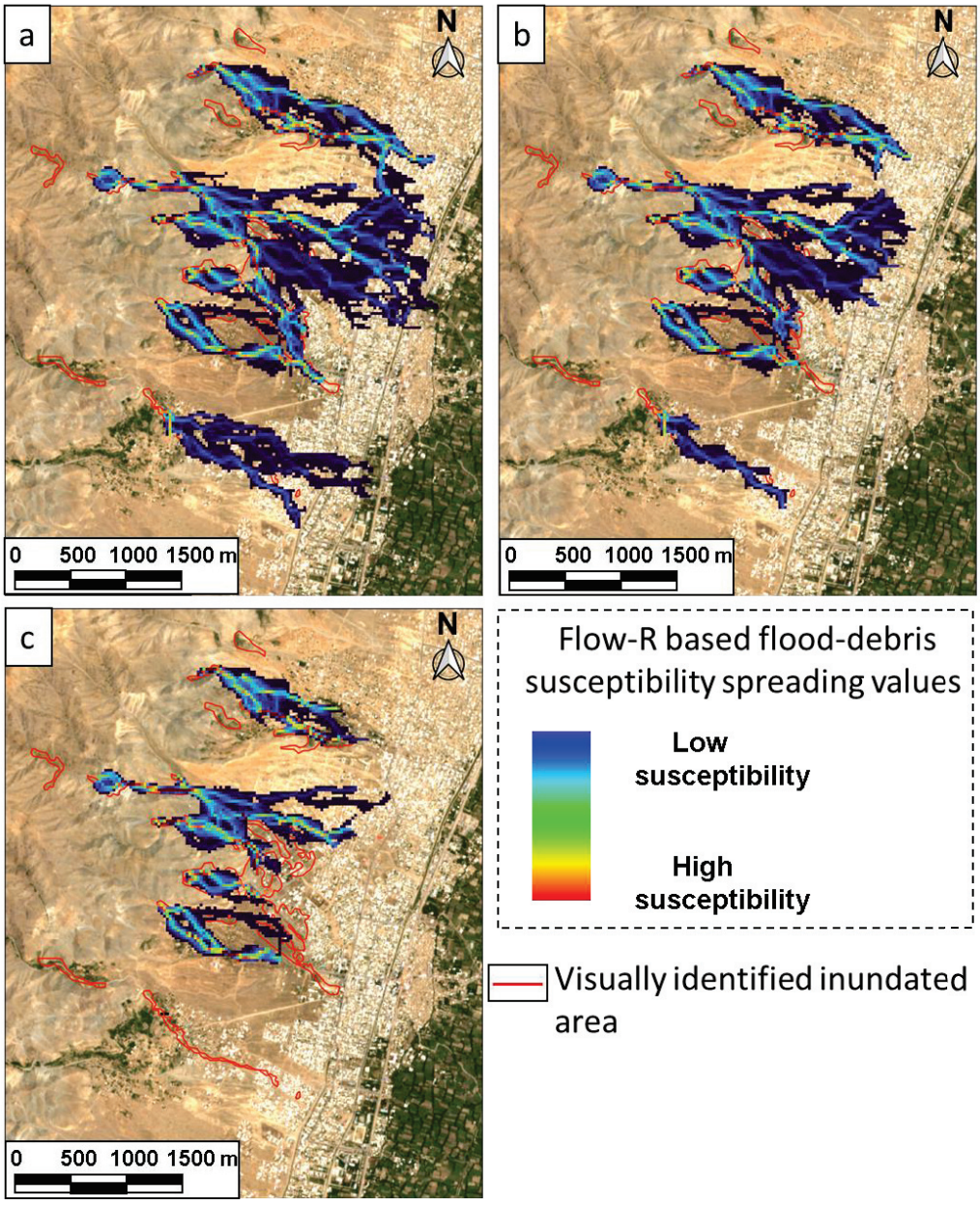

Figure 4-18. Flow-R generated flood -debris susceptibility map using a 4-degree travel angle illustrated in (a), 5-degree travel angle in (b), and 6-degree travel angle in (c).

4.11. Significance of the method

The novel aspect of this study is the combination of pre- and post-greenest pixel compositing with the Google Earth Engine service in order to map hazard-related changes in the vegetated and non-vegetated areas, as well as flat areas, mountainous areas, and areas with a high concentration of buildings. This work is also an attempt to bridge the gap between the worlds of cloud computing and big data, which enables extremely large satellite datasets to be processed quickly in response to a crisis. On the other hand, government agencies and the general public could benefit from the current method even though they lack the expertise to do so directly through the Google Earth Engine utilizing the rdNVI to monitor changes in the vegetation. Schiep et al., 2021, utilized the rdNVI to monitor changes in the vegetation; However, those researchers did not investigate the usefulness of the system in identifying landslides, particularly in areas that were devoid of vegetation. In contrast to the previous research Schiep et al., 2021, which proposed using the method in vegetated regions, this study successfully applied and map the inundated area by using the rdNDVI approach in a dry environment without any vegetation. In addition, the accuracy of the rdNDVI methodology was not investigated in the previous research; however, in this work, the accuracy of the method is also discussed.

The use of this study in a place with little data, less research, and significant security challenges would be an additional contribution that would be of use for government and volunteer organizations. Another important part of the current study is its applicability in a flood-prone area with no standing water when the satellite is passing. There are numerous methods for extracting water body using spectral water index such as NDWI (McFeeters 1996; Rogers et al., 2004), MNDWI (Xu, 2006), AWEI (Feyisa et al., 2014), EWI (Wang et al., 2014), NDMI (Zha et al., 2003) and NDBI (Gao, 1996). However, none of these techniques

acknowledged their application in detection of inundated areas with no standing water. Although it is conceivable to detect the inundated area in a completely identical scenario such as Charikar city using some of the water spectral indices, but no research has been conducted in this regard using the so-called indices.

4.12. Urban planners and flood managers' expectations from current study

Rapid urbanization poses a serious threat to existing flood management infrastructure, putting lives and property at risk if it is not appropriately planned. Rivers, coastal floods, pluvial and groundwater floods, and manmade system failures can all cause flooding in urban areas. Lands with open soil that can be used for water storage are scarce in metropolitan settings. Flooding can occur when rainfall intensity is high and drainage systems do not have the ability to handle the flow. Constant urbanization has diminished the permeability of the soil in groundwater recharge zones, resulting in increased runoff and a higher risk of flooding. To avoid catastrophic disasters, it is critical to take preventative and precautionary measures while dealing with flood threats. As (Abdrabo et al., 2022) suggested, Flood Risk Assessment (FRA) is intended to improve disaster management efficiency, decrease the terrible social and economic effects of flooding, and direct urban growth to a safe place. As a result, FRA is critical for detecting flood-prone locations in arid urban contexts, reducing flood risks, and assisting in decision-making. (Abdrabo et al., 2022; Amundrud et al., 2015).

Both structural and non-structural flood control measures must be undertaken to reduce current and future flood damage. The structural measures are engineering works that can be undertaken to remedy and/or prevent flood-related problems. Non-structural measures are those that aim to prevent or decrease flood damage or effects by introducing rules, regulations, and programs aimed at, for example, regulating land use and occupation, implementing warning systems, and raising public awareness.

This approach will significantly contribute to the rapid detection of inundated areas using a single publicly available satellite image, such as Sentinel-2. The GEE is utilized for the analysis in order to speed the operation. Rapid identification of the inundated area expedites the post-crisis management of rescuing the affected individuals, offering additional essential aid, and assisting the people in rebuilding and reconstructing the affected areas. Afghanistan's government lacks the capacity to develop crisis maps quickly after an occurrence. The results of this study and the provision of such results can inspire the government to prioritize remotely sensed data for crisis management in the future. In addition, in this study, the detection of possible future flood utilizing Flow-R is also discussed. If future flood zones are identified, urban planners, policy makers, and flood operators on the ground will be better equipped to mitigate risks by taking the appropriate countermeasures, such as structural and non-structural measures. In addition, whether contemplating the formation of new cities or formulating plans for existing ones, it is strongly recommended that the Flow-R software be used to analyze the likelihood of future flooding. It is also important to note that local and central government must ensure that no new homes are constructed in high-risk regions. For existing settlements in flood-prone areas, the government must either replace homes with safer alternatives or implement structural measures such as detention/ retention facilities, channel improvements to reduce the impact of flooding in flood-hazard areas, construction of banks or dams, upstream storage and diversion works.

According to the results of the present study, the damaged area has not recovered even two years later. It is evident that the government is inadequate in terms of monitoring and offering assistance. The government will be able to monitor the damaged area and provide better aid to the affected area using the current method's results and applications. Last but not least, the outcome of transferring the current study's skills will be an improvement in government and officials' awareness.

4.13. Applications and future aspects

This section discusses the applications and future aspects of remote sensing technology for detecting and monitoring areas affected by natural disasters. The workflow can be easily applied to different areas, such as built-up areas, vegetated and non-vegetated areas. Moreover, it can be used in different flood scenarios, such as flash floods, coastal floods, fluvial, and pluvial floods. Unlike any traditional method, the GEE used in this study automatically gives the flood-affected area with little processing time after giving the area of interest and the concerning event date. It is also worth noting that the current method can quickly identify a flooded area with significant time efficiency in terms of disaster support management for affected people. In addition, most traditional methods of identifying flood-affected areas in urban, densely vegetated, or non-vegetated areas are challenging. In most cases, the download and preprocessing of images add extra time to the analysis process. However, the current method can determine the inundated area in the mentioned areas with considerable speed without the existence of the mentioned challenges in traditional methods. The GEE allows for rapid deployment of the algorithm during flood events and gives the user extra time to not download the numerous temporal images.

Many false positive pixel changes on the land surface in the inundated images also noticed, which were mostly not caused by flooding. Most of the false-positive pixels detection was due to the sharp slope, which makes the pixels in those areas darker and, as a result, falsely leads the algorithm to detect those areas as a flood. To prevent the detection of such false positive pixels the sharp slope is masked out in the analyses. The current method is not able to capture the flood peak due to the acquisition frequency of Sentinel-2 or most of the time due to the clouds. However, the recent increase in launches of satellites with optical sensors will allow users immediate data acquisition just after a natural disaster. Moreover, the shortcoming

addressed here may need further research to find a possible way of automatically denoising the rdNDVI result to accomplish the analysis faster.

4.14. Summary of this chapter

Due to the recent increase in the frequency and magnitude of natural hazards such as flooding events, satellite remote sensing has become more valuable for post-disaster activities. This study presented utilizing the rdNDVI in GEE using Sentinel-2 images to detect and estimate the flood-affected area. The technique presented in this study was employed in a flood disaster that occurred on Aug 26, 2020, in Charikar, Afghanistan. The method successfully detected the flood-affected area with only one post-event image which is significant time efficient in terms of disaster support management for the affected people. An increasing number of post-event images does not significantly improve the quality of the estimated inundation map. Moreover, it is being stressed that the method can successfully be used even in non-vegetated areas such as semi-arid regions like Charikar to quickly identify affected areas.

The sharp slope of the mountain caused false positive pixels changes on the land surface in the inundated images which makes the pixels on those areas darker and as a result falsely leads the algorithm to detect those areas as a flood. The most flood-affected area was in the built-up area, which also can be confirmed by government survey reports. Accuracy assessment was carried out to verify and assess the accuracy of the inundated map. The accuracy assessment obtained from the analysis of this study showed an overall accuracy of 88 % with a Kappa coefficient of 0.75, which indicates a good agreement between thematic maps generated by the visual interpretation. Even after two years, there is no noticeable increase in NDVI values in the study area, indicating that the damaged areas have not recovered due to the government's lack of financial and human resources and the poverty of the affected population. Further, the Flow-R simulation is utilized to discuss the applicability of the technique in assessing flood areas for a probable future flood event. The inundated map obtained from the Flow-R was also comparable with the identified inundation areas.

Estimations of flooded areas serve as important input information used for determining the extent of natural disasters and for making decisions regarding the recovery plans for the damaged areas. The total flood-affected area using the current method was approximately estimated at 300 ha. With this, it can be concluded that the method utilized in this study has a considerable potential to map the inundated area rapidly in both flat and mountainous regions, and it indicates good applicability of this technique. With that being said, it suggests that this method can be used efficiently even with the viability of one single post-event image on a routine basis and runs whenever a new flood event has occurred.

CHAPTER V

CONCLUSIONS

This dissertation overviewed five major natural disaster and it finally utilize remote sensing analysis to detect, monitor, and predict the landslide and flood which are the leading cause of hundreds of life's losses in Afghanistan. Besides the detection of the mentioned natural disaster, the extent of the landslide, such as volume, depths of erosion, and depositions is also estimated. To accomplish the objective of this study, two different methodologies is used. For landslide detection and assessments, nonlinear mapping techniques is employed. However, for flood detection and assessment, the rdNDVI techniques is utilized. The nonlinear mapping techniques is used for landslides because of lack high resolution stereo satellite imagery in the study area where the landslides happened. As a result, in the flood-affected area, similar data could not be obtained. Applying nonlinear mapping techniques is solely dependent on the availability of stereo types of satellite imagery. The availability of such high-resolution satellite imagery give user the opportunity to not only detect and assess the changes in the area but also estimate the volume and depth of those changes with high accuracy. On the contrary, the rdNDVI can detect both landslides and floods in any type of land area rapidly by using freely available satellite imagery. Although rdNDVI satellite imagery can be used to detect and assess nearly all types of natural disaster, it cannot be used to estimate the volume and depth of changes.

This dissertation initially discusses the details of the natural disaster risk such as earthquakes, floods, landslides, avalanches, and droughts in Afghanistan. The availability of risk information is a key to the effective management of disaster and climate risks. The risk profile provides a summary and visualization of the national multi-hazard assessments. Such

information will provide essential data and information for policymakers, decision-makers, development planners, and infrastructure investors to ensure a more resilient future for people in Afghanistan. Therefore, this study discussed the susceptibility map, lack of coping capacities, lack of adaptive capacities, vulnerability map, exposure of the population to natural hazards, and world risk index as a result of exposure and vulnerability. This study also present which natural disaster is worse in terms of agricultural losses, property losses, and deaths.

The nonlinear mapping technique is utilized to detect and estimate the volume of the landslide affected area using stereo-paired high-resolution satellite imagery. It is being stressed that the method can successfully be used in the image processing analysis to conduct mapping tasks, diminishing the geometric errors accumulating in the unchanged areas of the DoDs output, and finally, obtain the volume and average depth of the displaced material in the disaster area to ease the crisis management support and contribute very well to the more effective planning of disaster relief and restoration.

The technique presented in this study was employed in a large-scale landslide that occurred on May 2, 2014, in Abe-Barek village, Badakhshan, Afghanistan. Using the DEMs of the difference change detection technique, the DEMs of landslide affected areas are generated from the pre-and post-event satellite stereo-pair images. Although the DEMs were corrected using the RPC method, registration noises or locational errors were still spotted in the nonaffected areas. The nonlinear mapping technique was utilized to diminish the aforesaid geometric inconsistencies or registration noises and enhance the accuracy of the process analysis. The proposed method has been coded in such a way that, in the selected testing zone with the given combinations of parameters, the post-event DEM (follower data), superimposes on the pre-event DEM, and pixel by pixel, scans neighboring vicinities for the best possible matching points in the pre-event DEM (controller data). In this study, nine scenarios were examined with different values of NW (window size or size of the subarea), NS (search area),

NC (consensus area), and n (number of iterations). As the quantitative and graphical comparison revealed, the locational gaps were significantly reduced, and a bell-shaped histogram, also known as a normal distribution, was obtained. Moreover, statistical values, in particular, mean and standard deviations, decreased more towards zero and one, respectively. Additionally, the obtained RMSE values also verified the nonlinear mapping's applicability in decreasing the locational errors quantitatively. After carefully comparing and observing the assessments, $N_W = 5$, $N_S = 9$, $N_C = 3$, and $n = 3$; were chosen as the required inputs for the method to use for the rest of analysis.

The total eroded soil volume in the landslide area after adopting the nonlinear mapping method was approximately estimated at about 1.05×10^6 m^3, and the volume of the deposited soil acquired was 6.73×10^5 m^3. The landslide's estimated volume was compared with the volumes obtained from the previous studies. The erosion volume of the soil obtained in this study showed good agreement with that achieved in the previous studies. The average depth of erosion, mostly situated on the mountain's hilly side, was 8.6 m. On the contrary, the average depth of deposition, which is typically situated in a flat area, was estimated at 4.6 m. This highlights that nonlinear mapping has a considerable potential to reduce locational errors in mountainous regions. Therefore, it indicates a good applicability of the nonlinear mapping technique. It suggests that the method can be used efficiently on a routine basis and run whenever a new landslide event has occurred if high-resolution stereo-pair images of the area become available.

Chapter four of current study presents This study explored the usefulness of the rdNDVI approach in Sentinel-2 images for estimating flood inundation areas in a semi - arid and arid region by employing the GEE. The approach of this investigation was applied to the flash flood incident in Charikar, Afghanistan on August 26, 2020. Several spectral indices, including NDVI, MNDWI, and NDMI, were utilized to detect the flooded areas. A strong relationship

was found between NDVI and MNDWI, and both indices decreased significantly in the affected zones soon following the occurrence of the incident. In contrast, NDMI did not change significantly between before and after the event. From the perspective of spatial resolution, it is determined that NDVI should be used to detect flooding zones. The NDVI was effective in defining flood inundation regions in a semi - arid and arid region, which is one of the most noteworthy findings of this study. The method successfully detected the flood-affected area with only one post-event image, which is significantly time-efficient in terms of disaster support management for the affected people. An increasing number of post-event images does not significantly improve the quality of the estimated inundation map. Moreover, it is being stressed that the method can be successfully used even in non-vegetated areas such as semi-arid regions like Charikar to quickly identify affected areas.

The sharp slope of the mountain caused false positive pixels on the land surface in the inundated images, which made the pixels in those areas darker and, as a result, falsely led the algorithm to detect those areas as a flood. The most flood-affected area was in the built-up area, which can also be confirmed by government survey reports. An accuracy assessment was carried out to verify and assess the accuracy of the inundated map. The accuracy assessment obtained from the analysis of this study showed an overall accuracy of 88% with a Kappa coefficient of 0.75, which indicates a good agreement between thematic maps generated by the visual interpretation. No significant increase in NDVIs value in the study area is observed even after two years, indicating that the affected areas have not recovered, probably due to the government's lack of financial and human resources and the poverty of the affected people. Furthermore, the Flow-R simulation is utilized to discuss the applicability of the technique in assessing flood areas for a probable future flood event. The inundated map from the Flow-R was also to some extent similar to the inundated areas that had already been found.

Estimations of flooded areas serve as important input information used for determining the extent of natural disasters and for making decisions regarding the recovery plans for the damaged areas. The total flood-affected area using the current method was approximately 300 ha. With this, it can conclude the method utilized in this study has considerable potential to map the inundated area rapidly in both flat and mountainous regions, and it indicates good applicability of this technique. Finally, it is suggested that this method can be used efficiently with the viability of one single post-event image on a routine basis and run whenever a new flood event has occurred.

The error estimation has not been discussed in landslide assessments using actual GCPs. Once such data are collected, much additional work needs to be done. For example, an error estimation of both depths and volume obtained from the nonlinear mapping and real GCP can be compared using the evaluation change analysis technique. Most of the false-positive pixels detection in flood detected area was due to the sharp slope, which makes the pixels in those areas darker and, as a result, falsely leads the algorithm to detect those areas as a flood, a manual denoising method was applied in this study. Moreover, the proposed rdNDVI technique is not able to capture the flood peak due to the acquisition frequency of Sentinel-2 or most of the time due to the cloud's coverage. So further research needs to be done to find a possible way of automatically denoising the rdNDVI result to accomplish the analysis faster.

As a final remark it is to say that the approaches based on satellite imagery and/or DEM would be advantageous for pre- and post-disaster efforts, particularly for countries with limited financial and human resources, such as Afghanistan. Implementation of remote sensing technologies, including the proposed method in this work, by the government and official agencies would be crucial for more prompt and effective responses to future natural disasters and for the development of effective remedies.

References

Abdrabo, K.I. et al. The Role of Urban Planning and Landscape Tools Concerning Flash Flood Risk Reduction Within Arid and Semiarid Regions. In: Sumi, T., Kantoush, S.A., Saber, M. (eds) Wadi Flash Floods. Natural Disaster Science and Mitigation Engineering: DPRI reports. Springer, 2022., Singapore. https://doi.org/10.1007/978-981-16-2904-4_11.

Abdullah-Al-Wadud, M.; Kabir, M.H.; Dewan, M.A.A.; Chae, O. A Dynamic Histogram Equalization for Image Contrast Enhancement. IEEE Trans. Consum. Electron. 2007, 53, 593–600.

Abele, G. Bergsturze in den Alpen– Ihre Verbreitung, Morphologie und Folgeerscheinungen, Wissenschaftliche Alpenvereinshefte: Mu¨nchen, Germany, 1974; Volume 25; 247p. (In Germany)

Afghanistan-MHRS, 2017, Afghanistan—Multi-hazard risk assessment. Washington, DC: World Bank. Available online at: https://www.gfdrr.org/sites/default/files/publication/Afghanistan_MHRA.pdf.(Accessed on Jul 01, 2022).

Agisoft. Metashape. Available online: https://www.agisoft.com/ (accessed on 4 December 2020).

Ahmed, A. More Than 2000 Feared Dead in Landslides. The New York Times. 2014. Available online: https://www.nytimes.com/2014/05/04/world/asia/aid-effort-begins-at-scene-of-afghan-landslides.html (accessed on 25 October 2020).

Amundrud, Ø.; Aven, T., On how to understand and acknowledge risk. Reliab. Eng. Syst. Saf. 2015, 142, 42–47. https://doi.org/10.1016/j.ress.2015.04.021 .

Asokan, A.; Anitha, J. Change detection techniques for remote sensing applications: a survey. Earth Sci Inform 2019, 12, 143-160.

Atefi, M. R.; Miura, H. Volumetric analysis of the landslide in Abe Barek, Afghanistan based on nonlinear mapping of stereo satellite imagery - derived DEMs. Remote Sens. 2021, 13, 446. https://doi.org/10.3390/rs13030446.

Azadmanish, O. A general view of a building in Charikar covered with flooded debris of flooding in Parwan, 26 Aug 2020, Reuters, https://www.thestar.com.my/news/world/2020/08/26/flash-floods-kill-more-than-70-in-afghanistan, (Accessed on March 10, 2022)

BBC, 2017: Afghanistan and Pakistan avalanches kill more than 100 in Feb 2017. Accessed online at: https://www.bbc.com/news/world-asia-38872941. (Accessed on July 1 2022).

Boyd, O. S., Mueller, C. S., & Rukstales, K. S. (2007). Preliminary earthquake hazard map of Afghanistan. Open-File Report (United States Geological Survey. 1978.

Brunetti, M.T.; Guzzetti, F.; Rossi, M. Probability distributions of landslide volumes. Nonlinear Process Geophys 2009, 16, 179-188.

Caballero, I.; Ruiz, J.; Navarro, G. Sentinel-2 satellites provide near-real time evaluation of catastrophic floods in the west Mediterranean. Water 2019, 11(12), 2499, https://doi.org/10.3390/w11122499.

Campos-Taberner, M.; García-Haro, F. J.; Martínez, B.; Izquierdo-Verdiguier, E.; Atzberger, C.; Camps-Valls, G.; Gilabert, M. A. Understanding deep learning in land use classification based on Sentinel-2 time series. Sci. Rep. 2020, 10(1), 17188-17188, https://doi.org/10.1038/s41598-020-74215-5.

Chen, S.; Chen, C.; Huang, W. Exploring landslide erosion volume–area scaling relationships by slip depth using changes in DTMs for basin sediment volume estimation. J. Mt. Sci 2019, 16, 581-594.

Chen, Z.; Zhang, B.; Han, Y.; Zuo, Z.; Zhang, X. Modeling accumulated volume of landslides using remote sensing and DTM data. Remote Sens., 2014, 6, 1514-1537.

Dai, F.C.; Lee, C.F.; Ngai, Y.Y. Landslide risk assessment and management: an overview. Engineering Geology 2002, 64, 65-87, https://doi.org/10.1016/S0013-7952(01)00093-X.

Davranche, A., G. Lefebvre, B. Poulin. Wetland monitoring using classification trees and SPOT-5 seasonal time series a. Remote Sens. Environ, 2010, 114, pp. 552-562.

DeVries, B.; Huang, C.; Armston, J.; Huang, W.; Jones, J. W.; Lang, M. W. Rapid and robust monitoring of flood events using Sentinel-1 and Landsat data on the Google Earth Engine. Remote Sens. Environ. 2020, 240, 111664. https://doi.org/10.1016/j.rse.2020.111664.

Dinh, D. A.; Elmahrad, B.; Leinenkugel, P.; Newton, A. Time series of flood mapping in the Mekong delta using high resolution satellite images. IOP Conf. Ser. Earth Environ. Sci. 2019, 266(1), 12011. https://doi.org/10.1088/1755-1315/266/1/01201.

Duan, Z., Bastiaanssen, W.G.M. Estimating water volume variations in lakes and reservoirs from four operational satellite altimetry databases and satellite imagery data. Remote Sens. Environ, 2013, 134, pp. 403-416.

Dupree, Louis, Petrov, Victor P., Allchin, Frank Raymond, Ali Mohammad , Weinbaum, Marvin G. and Dupree, Nancy Hatch. "Afghanistan". Encyclopedia Britannica, 2 Nov. 2021, https://www.britannica.com/place/Afghanistan. Accessed 4 May 2022.

Emma, G. Afghanistan Mudslides: Hundreds Feared Dead. The Guardian. 2014. Available online: https://www.theguardian.com/world/2014/may/02/afghanistan-landslide-badakhshan-leaves-thousand-missing (accessed on 27 October 2020).

Ermini, L.; Catani, F.; Casagli, N. Artificial neural networks applied to landslide susceptibility assessment. Geomorphology 2005, 66, 327-343.

Escuin, S; Navarro, R.; Fernández, P. Fire severity assessment by using NBR (normalized burn ratio) and NDVI (normalized difference vegetation index) derived from LANDSAT TM/ETM images. Int. J. Remote Sens. 2008, 29(4), 1053-1073. https://doi.org/10.1080/01431160701281072.

European Space Agency (ESA). Sentinel-2 User Handbook', ESA Standard Doc 2015, 24/07/2015 Issue 1 Rev 2.

Fauvel, M.; Chanussot, J.; Benediktsson, J.A. Kernel principal component analysis for the classification of hyperspectral remote sensing data over urban areas. EURASIP J Adv Signal Processg. 2009, 2009, 1-14.

Feyisa, G. L., Meilby, H., Fensholt, R., & Proud, S. R. Automated water extraction index: A new technique for surface water mapping using Landsat imagery. Remote Sens. Environ. 2014, 140(0), 23–35. https://doi.org/10.1016/j.rse.2013.08.029.

Fonseca, L.M.G.; Manjunath, B.S. Registration techniques for multisensor remotely sensed imagery. Photogramm. Engr. Remote Sens. 1996, 62, 1049–1056.

Freebairn. A; Turmine. V; Singh. R. Climate as a risk multiplier-trends in vulnerability and exposure, World Disasters Report 2020 Come Heat or High Water, edited by Hagon, K. 2020, pp. 119-126, Geneva, (IFRC).

Fuchs, S., Keiler, M., & Sokratov, S. (2019). Chapter 15—Snow avalanches. In V. Maggioni & C. Massari (Eds.), Extreme Hydroclimatic Events and Multivariate Hazards in a

Changing Environment (pp. 369–389). Elsevier. https://doi.org/10.1016/B978-0-12-814899-0.00015-8

Gandhi, G.M.; Parthiban, S.; Thummalu, N.; Christy, A. Ndvi: Vegetation change detection using remote sensing and Gis - A case study of Vellore District. Procedia Comput. Sci. 2015, 57, 1199–1210.

Gao, B.C. Ndwi - a normalized difference water index for remote sensing of vegetation liquid water from space. Rem. Sens. Environ. 1996, 58, pp. 257-266

Gibbons, T.; Fahim Abed, N. Nearly 80 killed as flash floods ravage city in Afghanistan. The New York Times, Aug 26, 2020. https://www.nytimes.com/2020/08/26/world/asia/afghanistan-floods-charikar.html (Accessed March 02, 2022).

Glinski, S. Many people are still missing': Afghanistan families devastated by flash floods, Sep 2020, The Guardian, https://www.theguardian.com/world/2020/sep/01/many-people-are-still-missing-afghanistan-flash-floods (Accessed on March 10, 2022)

Gul, R. People walk near damaged houses after the 2020 heavy flooding in the Charikar, Parwan province. Aug 26, 2020. https://www.foxnews.com/world/floods-in-north-east-afghanistan-leave-at-least-100-dead (Accessed on March 10, 2022).

Gul, R. Villagers' soldiers search for victims in a mudslide resulting from a flash flood that affected the area at Sayrah-e-Opiyan in Charikar, 26 Aug 2020, https://www.rferl.org/a/afghanistan-weather-floods/30803355.html. (Accessed on March 10, 2022).

Gupta, M. Afghanistan: National Disaster Management Plan, 2010. National Legislative Bodies / National Authorities, UNDP, 2010. Available online: https://www.preventionweb.net/files/31182_afghanistannationaldisastermanageme-451.pdf (Accessed on November 7, 2020)

Guthrie, R.H.; Evans, S.G. Analysis of landslide frequencies and characteristics in a natural system, coastal British Columbia. Earth Surf. Process. Landf. 2004, 29, 1321–1339.

Guzzetti, F.; Ardizzone, F.; Cardinali, M.; Galli, M.; Reichenbach, P.; Rossi, M. Distribution of landslides in the Upper Tiber River basin, central Italy. Geomorphology 2008, 96, 105–122.

Guzzetti, F.; Ardizzone, F.; Cardinali, M.; Rossi, M.; Valigi, D. Landslide volumes and landslide mobilization rates in Umbria, central Italy. Earth Planet Sci Lett 2009, 279, 222-229.

Haque, U.; Da Silva, P.F.; Devoli, G.; Pilz, J.; Zhao, B.; Khaloua, A.; Wilopo, W.; Andersen, P.; Lu, P.; Lee, J.; Yamamoto, T.; Keellings, D.; Wu, J.; Glass, G.E. The human cost of global warming: Deadly landslides and their triggers (1995–2014). Sci. Total Environ. 2019, 682, 673-684.

Harp, E.L., Crone, A.J., (2006). Landslides triggered by the October 8, 2005, Pakistan earthquake and associated landslide-dammed reservoirs. U.S. Geological Survey Open-File Report 2006–1052, 10 pp.

HashtiSubh, reports of flood from National Statistics and Information Authority, Aug 31, 2020, https://8am.af/satellite-images-of-the-parwan-flood-nearly-one-thousand-houses-have-been-damaged/ (Accessed on March 9, 2022).

Hirakawa, Y. Optimization of altitude change values for extracting topographical changes by LIDAR. Int. J. Eros. Control Eng. 2006, 58, 18–22. (In Japanese)

Horton, P.; Jaboyedoff, M.; Rudaz, B.; Zimmermann, M. Flow-R, a model for susceptibility mapping of debris flows and other gravitational hazards at a regional scale. Nat. Hazards Earth Syst. Sci. 2013, 13(4), 869-885. https://doi.org/10.5194/nhess-13-869-2013.

Hsieh, Y.; Chan, Y.; Hu, J. Digital Elevation Model Differencing and Error Estimation from Multiple Sources: A Case Study from the Meiyuan Shan Landslide in Taiwan. Remote Sens. 2016, 8, 199.

Huang, C., Chen, Y., Zhang, S., & Wu, J. (2018). Detecting, extracting, and monitoring surface water from space using optical sensors; a review. Rev. Geophys. 2018, (1985), 56(2), 333-360. https://doi.org/10.1029/2018RG000598.

Huete, A. R.; Liu, H. Q.; Batchily, K.; van Leeuwen, W. A comparison of vegetation indices over a global set of TM images for EOS-MODIS. Remote Sens. Environ. 1997, 59(3), 440-451. https://doi.org/10.1016/S0034-4257(96)00112-5.

Hungr, O.; Leroueil, S.; Picarelli, L. The Varnes classification of landslide types, an update. Landslides 2014, 11(2), 167-194. https://doi.org/10.1007/s10346-013-0436-y.

IFRC, (2015), Information bulletin, Afghanistan: Earthquake. Available online at: file:///C:/Users/Mujeeb%20Rahman%20Atefi/Downloads/IBAFeq02102015.pdf. (Accessed on Jul 01, 2022).

Imaizumi, F.; Sidle, R.C.; Kamei, R. Effects of forest harvesting on the occurrence of landslides and debris flows in steep terrain of central Japan. Earth Surf. Process. Landf. 2008, 33, 827–840.

IMMAP-Hagen, (2017), Afghanistan earthquake occurrences, Magnitude and Hazard period 1971-2017. Available online at: https://immap.org/product/afghanistan-earthquake-occurrences-magnitude-and-hazard-1971-2017/. (Accessed on July 1 2022).

Independent Farsi. Flood in Afghanistan killed hundreds in Parwan Province, Aug 26, 2020, https://tinyurl.com/independentpersian (Accessed on March 3, 2022).

Innes, J.N. Lichenometric dating of debris-flow deposits in the Scottish Highlands. Earth Surf. Process. Landf. 1983, 8, 579–588.

International Federation of Red Cross and Red Crescent Societies; Walter, J. World Disasters Report 2001: Focus on Recovery, 2001.

International Water Management Institute (IWMI). Flash flood hit Charikar, Parwan province in Afghanistan (26 Aug 2020), FL-2020-0006-AF version 1.

Jaboyedoff, M.; Oppikofer, T.; Abellán, A.; Derron, M.; Loye, A.; Metzger, R.; Pedrazzini, A. Use of LIDAR in landslide investigations: A review. Nat. Hazards 2012, 61, 5–28.

Jalali, J. Flash flood brought debris and boulders into the house and covered the car and injured and killed the people. 26 Aug 2020, https://www.nytimes.com/2020/08/26/world/asia/afghanistan-floods-charikar.html (Accessed on March 10, 2022).

Jensen, J.R.; Lulla, K. Introductory Digital Image Processing: A Remote Sensing Perspective, Prentice Hall: NJ, United States 2015, 4th ed.; pp. 131–133, ISBN 978-0-13-405816-0.

Khosravi, K.; Shahabi, H.; Pham, B. T.; Adamowski, J.; Shirzadi, A.; Pradhan, B.; Dou, J.; Ly, H.; Gróf, G.; Ho, H. L.; Hong, H.; Chapi, K.; Prakash, I. A comparative assessment of flood susceptibility modeling using multi-criteria decision-making analysis and machine learning methods. J. Hydrol. 2019, 573, 311-323. https://doi.org/10.1016/j.jhydrol.2019.03.073.

Kobayashi, N.; Tani, H.; Wang, X.; Sonobe, R. Crop classification using spectral indices derived from Sentinel-2A imagery. J. Inf. Syst. Telecommun. 2020, 4(1), 67-90, https://doi.org/10.1080/24751839.2019.1694765.

Kosugi, Y.; Sakamoto, M.; Fukunishi, M.; Lu, W.; Doihara, T.; Kakimoto, S. Urban change detection related to earthquakes using an adaptive nonlinear mapping of high-resolution images. IEEE Geosci. Remote Sens. Lett. 2004, 1, 152–156.

Kovács, I.P.; Czigány, S.; Dobre, B.; Fábián, S.Á; Sobucki, M.; Varga, G.; Bugya, T. A field survey-based method to characterize landslide development: a case study at the high bluff of the Danube, south-central Hungary. Landslides, 2019, 16, 1567-1581.

Larsen, I.J.; Montgomery, D.R.; Korup, O. Landslide erosion controlled by hillslope material. Nat. Geosci 2010, 3, 247-251.

Larsen, M.C.; Torres-Sanchez, A.J. The frequency and distribution of recent landslides in three montane tropical regions of Puerto Rico. Geomorphology 1998, 24, 309–331.

Le Moigne, J.; Campbell, W.J.; Cromp, R.F. An automated parallel image registration technique based on the correlation of wavelet features. IEEE Trans. Geosci. Remote Sens. 2002, 40, 1849–1864.

Lei, T.; Zhang, Y.; Lv, Z.; Li, S.; Liu, S.; Nandi, A.K. Landslide inventory mapping from bitemporal images using deep convolutional neural networks. IEEE Geosci. Remote. Sens. Lett. 2019, 16, 982-986.

Lin, M.; Chen, T. Estimating volume of deep-seated landslides and mass transport in Basihlan river basin, Taiwan. Eng. Geol. 2020, 278, 105825.

Malamud, B.D.; Turcotte, D.L.; Guzzetti, F.; Reichenbach, P. Landslides, earthquakes, and erosion, Earth Planet. Sci. Lett. 2004, 229, 45-59.

Martha, T.R.; Kerle, N.; Jetten, V.; van Westen, C.J.; Kumar, K.V. Landslide Volumetric Analysis Using Cartosat-1-Derived DEMs. IEEE Geosci. Remote. Sens. Lett. 2010, 7, 582–586.

Martin, Y.; Rood, K.; Schwab, J.W.; Church, M. Sediment transfer by shallow landsliding in the Queen Charlotte Islands, British Columbia. Can. J. Earth Sci. 2002, 39, 189–205.

Martinez, M.; Basil, Y.; Sediqi, Q. Twin landslides site that killed at least 2000 Afghans declared a mass grave. CNN. 2014. Available online:

https://edition.cnn.com/2014/05/03/world/asia/afghanistan-landslide/index.html (accessed on 22 October 2020).

Mas, J.F.; Flores, J.J. The application of artificial neural networks to the analysis of remotely sensed data. Int. J. Remote Sens. 2008, 29, 617-663.

McFeeters, S. "The Use of the Normalized Difference Water Index (NDWI) in the Delineation of Open Water Feature." Int. J. Remote Sens. 1996, 17 (7): 1425–1432. doi:10.1080/01431169608948714.

Miller, J.D.; Thode, A.E. Quantifying burn severity in a heterogeneous landscape with a relative version of the delta Normalized Burn Ratio (dNBR). Remote Sens. Environ., 2007. 109: 66–80.

Miranda, E.; Mutiara, A.B.; Wibowo, W.C. Classification of land cover from Sentinel-2 imagery using supervised classification technique (preliminary study). In Proceedings of the 2018 International Conference on Information Management and Technology (ICIMTech), Jakarta, Indonesia, 3–5 September 2018, pp. 69–74.

Miura, H. Fusion analysis of optical satellite images and digital elevation model for quantifying volume in debris flow disaster, Remote Sens. 2019, 11(9), 1096, https://doi.org/10.3390/rs11091096.

Miura, H. Soil volume estimation in debris flow areas using lidar data in the 2014 Hiroshima, Japan rainstorm. In Proceedings of the Earth Resources and Environmental Remote Sensing/GIS Applications, VI, Toulouse, France, 22–24 September 2015; The International Society of Optics and Photonics: Bellingham, WA, USA, 2015; Volume VI, p. 96440K.

Muis, S.; Güneralp, B.; Jongman, B.; Aerts, J. C. J. H.; Ward, P. J. Flood risk and adaptation strategies under climate change and urban expansion: A probabilistic analysis using

global data. Sci. Total Environ. 2015, 538, 445-457. https://doi.org/10.1016/j.scitotenv.2015.08.068.

Mutanga, O.; Kumar, L. Google Earth Engine applications. Remote Sens. 2019, 11, 591, https://doi.org/10.3390/rs11050591.

Nadi, S.; Shojaei, D.; Ghiasi, Y. Accuracy Assessment of DEMs in Different Topographic Complexity Based on an Optimum Number of GCP Formulation and Error Propagation Analysis. J. Surv. Eng. 2020, 146, 4019019.

Nakamura, M.; Sakamoto, M.; Kosugi, Y. Stabilizing the accuracy of change detection from geographic images by multi-leveled exploration and selective smoothing, ITE (The Institute of Image Information and Televisions Engineers) Technical Reports: Tokyo, 2002, 27.77, 1-6, doi: https://doi.org/10.11485/itetr.26.77.0_1.

NASA/METI/AIST/Japan Space systems, and U.S./Japan ASTER Science Team. ASTER Global Digital Elevation Model V003. 2018, distributed by NASA EOSDIS Land Processes DAAC, https://doi.org/10.5067/ASTER/ASTGTM.003. (Accessed March 2, 2022)

Norman, S. P and Christie, W. M: Satellite-based evidence of forest stress and decline across the conterminous United States for 2016, 2017, and 2018, Gen. Tech. Rep. SRS-250. Asheville, NC: US Department of Agriculture, Forest Service, Southern Research Station, 2020, 151–166, 2020. a, b.

Norman, S.P.; Koch, F.; Hargrove, W.W. Review of broad-scale drought monitoring of forests: toward an integrated data mining approach, 2016.

Norwegian Refugee Council (NRC): Severe Drought Threatens Three Million Afghans. (2021). Targeted News Service. Accessed from: https://www.nrc.no/news/2021/june/severe-drought-threatens-three-million-afghans/ (Accessed on July, 2022).

OCHA, 2001, Afghanistan facing famine, millions of lives at risk, Available online at: https://reliefweb.int/report/afghanistan/afghanistan-facing-famine-millions-lives-risk. (Accessed on Jul. 01. 2022).

OCHA, 2015, Afghanistan/Pakistan: Earthquake-Oct 2015. Available online at: https://reliefweb.int/disaster/eq-2015-000147-afg. (Accessed on Jul 01, 2022).

OCHA, 2022, Afghanistan: Overview of Natural Disasters (as of 26 June 2022), Natural disaster events from 4 January 2012 to 21 June 2022, accessed online at: https://public.tableau.com/shared/PPS2GPWP8?:showVizHome=no. (Accessed on Jul 1, 2022).

Ostrowski, J.A.; He, D.C. Error Correction of Digital Elevation Models Produced by Automatic Matching of Digital Stereo Images. In Proceedings of the 12th Canadian Symposium on Remote Sensing Geoscience and Remote Sensing Symposium, Vancouver, BC, Canada, 10–14 July 1989; Volume 2, pp. 446–449.

Otsu, N. A threshold selection method from gray-level histograms. IEEE Trans. Syst. Man. Cybern. 1979, 9, 62–66.

Patel, N. N.; Angiuli, E.; Gamba, P.; Gaughan, A.; Lisini, G.; Stevens, F. R.; Tatem, A. J.; Trianni, G. Multitemporal settlement and population mapping from Landsat using Google Earth Engine. Int J Appl Earth Obs Geoinf 2015, 35, 199–208, https://doi.org/10.1016/j.jag.2014.09.005.

Petley, D.N.; Dunning, S.A.; Rosser, N.J. The analysis of global landslide risk through the creation of a database of worldwide landslide fatalities. In Landslide Risk Management; Hungr, O.; Fell, R.; Couture, R.; Eberhardt, E., Eds., CRC Press, 2005, 377-384.

Phongsapan, K.; Chishtie, F.; Poortinga, A.; Bhandari, B.; Meechaiya, C.; Kunlamai, T.; Aung, K. S.; Saah, D.; Anderson, E.; Markert, K.; Markert, A.; Towashiraporn, P.

Operational flood risk index mapping for disaster risk reduction using earth observations and cloud computing technologies: A case study on Myanmar. Front. Environ. Sci 2019, 7, 191, https://doi.org/10.3389/fenvs.2019.00191.

Poortinga, A.; Nguyen, Q.; Tenneson, K.; Troy, A.; Saah, D.; Bhandari, B.; Ellenburg, W. L.; Aekakkararungroj, A.; Ha, L.; Pham, H.; Nguyen, G.; Chishtie, F. Linking earth observations for assessing the food security situation in Vietnam: A landscape approach. Front. Environ. Sci. 2019, 7, 186, https://doi.org/10.3389/fenvs.2019.00186.

Poulin, B., Davranche, A. G. Lefebvre. Ecological assessment of Phragmites australis wetlands using multi-season SPOT-5 scenes, Remote Sens. Environ., 114 (2010), pp. 1602-1609.

Ranghieri, Federica Fallesen, Ditte Marie Gammelgaard Jongman,Brenden Balog,Simone Andrea Breunig Mashahid,Sayed Sharifullah Siercke,Guillermo A. Simpson,Alanna Leigh. Disaster risk profile: Afghanistan (English). Washington, D.C, World Bank Group. http://documents.worldbank.org/curated/en/284301491559464423/Disaster-risk-profile-Afghanistan. (Accessed on Jul 1, 2021).

Rättich, M.; Martinis, S.; Wieland, M. Automatic flood duration estimation based on multi-sensor satellite data. Remote Sens. 2020 12(4), 643, https://doi.org/10.3390/rs12040643.

Rawat, K.S.; Singh, S.K.; Singh, M.I.; Garg, B.L. Comparative evaluation of vertical accuracy of elevated points with ground control points from ASTERDEM and SRTMDEM with respect to CARTOSAT-1DEM. Remote Sens. Appl. 2019, 13, 289–297.

Rice, R.M.; Corbett, E.S.; Bailey, R.G. Soil slips related to vegetation, topography, and soil in Southern California. Water Resour. Res. 1969, 5, 647–659.

Rice, R.M.; Foggin, G.T. Effects of high-intensity storms on soil slippage on mountainous watersheds in Southern California. Water Resour. Res. 1971, 7, 1485–1496.

Rogan, J.; Chen, D. Remote sensing technology for mapping and monitoring land-cover and land-use change. Prog Plann. 2004, 61, 301-325.

Rogers, A. S., Kearney, M.S. Reducing signature variability in unmixing coastal marsh Thematic Mapper scenes using spectral indices. Int. J. Remote Sens. 2004, 25, pp. 2317-2335

Rokni, K., Ahmad, A., Selamat, A., & Hazini, S. Water feature extraction and change detection using multitemporal Landsat imagery. Remote Sens, 2014, 6(5), 4173–4189.

Rouse, J.W., Haas, R.H., Schell, J.A. and Deering, D.W. Monitoring Vegetation Systems in the Great Plains with ERTS (Earth Resources Technology Satellite). Proceedings of 3rd Earth Resources Technology Satellite Symposium, Greenbelt, 1973, 10-14 December, SP-351, 309-317.

Saah, D.; Tenneson, K.; Matin, M.; Uddin, K.; Cutter, P.; Poortinga, A.; Nguyen, Q. H.; Patterson, M.; Johnson, G.; Markert, K.; Flores, A.; Anderson, E.; Weigel, A.; Ellenberg, W. L.; Bhargava, R.; Aekakkararungroj, A.; Bhandari, B.; Khanal, N.; Housman, I. W.; Chishtie, F. Land cover mapping in data scarce environments: Challenges and opportunities. Front. Environ. Sci 2019, 7, https://doi.org/10.3389/fenvs.2019.00150.

Sabokbar, H.F.; Roodposhti, M.S.; Tazik, E. Landslide susceptibility mapping using geographically weighted principal component analysis. Geomorphology 2014, 226, 15-24.

Sarvaiya, J.N.; Patnaik, S. Automatic Image Registration Using Mexican Hat Wavelet, Invariant Moment, and Radon Transform. Int. J. Adv. Comput. Sci. Appl. 2011, 1, 1.

Scaioni, M.; Longoni, L.; Melillo, V.; Papini, M. Remote sensing for landslide investigations: an overview of recent achievements and perspectives. Remote Sens. 2014, 6, 9600-9652.

Scheip, C. M.; Wegmann, K. W. HazMapper: A global open-source natural hazard mapping application in Google Earth Engine. Nat. Hazards Earth Syst. Sci. 2021, 21(5), 1495-1511. https://doi.org/10.5194/nhess-21-1495-2021.

Schuster, R.L. Socioeconomic and environmental impacts of landslides in the Western Hemisphere, U.S. Dept. of the Interior, U.S. Geological Survey: Menlo Park, Calif., 2001.

Shah Marai, 2010. At least 45 killed in latest Afghanistan avalanche. Available online at: https://theworld.org/stories/2012-03-13/least-45-killed-latest-afghanistan-avalanche. (Accessed on Jul. 01, 2022).

Shi, P & Kasperson, R. (2015). World Atlas of Natural Disaster Risk (1st ed. 2015.). Springer Berlin / Heidelberg. DOI: 10.1007/978-3-662-45430-5_17.

Shroder, J.F. Natural Resources in Afghanistan: Geographic and Geologic Perspectives on Centuries of Conflict, 1st ed.; Elsevier: Amsterdam, The Netherlands, 2014; pp. 24–27, ISBN 978-0-12-800135-6.

Shroder, J.F.; Schettler, M.J.; Weihs, B.J. Loess failure in northeast Afghanistan. Phys Chem Earth 2011, 36, 1287-1293.

Shroder, J.F.; Weihs, B.J.; Schettler, M.J. Mass movement in northeast Afghanistan. Phys Chem Earth 2011, 36, 1267-1286.

Sidi Almouctar, M. A.; Wu, Y.; Kumar, A.; Zhao, F.; Mambu, K. J.; Sadek, M. Spatiotemporal analysis of vegetation cover changes around surface water based on NDVI: A case study in Korama basin, Southern Zinder, Niger. Appl. Water Sci. 2020;2021, 11(1), 1-14, https://doi.org/10.1007/s13201-020-01332-x.

Simonett, D.S. Landslide distribution and earthquakes in the Bewani and Torricelli Mountains, New Guinea. In Landform Studies from Australia and New Guinea; Jennings, J.N., Mabbutt, J.A., Eds.; Cambridge University Press: Cambridge, UK, 1967; pp. 64–84.

Singh, A. Review Article Digital change detection techniques using remotely sensed data. Int. J. Remote Sens. 1989, 10, 989-1003.

Sohl, T.L. Change analysis in the United Arab Emirates: an investigation of techniques. Photogramm. Eng. Remote Sens. 1999, 65, 475-484.

Solovey, T. Flooded wetlands mapping from Sentinel-2 imagery with spectral water index: A case study of Kampinos national park in central Poland. Geological Quarterly 2020, 64(2), https://doi.org/10.7306/gq.1509.

Somers, B.; Asner, G.P.; Tits, L.; Coppin, P. Endmember variability in spectral mixture analysis: A review. Remote Sens. Environ. 2011, 115, 1603-1616.

Szostak, M.; Hawryło, P.; Piela, D. Using of Sentinel-2 images for automation of the forest succession detection. Eur. J. Remote Sens. 2018, 51(1), 142-149. https://doi.org/10.1080/22797254.2017.1412272.

The International Federation of Red Cross and Red Crescent Societies (IFRC). Afghanistan: Flash Floods-Final Report DREF Operation No. MDRAF006; 2021; https://reliefweb.int/sites/reliefweb.int/files/resources/MDRAF006dfr.pdf (accessed March 12, 2022).

The International Federation of Red Cross and Red Crescent Societies (IFRC). Afghanistan: Floods - Emergency Plan of Action (EPoA) DREF Operation No. MDRAF008; 2021, Retrieved from: https://reliefweb.int/sites/reliefweb.int/files/resources/MDRAF008do1.pdf. (Accessed March 12, 2022).

Tolo News. Over 110 killed in flash floods in Afghanistan, Aug 27, 2020. https://tolonews.com/afghanistan/over-110%C2%A0killed-flash-floods-afghanistan (Accessed on March 2, 2022).

Tsutsui, K.; Rokugawa, S.; Nakagawa, H.; Miyazaki, S.; Cheng, C.; Shiraishi, T.; Yang, S. Detection and Volume Estimation of Large-Scale Landslides Based on Elevation-Change Analysis Using DEMs Extracted from High-Resolution Satellite Stereo Imagery. IEEE Trans. Geosci. Remote Sens. 2007, 45, 1681–1696.

UNDATA, 2022, Natural disaster information based on assessment data received by OCHA Afghanistan sub-office and IOM Afghanistan Humanitarian Assistance Database (HADB). Humanitarian data exchange (HDX) website: https://goo.gl/PspBze. (Accessed on Jul 1, 2022).

UNDRR (2020). Disaster Risk Reduction in Afghanistan: Status Report 2020. Bangkok, Thailand, United Nations Office for Disaster Risk Reduction (UNDRR), Regional Office for Asia and the Pacific. Accessed from: https://www.undrr.org/publication/disaster-risk-reduction-afghanistan-status-report-2020 (Accessed on Jul,1 2022.).

UNITAR/UNOSAT. The Ab Barak Landslide: Past and Future. 2014, 2-3. Available online: https://unitar.org/maps/map/2058 (Accessed on October 29, 2020).

United Nations International Strategy for Disaster Reduction (UNISDR). The human cost of weather-related disaster 1995-2015, https://www.preventionweb.net/publication/human-cost-weather-related-disasters-1995-2015, (accessed March 12, 2022).

United Nations Population Fund (UNFPA). Badakhshan, a Socio-Economic and Demographic Profile Household, Listing—2003; UNFPA: Kabul, Afghanistan, 2003; pp. 2–3. Available online:

https://www.academia.edu/35118452/Badakhshan_A_Socio_Economic_and_Demographic_Profile_With_the_financial_and_technical_assistance_of_UNFPA (accessed on 5 November 2020).

UNOCHA, 2020. Afghanistan Natural Disaster Incident Reports [2012 through 2020]. Available online: https://data.humdata.org/dataset/afghanistan-natural-disaster-incidents-in-2020 (Accessed on October 20, 2020).

USGS, 2017, Significant Earthquake between 1971 to 2017 in Afghanistan, available online at: https://earthquake.usgs.gov/earthquakes/browse/significant.php?year=2017. (Accessed on Jul 01, 2022).

USGS, 2022, Earthquake between 2014 to 2017 in Afghanistan, available online at: https://earthquake.usgs.gov/earthquakes/browse/significant.php?year=2017. (Accessed on Jul 01, 2022).

Wakil Kohsar/AFP/Getty Image. The Atlantic. Available online: https://www.theatlantic.com/photo/2014/05/massive-landslide-buries-remote-afghan-village/100729/ (accessed on 10 September 2020).

Wang, D.; Wan, B.; Qiu, P.; Su, Y.; Guo, Q.; Wang, R.; Sun, F.; Wu, X. Evaluating the performance of Sentinel-2, Landsat-8 and Pléiades-1 in mapping mangrove extent and species. Remote Sens. 2018, 10(9), 1468, https://doi.org/10.3390/rs10091468.

Wang, S., Baig, M. H. A., Zhang, L., Jiang, H., Ji, Y., Zhao, H., & Tian, J. A simple enhanced water index (EWI) for percent surface water estimation using Landsat data. IEEE J. Sel. Top. Appl. Earth Obs. Remote Sens., 2014, 8(1), 90– 97.

Westfall, A. O, Latkovich, V. J. Surface water resources Investigation Plan for Afghanistan by water resource division U.S. Geological Survey. Available online at: https://apps.dtic.mil/dtic/tr/fulltext/u2/a523598.pdf.

Wheeler, R.L.; Bufe, C.G.; Johnson, M.L.; Dart, R.L.; Norton, G.A. Seismotectonic Map of Afghanistan, with an Annotated Bibliography; U.S. Dept. of the Interior, US Geological Survey: Reston, VA, USA, 2005, pp. 7–10; Open-File Report 2005–1264, USGS Afghanistan Project Product No. 011.

Whitehouse, I.E. Distribution of large rock avalanche deposits in the central Southern Alps, New Zealand, N. Z. J. Geol. Geophys. 1983, 26, 272–279.

Williams, R.D. DEMs of difference. In Geomorphological Techniques, British Society for Geomorphology 2012, Chap. 2, Sec. 3.2, 1-17.

World bank, 2017. Disaster Risk Profile: Afghanistan.available online at: https://www.gfdrr.org/sites/default/files/afghanistan_low_FINAL.pdf (Acessed May 5, 2022)

World bulletin, 2015 avalanche kill 186 in Afghanistan: Available online at: https://worldbulletin.dunyabulteni.net/world/avalanches-kill-186-in-afghanistan-h155698.html. (Accessed on Jul.01,2022).

World Risk Report (2021). Bündnis Entwicklung Hilft, Ruhr University Bochum – Institute for International Law of Peace and Conflict 2021. https://weltrisikobericht.de/weltrisikobericht-2021-e.

Wu, W.; Westra, S.; Leonard, M. A basis function approach for exploring the seasonal and spatial features of storm surge events. Geophys. Res. Lett. 2017, 44(14), 7356-7365. https://doi.org/10.1002/2017GL074357.

Xinhua, 2022, Avalanche, landslide kill 8, injure 10 in Afghanistan. Available online at: https://english.news.cn/20220119/0df94c2b9d9e4bc7805887bfa792e8a6/c.html. (Accessed on Jul. 01, 2022).

Xu, C.; Xu, X.; Shen, L.; Yao, Q.; Tan, X.; Kang, W.; Ma, S.; Wu, X.; Cai, J.; Gao, M.; Li, K. Optimized volume models of earthquake-triggered landslides. Scientific Reports, 2016, 6, 29797.

Xu, H. Modification of normalized difference water index (NDWI) to enhance open water features in remotely sensed imagery. Int. J. Remote Sens. 2006, 27, pp. 3025-3033.

Yilmaz, I. A case study from Koyulhisar (Sivas-Turkey) for landslide susceptibility mapping by artificial neural networks. Bull. Eng. Geol. Env. 2009, 68, 297-306.

Yin, Y.; Wang, F.; Sun, P. Landslide hazards triggered by the 2008 Wenchuan earthquake, Sichuan, China. Landslides, 2009, 6, 139-152.

Zaji, A. H.; Bonakdari, H.; Gharabaghi, B. Remote sensing satellite data preparation for simulating and forecasting river discharge. IEEE Trans Geosci Remote Sens. 2018, 56(6), 3432-3441. https://doi.org/10.1109/TGRS.2018.2799901.

Zekkos, D.; Clark, M.; Cowell, K.; Medwedeff, W.; Manousakis, J.; Saroglou, H.; Tsiambaos, G. Satellite and UAV-enabled mapping of landslides caused by the November 17, 2015, Mw 6.5 Lefkada earthquake, Proc. 19th Int. Conference on Soil Mechanics and Geotechnical Engineering 2017, 17-22.

Zha, Y, Gao, J. Ni, S. Use of normalized difference built-up index in automatically mapping urban areas from TM imagery Int. J. Rem. Sens. 2003, 24 (3), pp. 583-594, 10.1080/01431160304987.

Zhang, J.; Gurung, D.; Liu, R.; Murthy, M.; Su, F. Abe Barek landslide and landslide susceptibility assessment in Badakhshan province, Afghanistan. Landslides, 2015, 12, 597-609.

Zhang, T.; Su, J.; Liu, C.; Chen, W. Potential bands of Sentinel-2A satellite for classification problems in precision agriculture. Int. J. Autom. Comput. 2019, 16(1), 16-26. https://doi.org/10.1007/s11633-018-1143-x.

Zhang, Y.; Meng, X.M.; Dijkstra, T.A.; Jordan, C.J.; Chen, G.; Zeng, R.Q.; Novellino, A. Forecasting the magnitude of potential landslides based on InSAR techniques. Remote Sens. Environ. 2020, 241, 111738.

List of Publications

Atefi, M. R. and Miura, H.: Volumetric Analysis of the Landslide in Abe Barek, Afghanistan Based on Nonlinear Mapping of Stereo Satellite Imagery-Derived DEMs, *Remote Sensing*, 13(3), 446, 2021, https://doi.org/10.3390/rs13030446.

Atefi, M. R. and Miura, H.: Detection and Volume Estimation of Large-scale Landslide in Abe Barek, Afghanistan Using Nonlinear Mapping of DEMs, *International Geoscience and Remote Sensing Symposium (IGARSS)*, 3757-3760, 2021, https://doi.org/10.1109/IGARSS47720.2021.9554504 .

Atefi, M.R.; Miura, H. Detection of Flash Flood Inundated Areas Using Relative Difference in NDVI from Sentinel-2 Images: A Case Study of the August 2020 Event in Charikar, Afghanistan. Remote Sens. 2022, 14, 3647. https://doi.org/10.3390/rs14153647

Atefi, M. R. and Yamamoto, H.: Obtaining the Optimum Inclination Angle of Anchor by Using Minor Principal Stress, *Proceedings of Annual Research Meeting, Chugoku Chapter, Architectural Institute of Japan (AIJ)*, 41, 105-108, 2017.

Atefi, M. R. and Yamamoto, H.: Using D-C Model to Evaluate the Stabilization Technique in a Typical Soil Sample under Tri-Axial Compression Stresses, *Proceedings of Annual Research Meeting, Chugoku Chapter, Architectural Institute of Japan (AIJ)*, 41, 109-112, 2017.